Title
Development of non-local density functionals

Author
Krull, Brandon

Publication Date
2015

Peer reviewed|Thesis/dissertation

UNIVERSITY OF CALIFORNIA,
IRVINE

Development of non-local density functionals

DISSERTATION

submitted in partial satisfaction of the requirements
for the degree of

DOCTOR OF PHILOSOPHY

in Chemistry

by

Brandon Tyler Krull

Dissertation Committee:
Professor Filipp Furche, Chair
Professor Kieron Burke
Professor Alan F. Heyduk

2015

TABLE OF CONTENTS

LIST OF FIGURES

LIST OF TABLES

LIST OF COMMONLY USED ABBREVIATIONS

AO	atomic orbital
CGTO	Cartesian Gaussian-type orbital
DFT	density functional theory
GGA	generalized gradient approximation
GPT	Gaussian product theorem
HF	Hartree-Fock
HOMO	highest occupied molecular orbital
KS	Kohn-Sham
LH	local hybrid
LR	long-range
LRSH	locally range-separated hybrid
LUMO	lowest unoccupied molecular orbital
MGGA	meta-generalized gradient approximation
MO	molecular orbital
PBE	Perdew-Burke-Ernzerhof semi-local GGA density functional
PBE0	hybrid version of PBE including 25% HF exchange
RPA	Random Phase approximation
RSH	range-separated hybrid
SR	short-range
TDDFT	time-dependent density functional theory
TPSS	Tao-Perdew-Staroverov-Scuseria semi-local MGGA density functional
UV-vis	ultraviolet-visible spectroscopy
XC	exchange-correlation

ACKNOWLEDGMENTS

I am thankful for all of my friends and colleagues I have made while going through graduate school. A particularly large thanks to Drs. Jeb Bates, Nate Sickerman, Vamsee Voora, Shane Parker, and (eventually Dr.) Martim Galvão. It was a great experience to work with and be around such a diverse set of gifted and creative people. Additional thanks goes to all of my other friends that I wasn't forced to see on a nearly-daily basis: Albert Zhu, Tobias Friedberger, Ben Toulson, Moritz Limpinsel, Jason Schroeder, Wes Kramer, Avi Khanna, Luke Hanna, Gavin Bascom, Mark Hilkert, Dave Marsh, Aurora Pribram-Jones. The friendships really are one of the great take-aways from grad school.

To the Furche research group, it has been an honor to be surrounded by such motivated and intelligent students, including high-school students, undergraduates, graduates, and post-docs. Special thanks to Nate Crawford for always dealing with our group's issues and for being patient and explaining our infrastructure to me. I really appreciate the contributions of Jason Yu, Brian Nguyen, Justin Le, and Jake Kwon, the four students who assisted in the luciferin project. Thanks to past and present members Ingolf Warnke, Henk Eshuis, Jordan Vincent, Erik Almaraze, who were there to provide support when the grad school experience got tough and good luck to younger students Guo, Sree, Saswata, and Matt.

I would like to thank my friends from home: Drew Piszyk, Teddy Truc, Tien Le, Eric Dao, Young Pak, Lawrence Yang, Martin Vo, Jeremy Tseng, Alex Dao, Viet Nguyen, and Joyce Lin. Whether it be mindless fun or productive conversation, I have shared most of my life experiences with you and I'm glad to have had your support along the way.

Many thanks to my committe members Alan Heyduk and Kieron Burke. We had both light-hearted and serious conversations when I was in need. Your perspective on life has been very helpful to me.

To Filipp, working on myself under your guidance has been single handedly the most challenging thing I have ever done in my life. Your ruthless dedication to rigor, absolute selflessness and devotion to the education process as a whole is inspiring. I am a better mentor, educator, scientist, and person because of you.

I would like to thank my extremely supportive family. Though mostly hands-off, they have never second guessed letting me run off on my own to pursue whatever I think is best, all with any judgements. I am who I am today because of them.

I am extremely grateful for my partner, Alysa Fukunaga, who has helped me with immense personal growth and challanges me every day to be a better person.

CURRICULUM VITAE

Brandon Tyler Krull

EDUCATION

Doctor of Philosophy in Chemistry **2015**
University of California *Irvine, California*

Master of Science in Chemistry **2012**
University of California *Irvine, California*

Bachelor of Science in Chemistry **2010**
California State Polytechnic University *Pomona, California*

Bachelor of Science in Biotechnology **2010**
California State Polytechnic University *Pomona, California*

TEACHING EXPERIENCE

Head Teaching Assistant - Honors general chemistry lecture **2012**
University of California *Irvine, California*

Teaching Assistant - Analytical chemistry laboratory **2011**
University of California *Irvine, California*

Teaching Assistant General chemistry laboratory **2010–2011**
University of California *Irvine, California*

MENTORING EXPERIENCE

High school mentor, student: Justin Le **2014–present**
University of California *Irvine, California*

Undergraduate mentor, student: Jason Yu **2013–present**
University of California *Irvine, California*

Undergraduate mentor, student: Brian Nguyen **2012–present**
University of California *Irvine, California*

High school mentor, student: Jake Kwon **2012–2013**
University of California *Irvine, California*

REFEREED JOURNAL PUBLICATIONS

1. *Structural, Spectroscopic, and Theoretical Comparison of Traditional vs. Recently Discovered Ln^{2+} Ions in the [K(2.2.2-cryptand)][($C_5H_4SiMe_3$)$_3$Ln] Complexes: The Variable Nature of Dy^{2+} and Nd^{2+}*
   M.E. Fieser, M.R. MacDonald, **B.T. Krull**, J.E. Bates, J.W. Ziller, F. Furche, and W.E. Evans.
   Journal of the American Chemical Society, 2015, 137(1), 369-382.

2. *Metal effects on ligand non-innocence in Group 5 complexes of the redox-active [ONO] pincer ligand*
   S. Hananouchi, **B.T. Krull**, J.W. Ziller, F. Furche, A.F. Heyduk.
   Dalton Transations, 2014, 43, 17991-18000.

3. *Acclerated Growth of Dendrimers via Thiol-Ene and Esterification Reactions*
   M.I. Montanez, L.M. Campos, P. Antoni, Y. Hed, M.V. Walter, **B.T. Krull**, A. Khan, A. Hult, C.J. Hawker, M. Malkoch.
   Macromolecules, 2010, 43, 6004-6008.

REFEREED CONFERENCE PRESENTATIONS

1. *Range-separated hybrids with correct scaling to the high density limit*
   American Chemical Society Western Regional Meeting, San Diego, CA, 2015.

2. *Non-local Density Functionals using Novel Integration Techniques*
   World Association of Theoretical Chemists 2014, Santiago, Chile, 2014.

3. *Non-local Density Functionals using Novel Integration Techniques*
   TURBOMOLE 25th Anniversary Conference, Karlsruhe, Germany, 2014.

4. *A Novel Fully Nonlocal XC-Functional Free of Self-Interaction Error*
   Gordon Research Conference, Time-Dependent Density Functional Theory, Biddeford, ME, 2013.

ABSTRACT OF THE DISSERTATION

Development of non-local density functionals

By

Brandon Tyler Krull

Doctor of Philosophy in Chemistry

University of California, Irvine, 2015

Professor Filipp Furche, Chair

This thesis focuses on the use and development of electronic structure methods in the density functional theory (DFT) framework. The first half is devoted to the implementation of a new integral algorithm and its use in fully non-local density functional approximations. While costly compared to simpler semi-local approximations, non-local functionals of the density are a way to intuitively incorporate physics into a real-space model. Two broad classes of methods are targeted: locally-range separated hybrids and non-local exchange kernels. These methods are tested on a variety of small systems. In both cases, proper scaling to the high-density limit is satisfied which turns out to hamper the approximations' ability to describe static correlation. This leads us to conclude that proper scaling methods will inherently need static correlation corrections if good performance in thermochemical measures is desired. In the second half, DFT is applied to three drastically different problems which highlights its ability to reasonably predict experimental structural parameters of compounds containing f- and d- block elements while simultaneously describing excited state properties of main group and transition metal compounds. Using time-dependent DFT, UV-vis spectra of lanthanides, transition metals, and the small molecule luciferin were simulated and found to be in good agreement with experiments, providing photophysical insight to the nature of their excited states.

Chapter 2 describes a new recursion scheme that was derived in order to target the evaluation of non-local interaction kernels. The integrals that arise from such kernels are first transformed into relative and center of mass coordinates and then rewritten in terms of an integral over the relative coordinate that is parametrically dependent on the center of mass. Using the shared-memory parallel progamming API, OpenMP, a multithreaded semi-analytical algorithm is presented where integrals over the relative coordinate are evaluated for blocks of grid points of the numerical integration. The algorithm scales as $O(N^5)$, where N is a measure of the system size, but prescreening based on density and integral prefactors are used to reduce the cost. In its present state, the algorithm is still costly and has been limited to only smaller molecules. Benchmark tests show that the recursion scheme can precisely recover the Coulomb interaction and that screening reduces the overall computational cost by 10-15% for small systems. The prescreening which is based on the sparsity of the exchange density matrix, should lead to asymptotic linear scaling with increasing system size; however, this is not realized in practice and is not fully understood at this point. Despite efforts to efficiently parallelize the numerical integration, the total wall time as a function of number of CPUs, does not behave as $1/N_{cpu}$, leading to the conclusion that there is a bottleneck executed on only a single CPU that reduces the efficiency. Testing of the implementation on larger systems is necessary to see if the screening behaves as expected and to further analyze the parallel efficiency.

Chapters 3 and 4 are focused on building non-local models of the density functional exchange-correlation energy using the integral scheme developed in chapter 2. Chapter 3 focuses on locally range-separated hybrids. Here, the exchange interaction is partitioned into long-range and short-range contributions via a range-separation function. We model this function using a density-dependent functional that is evaluted at the center of mass. Our models are made to satisfy exact constraints such as correct scaling in the high-density limit and good description of one-electron and iso-orbital regions. We propose and test a variety of forms that fall into two classes: ones that use long-range exact exchange with short-range approximate

exchange and ones that use short-range exact exchange with long-range exchange. Overall, with scaling to the high-density limit being enforced, atomization energies tend to be too low, though self-interaction error is significantly reduced. These proper scaling methods hint at the need to reintroduce the static correlation effects not described by Hartree-Fock to achieve a pragmatic balance. In chapter 4, corrections to the random-phase approximation are explored by way of a short-ranged non-local static exchange kernel. Our first model constructed consisted of a short-ranged Gaussian function. Use of this type of exchange kernel was plagued with instabilities which can be traced to negative values of the Fourier transform of the Hartree-exchange-correlation kernel. A second similar model based on an error function was also constructed and was better behaved. In places where instabilities occured, the first-order RPA-renormalization framework was used and shown to alleviate instabilities in both cases. The fact that a direct modeling of exchange kernels often leads to instabilities indicates that this route to beyond-RPA corrections may be more difficult than once assumed. Additionally, despite the fact that the implementation is purely proof of concept, the high $O(N^5)$ cost of computing the non-local integrals is challenging to manage and considerable effort would be required to reduce it.

Chapters 5-7 are based on collaborative work with other research groups at UCI. In chapter 5, a joint computational and experimental study on the photophysical properties of the light-emitting molecule luciferin was undertaken. Using time-dependent DFT, the excited states of a plethora of luciferin analogues were studied in order to find novel, robust light emitting species. While computed oscillator strengths corresponded well with previously known luciferins, the simple picture of non-adiabatic emission from the first singlet excited state was only moderately reliable in predicting the chemiluminescent properties of newly synthesized luciferins. This work implies the need for explicit consideration of environmental effects and the inclusion of other nearby electronic states in order to have a reliably predictive methodology. In chapter 6, a comprehensive study of lanthanides recently discovered to have a new +2 oxidation state was undertaken. Time-dependent DFT was used to simulate the

UV-vis spectra of new complexes of Eu, Sm, Tm, Yb, Dy, and Nd which were found to be in good agreement with experiments. Nd and Dy were found to be "crossover" elements in that their electronic ground state could be modulated easily by its ligand environment, in contrast to previous paradigms. In chapter 7, a comparison of complexes of Group V metals (vanadium, niobium, and tantalum) coordinated to redox active ligands is presented. The main challenge in using computational tools to study these complexes lies in the fact that they are coordinated to redox-active ligands which significantly complicate their electronic structure. It was discovered that while Nb and Ta are well described by a closed-shell singlet in their +5 oxidation state, V differs dramatically and has a more stable solution in the +4 oxidation state with open-shell singlet diradical character. This points to subtelties in the electronic structure of transition metals that can be exploited in catalytic applications.

Chapter 1

Statement of the problem

The global energy crisis and the associated climate change poses one of the most pressing issues for our society today. In this light, energy derived from solar radiation is one of the most promising solutions because it is overly abundant and its use has little-to-no environmental impact. Progress towards developing materials for solar applications is increasingly important and devices made from synthetic organics are appealing due to their cheap manufacturing cost and tunable properties. To design effective materials, it is necessary to understand their photophysical properties which amounts to understanding both their electronic ground and excited states. While spectroscopy and microscopy techniques are always improving, theoretical insights are increasingly important for understanding the electronic structure which governs their behavior. Given the difficulty of solving the time-dependent many-fermion problem for complex systems, electronic structure has rightfully become an engaging and cutting edge field over the past several decades.

Predictive and efficient computational methods for describing the electronic structure of molecules and materials are necessary for laying the foundation on which the design of light-harvesting materials will hinge. Semi-local Kohn-Sham (KS) density functional theory

(DFT) is often the preferred method because of its balance between cost and accuracy. It has been a vital component in studies of heterogeneous water splitting photocatalysts[1–3] and dye-sensitized titania nanoparticles,[4,5] two of the most active fields of research. While many approximate ground state density functionals exist, none of them are without shortcomings.[6] Further, when studying excited states, the use of a time-dependent variant of DFT (TDDFT) is necessary. Modern implementations of TDDFT simply take an approximate ground state density functional and use it in a linear response framework to obtain the time (or frequency) dependent response. These calculations often inherit the problems of the ground state functional that was used.[7] Many of the issues with (TD)DFT can be traced back to the underlying semi-local density functional approximation, and specifically to the fact that semi-local quantities are used to describe an inherently non-local interaction.

Developing non-local density functional approximations that have the potential to remedy the main shortcomings of semi-local functionals is the next step towards predictive methods. Such functionals have been theorized for decades[8,9] but are not applied to larger molecules or materials because of their steep computational cost. To this end, having efficient algorithms to evaluate non-local density functional approximations is a prequisite to applying such methods to complex systems. The first step in furthering our understanding of these approximations is to use them to study new and exotic materials. This contributes to a positive feedback loop where continued use of a new type of approximation provides further insight into its behavior, which, in turn, can be used to improve the theoretical framework.

Chapter 2

Integration methods for non-local density functionals

2.1 Introduction

Calculation of the four-center, two-electron integrals is the computational bottleneck in all ground-state Hartree-Fock (HF) and density functional theory (DFT) calculations.[10–12] Scaling formally as $O(N^4)$, where N is a measure of the system size, i.e. the number of basis functions, billions of integrals are routinely computed for even moderately sized finite systems. For example, in the octopeptide Angiotension II using a small split-valence basis set, there are a total of 1192 basis functions which leads to roughly twenty-three trillion non-negligible, non-redundant integrals per self-consistent field (SCF) iteration. This task would be impossible to carry out if all integrals were to be computed and stored, requiring in this example, 190GB of disk space per SCF iteration.[1]

[1]The contributing twenty-three trillion integrals are ones who are unique and are larger than 2.6×10^{-12}. The storage estimate is based on storing contributing integrals whose values are larger than 10^{-5}, where each integral is a double precision floating point number that takes up 8 bytes.

For many decades, the algorithmic and mathematical research in quantum chemistry was concerned with reducing both the CPU and memory loads resulting from the innumerable integrations.[13–21] In the late 1980's Almlöf proposed a way to avoid the reading-from and writing-to disk bottleneck in the calculation of integrals by computing them in a direct, on-the-fly manner.[22] This revolutionized electronic structure calculations and made it possible to compute the energy of systems with around 500 basis functions, an impressive feat given the available computational technology of the time. Efficient ways to evalute the integrals were developed, including both numerical[15,16,23] and analytical schemes.[13,14,18] Screening procedures were constructed to compute only non-negligible contributions,[24] molecular symmetry was exploited,[15,24,25] and multipole methods[26–30] and density fitting techniques[31–33] were instrumental in reducing the $O(N^4)$ scaling to $O(N^2)$ by factorizing the four-center integrals into products of two- and three-center integrals. In a modern SCF calculation, all of the above techniques are simultaneously applied which gives DFT its appealing low-scaling computational cost.

Recent advancements in integral schemes have come from two main approaches: (1) the integral algorithms are being modernized to effectively use today's computational resources and (2) the mathematical approaches for evaluating the Coulomb integrals are being extended to more complicated interaction kernels. With respect to the first approach, there have been modest attempts to reorganize the Fock matrix build (and implicitly, computation of the two-electron integrals) to fit on GPUs,[34–38] an increasingly hot topic as of late. However, hand coding of integrals is necessary and is tedious for angular momentum functions higher than p-functions, which is crucial for a good description of most chemical systems. With respect to the second approach, progress has been made in dealing with integrals that arise from, e.g. van der Waals density functionals, and are based on six-dimensional numerical integrations,[39,40] but these methods tend to have challenges when integrating functions that rapidly vary in space or have many cusps, such as the ones that arise frequently in the electron-electron interaction. For relativistic calculations, promising timings for the calcula-

tion of three-electron Breit integrals were recently reported.[41] Despite these advancements, widely applicable non-local density functionals still remain elusive because of their high computational cost.

The goal of this chapter is to develop modern integral schemes that will allow quantum chemists to explore new models based on non-local interaction kernels. For the present discussion, it is sufficient to simply define the type of integral that we are interested in computing, with little focus on the specific purpose. The use of the new integral methodology will be discussed in later chapters. The interaction kernels are inspired by the growing interest in being able to balance the description of static-correlation with minimizing self-interaction error.[42–46] Such models require non-locality and flexibility. The integrals we seek to compute are over atom-centered Gaussian basis functions interacting via a kernel of the form

$$f(u, \mathbf{R}) = g^{sr}(u, \mathbf{R}) \sum_{n=-1}^{N} c_n(\mathbf{R}) u^n. \tag{2.1}$$

Here, $u = |\mathbf{r}_1 - \mathbf{r}_2|$ is the relative electron coordinate and $\mathbf{R} = \frac{1}{2}(\mathbf{r}_1 + \mathbf{r}_2)$ is the electron center-of-mass (COM) coordinate. g^{sr} is a short-ranged function such as an error function or Gaussian function. Non-locality is introduced through the center-of-mass dependence of the function g^{sr} and the coefficients c_n. These non-local functions are functionals of the density and its derivatives evaluated at the center-of-mass coordinate. In principle, the methodology described herein can be applied to any number of powers of u;[47] however, the current implementation can only handle $n = -1, 0, 1, 2$, and 3. We begin by describing notation of the two-electron integrals over atom-centered Gaussian basis sets (Sec. 2.2). This is followed by a derivation of a new recursion scheme (Sec. 2.3) that allows for calculation of classes of non-local integrals that have been previously intractable. In Section 2.4, a semi-analytical algorithm is presented, implemented in DSCF using the OpenMP parallel programming API, and in Section 2.5 the accuracy and performance are assessed.

2.2 Definitions

We are interested in computing the energy associated two charge densities interacting via a potential described by Eq. (2.1)

$$E = \frac{1}{2} \int d^3 r_1 d^3 r_2 \rho(\mathbf{r}_1) f(\mathbf{r}_1, \mathbf{r}_2) \rho(\mathbf{r}_2), \tag{2.2}$$

where

$$\rho(\mathbf{r}) = \sum_i^N \phi_i^*(\mathbf{r}) \phi_i(\mathbf{r}) \tag{2.3}$$

is the electron density at $\mathbf{r} = (r_x, r_y, r_z)$ written in terms of the N occupied Kohn-Sham orbitals. To arrive at the four-center, two-electron integrals, we expand each orbital in a basis of atom-centered Cartesian Gaussian-type orbitals (CGTOs) according to

$$\phi_i(\mathbf{r}) = \sum_\mu^{N_{bf}} C_{i\mu} \chi_\mu(\mathbf{r}). \tag{2.4}$$

$C_{i\mu}$ is a contraction coefficient, and χ_μ is an unnormalized primitive Cartesian Gaussian-type orbital with exponent ζ_μ centered at $\mathbf{r}_\mu = (r_{\mu x}, r_{\mu y}, r_{\mu z})$ and angular momentum $\boldsymbol{\ell}_\mu = (\ell_{\mu x}, \ell_{\mu y}, \ell_{\mu z})$,

$$\chi_\mu(\mathbf{r}) = \chi(\mathbf{r}|\boldsymbol{\ell}_\mu, \zeta_\mu, \mathbf{r}_\mu) \equiv \prod_{i \in \{x,y,z\}} (r_i - r_{\mu i})^{\ell_{\mu i}} e^{-\zeta_\mu |r_i - r_{\mu i}|^2}. \tag{2.5}$$

Using the basis set expansion for each Kohn-Sham orbital in (2.2), we arrive at the energy expression in an atom-centered basis set

$$E = \frac{1}{2} \sum_{\mu\nu\kappa\lambda} D_{\mu\nu} D_{\kappa\lambda} (\mu\nu|\kappa\lambda). \tag{2.6}$$

Here, $D_{\mu\nu} = \sum_i C_{\mu i} C_{i\nu}$ is the one-electron density matrix and the four-center, two-electron integrals are defined in Mulliken notation as

$$(\mu\nu|\kappa\lambda) = \int d^3r_1 d^3r_2 \chi_\mu(\mathbf{r}_1)\chi_\nu(\mathbf{r}_1) f(\mathbf{r}_1,\mathbf{r}_2)\chi_\kappa(\mathbf{r}_2)\chi_\lambda(\mathbf{r}_2). \tag{2.7}$$

Due to the non-trivial center-of-mass dependence of the interaction kernel in Eq. (2.1), the integral can be more easily evaluted following a coordinate transformation to relative $\mathbf{u}$ and COM $\mathbf{R}$ coordinates where a four-center, one-electron integral over $\mathbf{u}$ is parametrically dependent on $\mathbf{R}$,

$$(\mu\nu|\kappa\lambda) = \frac{(-1)^{(|\boldsymbol{\ell}_\kappa|+|\boldsymbol{\ell}_\lambda|)}}{2^{(|\boldsymbol{\ell}_\mu|+|\boldsymbol{\ell}_\nu|+|\boldsymbol{\ell}_\kappa|+|\boldsymbol{\ell}_\lambda|)}} \int d^3R \, [\boldsymbol{\ell}_\mu \boldsymbol{\ell}_\nu \boldsymbol{\ell}_\kappa \boldsymbol{\ell}_\lambda](\mathbf{R}) \tag{2.8}$$

$$[\boldsymbol{\ell}_\mu \boldsymbol{\ell}_\nu \boldsymbol{\ell}_\kappa \boldsymbol{\ell}_\lambda](\mathbf{R}) = \tag{2.9}$$

$$\int d^3u \; \chi_\mu(\mathbf{u}|\boldsymbol{\ell}_\mu, \bar{\zeta}_\mu, \bar{\mathbf{r}}_\mu)\, \chi_\nu(\mathbf{u}|\boldsymbol{\ell}_\nu, \bar{\zeta}_\nu, \bar{\mathbf{r}}_\nu)\, f(u|\mathbf{R}) \chi_\kappa(\mathbf{u}|\boldsymbol{\ell}_\kappa, \bar{\zeta}_\kappa, \bar{\mathbf{r}}'_\kappa)\, \chi_\lambda(\mathbf{u}|\boldsymbol{\ell}_\lambda, \bar{\zeta}_\lambda, \bar{\mathbf{r}}'_\lambda). \tag{2.10}$$

Here, we condense the center-of-mass dependence into barred quantities, where $\bar{\mathbf{r}}_\delta = 2(\mathbf{r}_\delta - \mathbf{R})$, $\bar{r}'_\delta = 2(\mathbf{R} - \mathbf{r}_\delta)$, and $\bar{\zeta}_\delta = \frac{1}{4}\zeta_\delta$. The prefactor in Eq. (2.8) results from the transformation to relative and COM coordinates and can be applied to the entire $\mathbf{u}$ integration for a given shell quadruple. The recursion described herein is for the analytical evaluation of integral (2.9) over the relative coordinate. It hinges on two convenient properties of Gaussian functions: their differential relationship[48]

$$\frac{\partial}{\partial r_{\mu i}} \chi_\mu(\mathbf{r}|\ell_{\mu i}, \zeta_\mu, r_{\mu i}) = 2\zeta_\mu \chi_\mu(\mathbf{r}|\ell_{\mu(i+1)}, \zeta_\mu, r_{\mu i}) - \ell_{\mu i}\delta_{ij}\chi_\mu(\mathbf{r}|\ell_{\mu(i-1)}, \zeta_\mu, r_{\mu i}), \tag{2.11}$$

and the fact that they can be combined via the Gaussian product theorem[49] (GPT)

$$e^{-a(\mathbf{r}-\mathbf{A})^2}e^{-b(\mathbf{r}-\mathbf{B})^2} = e^{-\frac{ab}{a+b}(\mathbf{A}-\mathbf{B})^2}e^{-(a+b)\left(\mathbf{r}-\frac{a\mathbf{A}+b\mathbf{B}}{a+b}\right)^2}. \tag{2.12}$$

Integration over $\mathbf{R}$ is done numerically (see Section 2.4.1). Round brackets $(\cdot)$ correspond to the entire two-electron integral, while square brackets $[\cdot]$ correspond to only the integral over the relative coordinate.

2.3 Recursion relations for non-local interactions

2.3.1 The integral [0000]

Evaluation of the integral over Gaussian basis functions (2.7) begins by computing the integral over only spherical (or s) functions

$$[\mathbf{0000}] = \int d^3u\, e^{-\zeta_\mu(\mathbf{u}-\mathbf{r}_\mu)^2}\, e^{-\zeta_\nu(\mathbf{u}-\mathbf{r}_\nu)^2}\, f(u)\, e^{-\zeta_\kappa(\mathbf{u}-\mathbf{r}'_\kappa)^2}\, e^{-\zeta_\lambda(\mathbf{u}-\mathbf{r}'_\lambda)^2}. \tag{2.13}$$

We suppress the use of barred notation for $\bar{\mathbf{r}}$ and $\bar{\zeta}$ for clarity but retain the primed " $'$ " notation to highlight the different center-of-mass dependence of the basis functions' locations. Using the GPT (Eq. (2.12)) to combine all four basis functions and the Gaussian of the interaction, Equation (2.13) is reduced to a one-dimensional elementary integral G_0 after integration over the angular components of $\mathbf{u}$. This is cast into the form

$$[\mathbf{0000}] = K_{\mu\nu\kappa\lambda}\, G_0(\zeta, T) \tag{2.14}$$

where $K_{\mu\nu\kappa\lambda}$ is a prefactor used for screening and G_0 (via its arguments) is dependent on the type of range-separation function that is to be incorporated; three examples are given

below. Here,

$$K_{\mu\nu\kappa\lambda} = \mathrm{Exp}[T - (\zeta_\mu r_\mu^2 + \zeta_\nu r_\nu^2 + \zeta_\kappa r_\kappa'^2 + \zeta_\lambda r_\lambda'^2)], \tag{2.15}$$

$$\mathbf{U} = \zeta_\mu \mathbf{r}_\mu + \zeta_\nu \mathbf{r}_\nu + \zeta_\kappa \mathbf{r}'_\kappa + \zeta_\lambda \mathbf{r}'_\lambda, \tag{2.16}$$

$$\gamma = \zeta_\mu + \zeta_\nu + \zeta_\kappa + \zeta_\lambda, \tag{2.17}$$

$$T = \frac{1}{\zeta} U^2. \tag{2.18}$$

The definitions for G_0, ζ, and T depend on the choice of range-separation function.

For $g^{sr} = e^{-(zu)^2}$, the expression for G_0 is

$$G_0^{Gaus}(\zeta, T) = \frac{2\pi}{\zeta} F_0[T], \tag{2.19}$$

$$\zeta = \gamma + z^2. \tag{2.20}$$

where F_0 is the Boys function,[17] which is obtained by a change of variables from the error function[48]

$$F_n(x) = \int_0^1 dt e^{-xt^2} t^{2n}. \tag{2.21}$$

This is easily obtained because the interaction can be directly incorporated via the GPT. It is effectively a fifth Gaussian basis function that is centered at the origin of the center-of-mass.

For the Error function, g^{sr} =Erf$[zu]$,

$$G_0^{Erf}(\zeta, T) = 2\pi \sqrt{\frac{\gamma}{\zeta}} F_0[T], \tag{2.22}$$

$$\zeta = \frac{\gamma(\gamma + z^2)}{z^2}. \tag{2.23}$$

Additional work is required to give this expression because the Error function itself is an integral (see Appendix A).

For $g^{sr} = 1$, we recover the plain Coulomb integral and results in

$$G_0 = \frac{2\pi^{5/2}}{(\mu+\nu)(\kappa+\lambda)\sqrt{\gamma}} F_0[T], \tag{2.24}$$

$$\zeta = \gamma. \tag{2.25}$$

2.3.2 Vertical recursion

The vertial recursion is built on the differential relation of Gaussian functions (Eq. (2.11)) which can be extended to the integral level as

$$[(\boldsymbol{\ell}_\mu + \mathbf{1}_i)\boldsymbol{\ell}_\nu\boldsymbol{\ell}_\kappa\boldsymbol{\ell}_\lambda] = \hat{D}_{\mu i}[\boldsymbol{\ell}_\mu\boldsymbol{\ell}_\nu\boldsymbol{\ell}_\kappa\boldsymbol{\ell}_\lambda] + \frac{\ell_{\mu i}}{2\zeta_\mu}[(\boldsymbol{\ell}_\mu - \mathbf{1}_i)\boldsymbol{\ell}_\nu\boldsymbol{\ell}_\kappa\boldsymbol{\ell}_\lambda]. \tag{2.26}$$

Here, $\hat{D}_{\mu i} = \frac{1}{2\zeta_\mu}\frac{\partial}{\partial r_{\mu i}}$ and $\mathbf{1}_i$ represents a single angular momentum unit in the i-Cartesian direction. In the present scheme, it is sufficient to only describe the increase in angular momentum on one center since expression (2.13) is symmetric under interchange of any center.

Following Ahlrichs' derivation,[47] we apply the differential operator $\hat{D}_{\mu i}$ to $[\mathbf{0000}]$ yielding an integral with a unit-increased angular momentum on basis function μ resulting from the sum of two terms

$$\hat{D}_{\mu i}[\mathbf{0000}] = (\hat{D}_{\mu i}K_{\mu\nu\kappa\lambda})G_0 + K_{\mu\nu\kappa\lambda}(\hat{D}_i G_0) = [\mathbf{1}_i\mathbf{000}], \tag{2.27}$$

$$\hat{D}_{\mu i}K_{\mu\nu\kappa\lambda} = (\frac{1}{\zeta}U_i - r_{\mu i})K_{\mu\nu\kappa\lambda};\ \hat{D}_{\mu i}G_0 = -\frac{1}{\zeta}U_i G_1 \tag{2.28}$$

where $K_{\mu\nu\kappa\lambda}, G_0, \mathbf{U}, \mathbf{T}$, and ζ are defined in Section 2.3.1 and

$$G_m(\zeta, T) = \left(-\frac{\partial}{\partial T}\right)^m G_0(\zeta, T) \tag{2.29}$$

denotes auxiliary integrals. Differentiation of $[\mathbf{1}_i\mathbf{000}]_u$ additionally requires the identities

$$\hat{D}_{\mu i}(\frac{1}{\zeta}U_i - r_{\mu i}) = \frac{1}{2\zeta};\ \hat{D}_{\mu i}(-\frac{1}{\zeta}U_i) = -\frac{1}{2\zeta}. \tag{2.30}$$

Combining equations (2.28) and (2.30) leads to the working 4-term vertical recursion relation,

$$\begin{aligned}[(\boldsymbol{\ell}_\mu + \mathbf{1}_i)\mathbf{000}]^{(m)} =&(\frac{1}{\zeta}U_i - r_{\mu i})[\boldsymbol{\ell}_\mu\mathbf{000}]^{(m)} - \frac{1}{\zeta}U_i[\boldsymbol{\ell}_\mu\mathbf{000}]^{(m+1)}+ \\ &\frac{\ell_{\mu i}}{2\zeta_\mu}\left([(\boldsymbol{\ell}_\mu - \mathbf{1}_i)\mathbf{000}]^{(m)} - [(\boldsymbol{\ell}_\mu - \mathbf{1}_i)\mathbf{000}]^{(m+1)}\right).\end{aligned} \tag{2.31}$$

Here, the superscript (m) corresponds to auxiliary integrals. In practice, one first generates auxiliary integrals G_m up to $m = \ell_{max} + 1$ followed by an increase of angular momentum on basis function μ up to ℓ_{max}, where $\ell_{max} = |\boldsymbol{\ell}_\mu| + |\boldsymbol{\ell}_\nu| + |\boldsymbol{\ell}_\kappa| + |\boldsymbol{\ell}_\lambda|$. Vertical recursion where angular momentum is generated only on the first center scales as ℓ^4p^4 in cost and ℓ^3p^4 in memory, where ℓ is the angular momentum and p is the number of primitive functions in a contracted orbital. The more widely implemented version of Obara-Saika recursion has two vertical recursion steps (OS2) inside the primitive loop and scales as ℓ^7p^4 in FLOPs and ℓ^6p^4 in memory.[50]

2.3.3 Horizontal and transfer recursions

The total translational invariance of the two-electron integrals allows angular momentum to be shifted from one center to another outside of the loop over primitive functions[14]

$$\begin{aligned}[\boldsymbol{\ell}_\mu(\boldsymbol{\ell}_\nu + \mathbf{1}_i)\mathbf{00}] &= [(\boldsymbol{\ell}_\mu + \mathbf{1}_i)\boldsymbol{\ell}_\nu\mathbf{00}] + (r_{\mu i} - r_{\nu i})[\boldsymbol{\ell}_\mu\boldsymbol{\ell}_\nu\mathbf{00}] \\ [\mathbf{00}\boldsymbol{\ell}_\kappa(\boldsymbol{\ell}_\lambda + \mathbf{1}_i)] &= [\mathbf{00}(\boldsymbol{\ell}_\kappa + \mathbf{1}_i)\boldsymbol{\ell}_\lambda] + (r'_{\kappa i} - \bar{r}'_{\lambda i})[\mathbf{00}\boldsymbol{\ell}_\kappa\boldsymbol{\ell}_\lambda].\end{aligned} \tag{2.32}$$

The obvious benefit to using horizontal recursion is the reduction of FLOPs in the $O(N^4)$ primitive loop. In our particular case, the horizontal recursion step for shifting angular momentum from, e.g. $\mu \rightarrow \nu$ or $\kappa \rightarrow \lambda$, is also independent of the numerical quadrature because of the cancellation of $\mathbf{R}$-dependence between the two centers ($\bar{\mathbf{r}}_\mu - \bar{\mathbf{r}}_\nu = 2(\mathbf{r}_\mu - \mathbf{R}) - 2(\mathbf{r}_\nu - \mathbf{R}) = 2(\mathbf{r}_\mu - \mathbf{r}_\nu)$) and is vital for good performance.

A special case of horizontal recursion where angular momentum is transferred from an $\mathbf{r}_1$-dependent center μ to an $\mathbf{r}_2$-dependent center κ ("transfer recursion")

$$[\boldsymbol{\ell}_\mu\mathbf{0}(\boldsymbol{\ell}_\kappa + \mathbf{1}_i)\mathbf{0}] = [(\boldsymbol{\ell}_\mu + \mathbf{1}_i)\mathbf{0}\boldsymbol{\ell}_\kappa\mathbf{0}] + (r_{\mu i} - r'_{\kappa i})[\boldsymbol{\ell}_\mu\mathbf{0}\boldsymbol{\ell}_\kappa\mathbf{0}] \tag{2.33}$$

is used in place of a second vertical recursion step as mentioned in the previous section. It is called "transfer recursion" because the angular momentum is transferred from an $\mathbf{r}_1$-dependent function to an $\mathbf{r}_2$-dependent function. It is important to note the difference in $\mathbf{R}$-dependence of $\bar{\mathbf{r}}_\mu = 2(\mathbf{r}_\mu - \mathbf{R})$ and $\bar{\mathbf{r}}'_\kappa = 2(\mathbf{R} - \mathbf{r}_\kappa)$ and that the difference as in (2.33) cannot be taken outside of the numerical integration.

2.3.4 Integral prescreening

Integral prescreening at the shell level is applied by factoring the prefactor $K_{\mu\nu\kappa\lambda}$ into a product of overlaps which can be used to exploit the locality of basis functions to discard

entire negligible blocks of integrals

$$K_{\mu\nu\kappa\lambda} = Exp[-\frac{1}{\zeta}(\zeta_\mu\zeta_\nu(\mathbf{r}_\mu - \mathbf{r}_\nu)^2 + \zeta_\mu\zeta_\kappa(\mathbf{r}_\mu - \mathbf{r}'_\kappa)^2 + \zeta_\mu\zeta_\lambda(\mathbf{r}_\mu - \mathbf{r}'_\lambda)^2 + \zeta_\nu\zeta_\kappa(\mathbf{r}_\nu - \mathbf{r}'_\kappa)^2 + \zeta_\nu\zeta_\lambda(\mathbf{r}_\nu - \mathbf{r}'_\lambda)^2 + \zeta_\kappa\zeta_\lambda(\mathbf{r}'_\kappa - \mathbf{r}'_\lambda)^2 + z^2 * (\zeta_\mu r_\mu^2 + \zeta_\nu r_\nu^2 + \zeta_\kappa r_\kappa'^2 + \zeta_\lambda r_\lambda'^2))]. \quad (2.34)$$

Overlap screening is done in a cumulative fashion at each AO shell-index $i, j, k,$ and l. Additional screening from products of exchange-type density matrix elements $D_{ik}D_{jl}$ is also utilized which formally reduces the complexity to $O(N)$, but tends to cause load balancing issues when parallelized.

2.4 Implementation

Using the new recursion relations derived in the previous section, a prototype implementation has been developed for use in the DSCF program[24] of TURBOMOLE.[51] The numerical integration is taken as an adaptation of the ground-state density functional numerical integration code (subroutine `xcrhf`) and was modified to enable more straight-forward parallelization. The analytical integration over the relative coordinate was implemented using a modified version of the two-electron integral code (subroutine `shloop`). To make use of the numerous benefits of modern compilers and to build extensible code, two new modules containing twenty-seven module procedures and five new derived types have been built in `utilmod` containing the entirety of this code. Module `nlxc` handles all things related to numerical integrations, from setting up of the OpenMP parallel region, to constructing the basis functions and density-dependent quantities on the numerical grid. Module `nlint` is responsible for all of the analytical integration subroutines and for contraction of the two-electron integrals with the density matrix.

2.4.1 Numerical integration

Algorithm 1 shows an overview of the numerical integration portion of the newly implemented integration scheme. The numerical integration over the COM coordinate is done using a quadrature based on a Lebedev mesh for the spherical angles and a Chebyshev quadrature of the second kind[48] for the radial grid. The radial grid is divided into atomic cells according to a modified Becke partitioning[52] as implemented in TURBOMOLE.[51,53] For efficient cache usage, integration is done using localized blocks of grid points which is exploited to reduce the number of repeated loops over shell quadruples. The major differences between the regular ground-state integrator and the one presented here is the way in which grid-dependent quantities are stored; the block lengths and offsets that address the molecular grid are precomputed and stored before the loop over blocks. This is an $O(N)$ step with a small prefactor that is done to reduce the amount of necessary communication between each block iteration which makes parallelization more effective. An OpenMP parallel reduce is then invoked where each thread is given the task of integrating an entire shell quadruple over the grid points in the block. Blocks of one-hundred grid points were used resulting in a range of roughly thirty blocks for light atoms to sixty blocks for heavy atoms.[53]

Algorithm 1 Integration of $(\mu\nu|\kappa\lambda)_{block}$ using numerical quadrature

```
for atoms in molecule do
  divide atomic grid points into blocks of size n
  for block in total_blocks of atom do
    save block size, block offset
  end for
end for

!$omp parallel do reduction(E_xc)
for block in total_blocks of molecule do
  compute φ_{i}(R), dφ_{i}(R)/dR ⇒ ρ(R), ∇ρ(R), τ(R)
  compute c_n[ρ, ∇ρ, τ](R), z[ρ, ∇ρ, τ](R)
  compute [μνκλ](R)_block
  E_x+=E_x^block
end for
```

2.4.2 Analytical integration

Computation of $[\mu\nu\kappa\lambda]_{block}$ is the most expensive section, costing $O(N^4)$ for each grid block. The analytical integration over the relative coordinate is performed for entire shell quadruples as shown in Algorithm 2. A shell quadruple consists of all non-redundant combinations of contracted basis functions. Each quadruple is still expanded further into the primitive functions that make up each contracted basis function. Integral pre-screening is done at the contracted level as described in Section 2.3.4. This prescreening allows the algorithm to approach linear scaling asymptotically; however, it is shown that this screening, which allows for entire quadruples to be skipped, has a heavy cost of making parallel load balancing difficult (see discussion below). Intermediates that are reused in the loop structure over the AO-indices (i, j, k, l) are stored in memory. One crucial difference is the removal of the third-center vertical recursion from the loop over primitive functions. While a loop over gridpoints cannot be avoided because of the quadrature-dependence of the difference $\bar{\mathbf{r}}_\mu - \bar{\mathbf{r}}_\kappa$, exploiting the fact that it is independent of the loop over primitive functions is crucial and is increasingly efficient for higher angular momentum integrals.[54]

Algorithm 2 Analytical integration of $[\boldsymbol{\ell}_\mu \boldsymbol{\ell}_\nu \boldsymbol{\ell}_\kappa \boldsymbol{\ell}_\lambda]$

for shell block $ijkl$ **do**
  screen at each loop index
  for primitive loop $\mu\nu\kappa\lambda$ **do**
    for grid points $\mathbf{R}_i$ in block **do**
      compute and store $[\boldsymbol{\ell}_{\mu+\nu+\kappa+\lambda} 000](\mathbf{R}_i)$
    end for
  end for
  for grid points $\mathbf{R}_i$ in block **do**
    compute $\sum_i [\boldsymbol{\ell}_{\mu+\nu} 0 \boldsymbol{\ell}_{\kappa+\lambda} 0](\mathbf{R}_i)$ from $[\boldsymbol{\ell}_{\mu+\nu+\kappa+\lambda} 000](\mathbf{R}_i)$ by horizontal recursion
  end for
  compute $[\boldsymbol{\ell}_\mu \boldsymbol{\ell}_\nu \boldsymbol{\ell}_{\kappa+\lambda} 0]$ from $[\boldsymbol{\ell}_{\mu+\nu} 0 \boldsymbol{\ell}_{\kappa+\lambda} 0]$ by horizontal recursion
  compute $[\boldsymbol{\ell}_\mu \boldsymbol{\ell}_\nu \boldsymbol{\ell}_\kappa \boldsymbol{\ell}_\lambda]$ from $[\boldsymbol{\ell}_\mu \boldsymbol{\ell}_\nu \boldsymbol{\ell}_{\kappa+\lambda} 0]$ by horizontal recursion
  compute $E_x^{block} = \sum_{\mu\nu\kappa\lambda} D_{\mu\nu} D_{\kappa\lambda}\ (\boldsymbol{\ell}_\mu \boldsymbol{\ell}_\nu \boldsymbol{\ell}_\kappa \boldsymbol{\ell}_\lambda)_{block}$
end for

2.5 Results

The results presented here demonstrate the performance of the implementation of the new recursion scheme. All cases were tested both with and without screening as it was found early on that there was a rather strong sensitivity to the screening under initial tests. Integral screening thresholds were set to 10^{-18} in all cases. Calculations were run on Intel Nehalem X5560 2.8GHz CPUs using 2GB of memory per CPU on the local cluster, Greenplanet, unless specified otherwise.

The accuracy of the both the recursion scheme and its implementation were verified by setting range-separation g^{sr} to 1 (or equivalently, the exponent of the short-ranged function to 0). In this case, the full Hartree-Fock exchange should be recovered. Table 2.1 shows the convergence towards the exact number as a function of the numerical grid size. Though the

gridsize	E_x^{HF}
1	-17.885391041237
2	-17.925505714432
3	-17.930387619517
4	-17.934108943249
5	-17.937913901276
exact	-17.9387344473

Table 2.1: Calculation of the exact exchange energy of water dimer using the basis set def2-SVP. The reference exact exchange value is computed self-consistently using the analytical scheme already implemented in TURBOMOLE.

system is on the small side, convergence to tens of mHartree is achieved by using gridsize 2 in TURBOMOLE and μHartree agreement by gridsize 3. This accuracy is sufficient for most applications. Larger grids can be used just verify the accuracy and the cost increases linearly as seen in Figure 2.1.

As a function of gridsize, we see a crossover point between the screened and unscreened protocols in the total wall time of the calculation. For less than 10^5 grid points, there tends to be a lot of overlap between grid-depdendent quantities and therefore not too much is

gained by screening. However, as the mesh becomes finer, it is easier to distinguish regions of space and a 10-15% improvement is observed. Given that NH_3 is such a small system, its performance is less than optimal. This screening is expected to be more effective for larger systems.

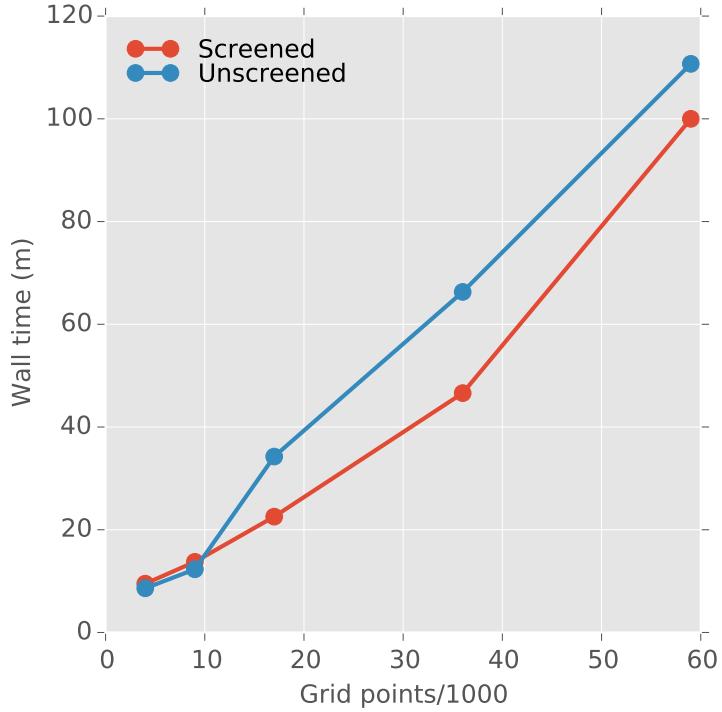

Figure 2.1: Total wall time of a single non-self-consistent iteration for the total energy of NH_3, using the basis def2-TZVP.

A more subtle feature, though important for understanding the performance of the algorithm, comes from the block size. The blocking was initially done as a way to make optimal use of cache and registers for numerical integration of quantities that could not be represented analytically, thus, it was not intended to be used to construct entire two-electron integrals on a grid. The length of the block is ultimately buried within the four-fold loop over primitive functions and unfortunately there is no way to avoid this. In Figure 2.2, the screened and unscreened timings are presented. The optimal block size is around 100 points; any less, and

the overhead of recomputing grid-independent quantities takes over, and any more overflows the caches, sacrificing time to system calls to accommodate the large arrays.

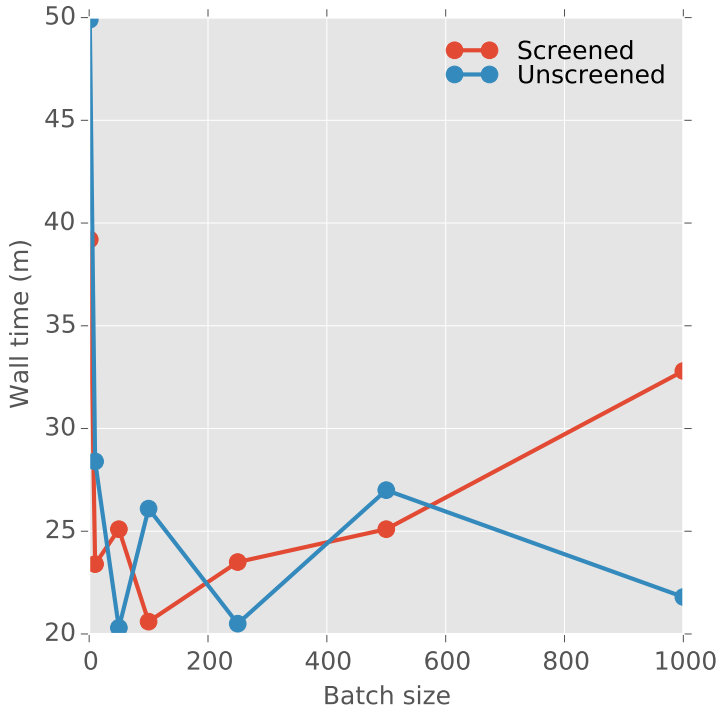

Figure 2.2: Total wall time of a single non-self-consistent interation for the total energy of H_2O using def2-TZVP, grid size 4, and 8 CPUs.

The total computational cost in terms of the basis set should scale formally as $O(N^4)$ if no screening procedures are implemented. Using the permutational symmetry of the integrals reduces the cost by 2^{-3}, one factor of two for each of the different pairing possibilities, i.e. i, j, j, k and k, l. In the present case, screening is only done via the integral prefactor K and its corresponding density matrix contribution. Integral estimates would provide a third way to determine if a block is negligible but would come at the cost of computing a grid-dependent estimate. Since each block of grid points is relatively localized, this may be feasible and is worth considering if the cost is to be brought down further. Screening at the shell level makes a much bigger impact on the analytical integration than on the numerical grid. This is a

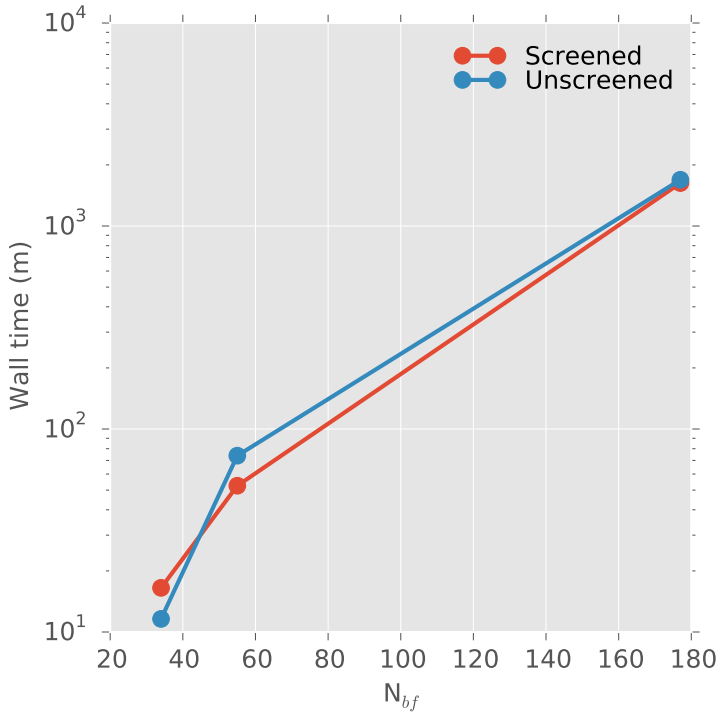

Figure 2.3: Total wall time of a single non-self-consistent iteration for the total energy of CH_4, using three basis sets, def2-SVP, def2-TZVP, def2-QZVP, gridsize 4, and 8 CPUs.

result of the relative expenses of the two different parts: the relative coordinate integration is by far the most expensive portion.

The overall scaling of the algorithm was assessed by computing water clusters $(H_2O)_n$, $n = 1, 2, 3, 4$, as seen in Figure 2.4. For the unscreened case, a power law fit to n^5 is observed, as expected. When screening is employed, a considerable improvement is seen for the $n = 4$ cluster, which only scales as $n^{4.2}$. In the screened case of $(H_2O)_4$, upwards of 30% of shell quadruples were skipped. This is promising for applications to larger systems where the locality of the grid blocks screens most shell quadruples that are not in the vicinity of the grid block.

The performance as a function of the number of processors used was also assessed. Figure 2.5 shows characteristic $1/n_{CPU}$ behavior with an asymptotic limit of around 2000 minutes. In a perfectly parallel scaling algorithm, one would expect the curve to approach 0; however,

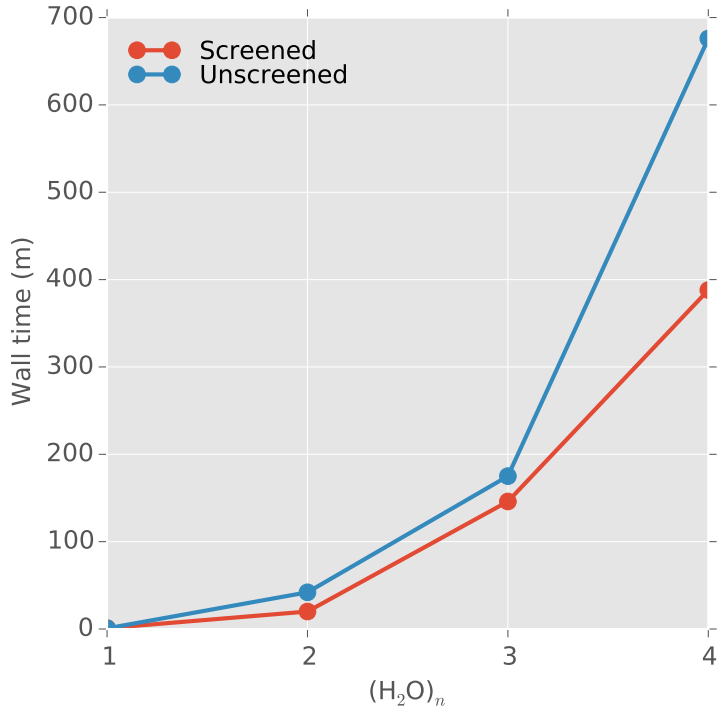

Figure 2.4: Total wall time in minutes for water monomer, dimer, trimer, and tetramer. Calculations were performed using def2-SVP basis sets, grid size 3 and 24 CPUs. Structures were taken from Ref. 55.

in practice, accumulation of thread communication and atomic statements that can only be executed by a single processor leads to diminishing returns.

2.6 Conclusions

The two-electron integral problem in quantum chemistry is still of appreciable importance because they are the core of describing the electron-electron interaction. Developing models for this interaction is crucial to the improvement of approximate density functional methods. While much progress has been made over the past decades to reduce the cost of their computation, development of integral schemes for more complicated interaction kernels has been slow because of the increasingly prohibitive cost of their evaluation. This chapter presented a new perspective on how to extend the literature to new classes of interactions.

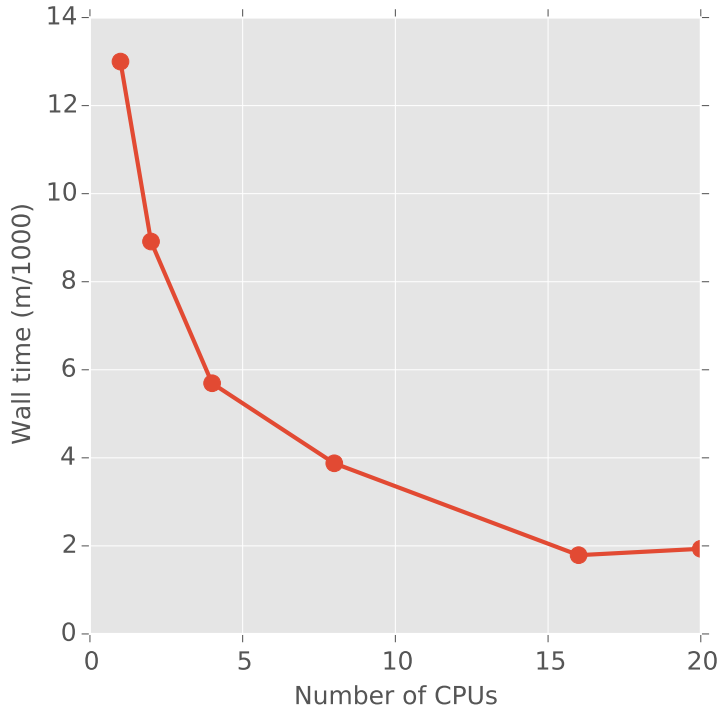

Figure 2.5: Total wall time in minutes$\times 10^{-3}$ as a function of the number of processors for calculation of the total energy of acetone. Calculation employs screening and uses the basis def2-TZVP, and gridsize 3.

A new recursion scheme was derived in order to broaden the scope of computationally tractable models. This is particularly relevant in the density functional community where beyond-semi-local approximations can remedy short comings such as self-interaction error. The scheme stems from a rewriting of the two coordinate's integration in terms of one integral that is parametrically dependent on the other coordinate. This affords a 'simple' integral over the relative coordinate that can be evaluted analytically by a recursion that resembles that of Obara and Saika. Additional polynomial dependence of the interaction kernel on the relative coordinate u is obtained by differentiation of the Boys function. Further generalization would yield an even more flexible recursion scheme applicable to arbitrary powers of the relative coordinate.

The new recursion scheme was implemented via a semi-analytical algorithm and will be made available in the quantum chemistry package TURBOMOLE in the near future. The algorithm

is broken up into two parts: (1) the construction of blocks of density-dependent quantities and (2) the analytical integration over the relative coordinate of the grid-dependent integral (second Eq. (2.9)). Prescreening is done at each shell level of the u integration in order to reduce the number of loops over primitive functions, the most expensive portion of the calculation. The analytical integration is done for blocks of center-of-mass gridpoints, with integration over the grid blocks done in an OpenMP reduction loop. The code is able to fully reproduce the Coulomb energy when no non-locality is included, which is a special case of this more general scheme.

Benchmark tests show that the recursion scheme and its implementation are correct but that its performance is not as good as would be expected. Timing tests on water clusters of increasing size show that the method scales as $O(N^5)$ with a large prefactor and the use of prescreening only lowers the cost to around $O(N^4)$. Based on the use of screening via the exchange density matrix, one would expect asymptotically linear scaling. This is not achieved in practice partially due to the locality of the small systems that were tested but further tests are necessary to discern the root of the observed poor screening. The parallel efficiency is also lower than expected, despite efforts to eliminate communication between threads in the numerical integration. Since each block of grid points is completely independent, the parallel performance is expected to be quite good but in practice we see diminishing returns for more processors. This is, in part, due to the issues with load balancing at the shell level. The relatively low efficiency of the screening and parallelization warrant further investigation to make this integral scheme viable for larger systems.

The integral in Eq. (2.9) may be rewritten in numerous other ways and there may be a benefit to doing a fully numerical scheme in that sums tend to be the most easily parallelized. This would lend itself well to massively distributed calculation on a GP-GPU type architecture. Though some infrastructural changes would need to be made, the increasing availability of large numbers of CPUs may make this alternate route one worth pursuing. In order to

reduce the overall scaling, a resolution-of-the-identity expansion may also prove to be fruitful, though the fact that the two-electron integrals must be computed for the entire molecular grid is a rather steep cost, regardless.

Chapter 3

Locally range-separated hybrids

3.1 Introduction

Hybrid density functionals[56,57] perform well in many chemical applications because they mitigate the negative consequences of self-interaction error[58–60] (SIE) present in all semi-local density functional approximations. One-electron SIE can be removed altogether by the use of 100% of exact exchange but comes at the cost of the description of static correlation, which is captured by semi-local functionals through cancellation between approximate exchange and correlation.[6,61,62] While hybrids often balance SIE and static correlation successfully, a serious concern with their use is the strong dependence of results on the fixed hybrid mixing parameter; optimal amounts of exact exchange have been shown to vary drastically depending on the property of interest.[63,64]

Local hybrid functionals[65–72] introduce a position-dependent mixing parameter which improves upon global hybrids for barrier heights[65] and atomization energies[69] in some systems. However, there is no clear way to construct the local mixing function and this is further hampered by the ambiguity of the exchange energy density,[73–75] making the local mixing

function non-unique. Range-separated hybrid functionals[76–81] (RSH) interpolate between exact and approximate exchange contributions based on the interelectronic distance, r_{12}. To this end, the electron-electron interaction is partitioned into a short- and long-range part using a screening function f, $0 \leq f \leq 1$, such as an exponential[82] or Error function,[77,83,84]

$$\frac{1}{r_{12}} = \frac{1 - f(zr_{12})}{r_{12}} + \frac{f(zr_{12})}{r_{12}}. \tag{3.1}$$

Range separation was inspired by the hypothesis that the local density approximation might be accurate or even exact at short-range[85] and could be balanced with a more appropriate description for long-range exchange interactions;[86] "inverse" hybrids have been successful in condensed matter applications because of the possibility to circumvent the slow convergence of long-range exact exchange.[77] Regardless, the range-separation parameter z is often determined empirically either by fitting to experimental data[87] or chosen to satisfy Koopmans' theorem on a case-by-case basis.[88–90] An obvious route to a first principles RSH is to replace the screening parameter z by a density-dependent screening function $z[\rho, \gamma, \tau](\mathbf{R})$, where $\mathbf{R} = \frac{1}{2}(\mathbf{r}_1 + \mathbf{r}_2)$ is the center-of-mass (COM) coordinate of two electrons and ρ, γ, and τ are the electron density, its gradient and the kinetic energy density, respectively. This ansatz is known as a locally range-separated hybrid (ℓRSH) and a proof-of-concept example has shown promise for thermochemistry.[91]

When constructing a density-dependent model, there are physically-motivated cases that are especially relevant for chemical applications such as uniform scaling to the high-density limit that can be enforced and has been a preferred method in density functional construction for many years.[92–94] In the high-density limit, the electrons approach the weak-coupling or non-interacting limit which is dominated by Hartree-Fock exchange.[58] In the RSH function of Krukau et. al, proper scaling to the high-density limit is not satisfied. The inverse relationship between the scale of different density regimes and the strength of correlation is

intimately tied to the transferability of a density functional approximation.[95,96] A proper-scaling, density-dependent z should be constructed to afford physically meaningful results in limiting cases.[97]

In this chapter, different density-dependent models for the range-separation function are constructed that satisfy exact conditions, bringing reliability and predictibility to range-separated hybrids. In section 3.2, the energy expression for our hybrid is defined and a model for the short-ranged PBE exchange contribution based on a reconstruction of the PBE exchange hole is derived and tested. Section 3.2.1 outlines the desirable properties of a hybrid functional and how they can be obtained from the behavior of a density dependent range-separation function. Section 3.3 describes the different models we constructed and gives a discussion of their formal behaviors. This is followed by results from various test sets and stretching profiles of prototypical cases of strong self-interaction error and static correlation. The chapter is concluded with a brief outlook for future developments in hybrid density functional theory.

3.2 Definition of the locally range-separated hybrid

Our expression for the range-separated exchange-correlation energy is

$$E_{xc}^{lRSH} = E_x^{lr} + E_x^{sr} + E_c^{\mathrm{PBE}} \tag{3.2}$$

where lr denotes long-range contributions and sr denotes short-range contributions. This equation makes no specification about which type of exchange to use in the short-range or the long-range because we attempt to study both; however, it only makes sense to pair exact exchange with DFT exchange so if one chooses long-range exact exchange, we pair this with short-range DFT exchange, and vice versa. In either case, the long-ranged portion is never

explicitly computed but is obtained by subtracting the short-ranged portion from the full-ranged quantity, e.g. $E_x^{lr-\mathrm{HF}} = E_x^{\mathrm{HF}} - E_x^{sr-\mathrm{HF}}$. For short-ranged exact exchange we have

$$E_x^{sr-HF}[\rho] = \int d^3r_1 d^3r_2 \sum_\sigma |\gamma_\sigma(\mathbf{r}_1, \mathbf{r}_2)|^2 \frac{f[\rho](\mathbf{r}_1, \mathbf{r}_2)}{r_{12}} \tag{3.3}$$

where γ is the one-particle density matrix and $f[\rho](\mathbf{r}_1, \mathbf{r}_2)$ is a short-ranged function dependent explicitly on the relative coordinate $u = |\mathbf{r}_1 - \mathbf{r}_2|$ and implicitly on the center-of-mass $\mathbf{R} = \frac{1}{2}(\mathbf{r}_1 + \mathbf{r}_2)$ through its density dependence. For algorithmic purposes, we use $f(u, \mathbf{R}) = e^{-(z(\mathbf{R})u)^2}$ to partition the short- from long-range interactions. The resulting integrals are evaluted using the scheme presented in the previous chapter.

Short-range PBE exchange[98] is computed using a short-ranged version of the GGA exchange-hole model constructed by Ernzerhof and Perdew[99].

$$E_x^{sr-\mathrm{PBE}} = \int d^3r \tilde{F}_x^{\mathrm{GGA}} \varepsilon_x^{\mathrm{LDA}}(\mathbf{r}) \tag{3.4}$$

Here, $\tilde{F}_x^{GGA}$ is the short-ranged version of the PBE enhancement factor over the LDA exchange energy per particle which is defined by

$$-\tilde{F}_x^{\mathrm{GGA}} = \frac{8}{9} \int_0^\infty dy\, y \tilde{J}^{GGA}(s, y). \tag{3.5}$$

The expression for $\tilde{J}^{GGA}$ (Eq. (24) in[99]) uses a further-damped expression for $\mathcal{H}$ (Eq. (A5) in Ref. 99) by the range-separation function z

$$\tilde{\mathcal{H}} = \mathcal{H} + \left(\frac{z^2 k_F}{s}\right)^2 \tag{3.6}$$

where $k_F = (3\pi\rho)^{1/3}$ is the Fermi wavevector and $s = |\nabla\rho|/(2k_F\rho)$ is the reduced gradient. A derivation is presented in Appendix C. This replacement is only made in the final expression

gridsize	E_x^{PBE}
1	-33.074290840165
2	-33.074627143517
3	-33.074663570756
4	-33.074643466785
5	-33.074640122706
ref	-33.074640836132
exact	-33.074632016454

Table 3.1: Calculation of the PBE exchange energy of benzene using the basis set def2-SV(P). The exponent in Eq. (3.6) is set to zero. The PBE exchange reference number is computed self-consistently using the reference grid which uses no procedures for efficiency.

for the exchange-energy density (Eq. A4), leaving their construction of $\mathcal{F}$ and $\mathcal{G}$ unchanged, which is important for maintaining the on-top exchange hole values. The analytic fit for $\mathcal{H}$ presented in Ref. 99 does not exactly reproduce the PBE enhancement factor but the error is less than 0.5% for $s \leq 6.5$. Considering only the short-range portion of $\mathcal{H}$ (small s), we expect errors associated with our modification to be of the same order of magnitude. Table 3.1 shows the total exchange energy as computed by the reconstruction of the PBE exchange-hole. The error for grid sizes that would be typically used in a calculation (grid size 3 to 4) is on the order of tens of microHartree.

3.2.1 Desirable properties of hybrid functionals

With a way to smoothly interpolate between exact and approximate exchange contributions, it is important to understand the way in which this interpolation should be done. Understanding some limiting cases which are well defined will govern the way in which our range-separation function behaves. Here we summarize the conditions we hope to satisfy; they are broadly broken up into two categories: one where Hartree-Fock exchange is appropriate and another where approximate semi-local exchange is. The expression to keep in mind throughout this section, is the balancing of long-ranged and short-ranged contributions

that come from

$$(1 - e^{-zr^2}) + e^{-zr^2}. \tag{3.7}$$

The term in parenthesis by defintion gives us the long-range portion, and the lone exponential gives us the short-range portion. By setting $z \to 0$, $e^{-zr^2} \to 1$ and we cancel the long-ranged exchange (in parenthesis), and by setting $z \to \infty$, $e^{-zr^2} \to 0$ and we remove all of the short-ranged exchange. This forms the basis for how we make z behave to obtain the appropriate limits using semi-local density-dependent quantities.

Hartree-Fock exchange is important and gives a good description of electronics in high-density like systems,[100] one-electron systems,[92] iso-orbital regions,[93,101] and in the tail of the density.[92] One-electron and iso-orbital regions are important because these are the cases where self-interaction error tends to be the highest. A simple example is that of stretched H_2^+, where bond dissociation is poorly described by semi-local functionals unless exact exchange is included (actually, if *only* exact exchange is included). One-electron and iso-orbital regions can be deduced by the positive kinetic energy density $\tau_\sigma(\mathbf{r}) = \frac{1}{2}\sum_i^{N_\sigma} |\nabla\phi_{i\sigma}(\mathbf{r})|^2$ and the von Weisacker kinetic energy density $\tau_W(\mathbf{r}) = |\nabla\rho|^2/(8\rho)$. In these cases, $\tau \to \tau_W$. This condition is often exploited by using the ratio of τ to τ_W. Meta-GGAs such as TPSS use τ as one of its ingredients in order to describe one-electron systems correctly.[93] For the high-density (or weak interaction) limit, we take a density with scaled coordinated $\rho_\lambda(\mathbf{r}) = \lambda^3\rho(\lambda\mathbf{r})$ and take $\lambda \to \infty$. It is well known that in the high-density limit exchange dominates and correlation scales to a constant, giving us the constraint[57,102]

$$\lim_{\lambda\to\infty} E_{xc}[\rho_\lambda]/E_x[\rho_\lambda] = 1. \tag{3.8}$$

Chemical systems tend to be closer to the high-density than the low-density limit which is partially why hybrid functionals have been so successful. The last regime where exact

exchange is important is in the tail of the density. Long-ranged tails of the density are governed by the asymptotic behavior of the Coulomb potential which goes as $1/r$, the distance between electrons. Approximate exchange is governed by e^{-r} behavior[103,104] which falls off much too quickly, giving rise to too-easily delocalized charge densities, a well known deficiency of semi-local functionals.[6]

Semi-local exchange is well behaved for uniform or slow varying systems, and systems with relatively strong static correlations, like that of a low-density system. In the molecular low-density, or strongly-correlated limit, we expect Hartree-Fock to behave quite poorly, whereas semi-local functionals tend to have a reasonable description.[105] For example, stretched H_2 is reasonably described by semi-local functionals due to the fortuitous cancellation of long-ranged correlations.[61,106] Uniform or slowly-varying densities are also well described by semi-local functionals, as the uniform electron gas is the basis for their construction.[86,94,98,107]

Table 3.2 provides a summary of relevant conditions. It shows how these limits may be obtained based on the behavior of the range-separation function z for the cases where one mixes short-range exact exchange with long-range approximate exchange and vice versa. As there are both types of hybrids present in the literature, we are interested in investigating both kinds.

Condition	Desired	srHF-lrPBE	srPBE-lrHF
A. High-density	E_x^{HF}	$z \to 0$	$z \to \infty$
B. One-electron	E_x^{HF}	$z \to 0$	$z \to \infty$
C. Iso-orbital	E_x^{HF}	$z \to 0$	$z \to \infty$
D. Low-density	E_x^{PBE}	$z \to \infty$	$z \to 0$
E. Two-electron	mix	$z \to \infty$	$z \to 0$
F. Uniform density	E_x^{PBE}	$z \to \infty$	$z \to 0$
G. Tail of density	E_x^{HF}	$z \to 0$	$z \to \infty$

Table 3.2: Summary of various well-understood cases that should be obtained with a proper method and how they can be achieved by the behavior of the range-separation function.

3.3 Range-separation functions

In this section, we define the different choices of the range-separation function for two different types of hybrids, one that employs long-range exact exchange with short-range PBE exchange, and another that uses short-range exact exchange with long-range PBE exchange. In terms of computational cost, there is little difference because the most expensive step is the computation of the short-range exact exchange, which is computed in both cases. When using long-range exact exchange, there is a marginally higher cost stemming from computing the full-range exchange integrals, but this is negligible in comparison to the non-local integrations. In the following defintions, we will use w for hybrids that employ short-range PBE exchange and long-range HF exchange, while z will be used for hybrids that have short-range HF exchange and long-range PBE exchange.

3.3.1 Aside: uniform coordinate scaling

We pause briefly to describe the notation which is used to clarify the behavior of our range separation functions under coordinate scaling. The first step is realizing that we are to evaluate a density functional using a scaled density defined by

$$\rho_\lambda(\mathbf{r}) = \lambda^3 \rho(\lambda \mathbf{r}). \tag{3.9}$$

Now, anywhere the density appears, it is replaced by the scaled density ρ_λ. This is then followed be a change of variables $\tilde{\mathbf{r}} = \lambda \mathbf{r}$. Any place where an unscaled coordinate exists, e.g. the Coulomb interaction, a substitution $\mathbf{r} = \tilde{\mathbf{r}}/\lambda$ will be made. For example, the short-ranged

function $f(u, \mathbf{R})$ evaluated on a scaled density yields

$$f^{\lambda}(\tilde{u}, \tilde{\mathbf{R}}) = Exp\left[-(z^{\lambda}(\tilde{\mathbf{R}})(\tilde{u}/\lambda)^2\right] = Exp\left[-(z^{\lambda}(\mathbf{R})/\lambda^2)u^2\right]. \tag{3.10}$$

Hence, the behavior of z^{λ} that we are interested in is z^{λ}/λ^2.

3.3.2 Short-range PBE exchange with long-range HF exchange

Range-separation function of Krukau et al.

A locally range-separated hybrid based on a 'local band-gap' was proposed by Krukau and coworkers.[91] In their work, the range-separation function w^{KSPS}, with dimension of inverse length, is approximated by a gradient expansion in $r_s = (3/(4\pi\rho))^{1/3}$, the Seitz radius,

$$w^{\mathrm{KSPS}} = \frac{1}{r_s}(\alpha + \beta s + \gamma s^2 + \cdots). \tag{3.11}$$

The authors explored the parameter space for α, β, and γ and found optimal results for $\alpha, \gamma \approx 0$, thus their (and our) choice of screening function is

$$w^{\mathrm{KSPS}} = \beta\frac{s}{r_s} = \frac{\beta}{(18\pi)^{1/3}}\frac{|\nabla\rho|}{\rho}. \tag{3.12}$$

Upon uniform coordinate scaling to the high-density limit, the only object to consider is the Seitz radius, $r_s(\mathbf{R})$ which goes to $\lambda^{-1}r_s(\lambda\mathbf{R})$, leading to the scaling relation

$$w^{\mathrm{KSPS},\lambda}/\lambda^2 = \lambda^{-1}w^{\mathrm{KSPS}}. \tag{3.13}$$

This function scales too slow in the high-density limit, yielding $w^{\mathrm{KSPS},\lambda} \to 0$. Proper scaling would require $w^{\mathrm{KSPS},\lambda}$ to scale at least as fast as λ^2.

Range-separation function with proper scaling

We propose a range-separation function with proper behavior under four important limits: (1) uniform scaling, (2) high-density limit, (3) low-density limit, and (4) iso-orbital regions.

A guess for w satisfying these constraints is

$$w_\sigma^{prop}[\rho] = (\varepsilon_{x\sigma}^{mgga})^2 \cdot \left(\frac{\tau_W}{\tau - \tau_W}\right)^2 \cdot a \cdot \ln(1 + b \cdot k_F), \tag{3.14}$$

where τ is the spin-summed kinetic energy density

$$\tau = \frac{1}{2}\sum_\sigma \tau_\sigma \tag{3.15}$$

$$\tau_\sigma = \sum_i^{N_\sigma} |\nabla \phi_{i\sigma}|^2, \tag{3.16}$$

and the von Weisacker kinetic energy density is defined as

$$\tau_W(\mathbf{r}) = |\nabla\rho|^2/(8\rho). \tag{3.17}$$

In the high-density, weak interaction limit ($\lambda \to \infty$), exchange dominates correlation (which goes to a constant) such that

$$\frac{w_\sigma^{prop}[\rho_\lambda]}{\lambda^2} \geq c \cdot \ln\lambda. \tag{3.18}$$

In the low-density, strong-interaction limit ($\lambda \to 0$), GGA exchange and correlation should cancel and corrections to that should vanish:

$$\frac{w_\sigma^{prop}[\rho_\lambda]}{\lambda^2} \sim \lambda. \tag{3.19}$$

In iso-orbital regions ($\tau \to \tau_W$), GGA exchange should vanish which can be satisfied by

$$\frac{w_\sigma^{prop}[\rho_\lambda]}{\lambda^2} \sim \left(\frac{\tau_W}{\tau - \tau_W}\right)^2. \tag{3.20}$$

This also enforces the proper uniform limit $w_\sigma^{prop}[\rho_\lambda]/\lambda^2 \to 0$.

3.3.3 Short-range HF exchange with long-range PBE exchange

Here we define new range-separation functions based on the long-range PBE and short-range HF exchange partitioning that are meant to describe the high density limit, the uniform limit, one-electron systems, iso-orbital regions, and two-electron singlets correctly. We proceed with three different z that are defined as

$$z_1 = \frac{\varepsilon_{xc}^{\mathrm{PBE}}}{s} * (1 - \zeta^2 + \alpha) \tag{3.21}$$

$$z_2 = \frac{\varepsilon_{c}^{\mathrm{PBE}}}{s} * (1 - \zeta^2 + \alpha) \tag{3.22}$$

$$z_3 = \frac{\varepsilon_{xc}^{\mathrm{PBE}}}{t} * (1 - \zeta^2 + \alpha) \tag{3.23}$$

where, $\varepsilon_{xc}^{\mathrm{PBE}}$ is the PBE exchange-correlation energy density,

$$\zeta = \frac{\rho_\alpha - \rho_\beta}{\rho_\alpha + \rho_\beta} \tag{3.24}$$

is the spin-polarization,

$$t = \frac{|\nabla\rho|}{2k_s\rho} \tag{3.25}$$

is the correlation gradient dependent on the Thomas-Fermi wavevector $k_s = \sqrt{4k_f/\pi}$, and

$$\alpha = \frac{\tau - \tau_W}{\tau^{unif}} \tag{3.26}$$

with $\tau^{unif} = (3/10)(3\pi^2)^{1/3}\rho^{4/3}$. α is a scale-invariant function that can distinguish between iso-orbital ($\alpha = 0$), uniform ($\alpha = 1$), and overlapping closed-shell ($\alpha >> 1$) regions. α was proposed for use in density functional approximations in Reference 108 and is related to the electron-localization function.[109]

In our z range-separation functions, one-electron and iso-orbital regions are recognized by $\alpha \to 0$. Two-electron singlets are also recognized by $\alpha \to 0$ because $\tau \to \tau_W$. Use of τ-dependent quantities in local hybrids[69,70] could isolate one-electron and two-electron singlets from other density regions but is unable to distinguish them. By introducing the spin-polarization ζ, a two-electron singlet $\zeta \to 0$ can be distinguished from one-electron systems $\zeta \to 1$. For uniform densities, $s \to 0$, such that $z \to \infty$. Though we are able to capture some same-spin correlation effects but the use of ζ, the scope may be slightly overextended, especially being incorporated into an exchange-type framework. However, it has been proposed that static-correlation effects scale to the high-density limit almost as fast as exchange[110] and thus could be an effect worth incorporating into an exchange-type functional.

Now, we insert z into our short-ranged Gaussian function in order to analyze its behavior under coordinate scaling. For z_1, using the fact that $\varepsilon_{xc}^{\mathrm{PBE}} = \varepsilon_x^{\mathrm{PBE}} + \varepsilon_c^{\mathrm{PBE}}$, we obtain the function

$$f_1(u, \mathbf{R}) = Exp\left[-\frac{1}{s^2}(1 - \zeta^2 + \alpha)^2 * ((\varepsilon_x^{\mathrm{PBE}})^2 + (2\varepsilon_x^{\mathrm{PBE}}\varepsilon_c^{\mathrm{PBE}}) + (\varepsilon_c^{\mathrm{PBE}})^2) * u^2\right]. \quad (3.27)$$

The subscript on f corresponds to the subscript of z. Since s, α, ζ are all dimensionless and therefore scale-less quantities, the only pieces that we are interested in analyzing are $\varepsilon_{xc}^{\mathrm{PBE}}$ and t. Using scaled coordinates, this translates to

$$f_1^{\lambda}(\tilde{u}, \tilde{\mathbf{R}}) = Exp\left[-\frac{1}{s^2}(1 - \zeta^2 + \alpha)^2 * ((\varepsilon_{x\lambda}^{\mathrm{PBE}})^2 + (2\varepsilon_{x\lambda}^{\mathrm{PBE}}\varepsilon_{c\lambda}^{\mathrm{PBE}}) + (\varepsilon_{c\lambda}^{\mathrm{PBE}})^2) * (\tilde{u}/\lambda)^2\right]. \quad (3.28)$$

The scaling behavior of $\varepsilon_{x\lambda}^{\mathrm{PBE}}$ and $\varepsilon_{c\lambda}^{\mathrm{PBE}}$ are known with $\varepsilon_{x\lambda}^{\mathrm{PBE}} \rightarrow \lambda\varepsilon_{x}^{\mathrm{PBE}}$ and $\varepsilon_{c\lambda}^{\mathrm{PBE}} \rightarrow C$.[57] Overall, the scaling behavior will be dominated by the product of $\varepsilon_{x}^{\mathrm{PBE}}$ and $\varepsilon_{c}^{\mathrm{PBE}}$, with this term scaling as $1/\lambda$. So, as $\lambda \rightarrow \infty$, $f_1^{\lambda} \rightarrow 0$.

For z_2, a similar analysis leads to the conclusion that as $\lambda \rightarrow \infty$, $f_2^{\lambda} \rightarrow 0$ as $1/\lambda^2$. For z_3, we replace the dimensionless gradient s by the correlation gradient t which scales with the density as $1/\lambda$ yielding

$$f_3^{\lambda}(\tilde{u}, \tilde{\mathbf{R}}) = Exp\left[-\frac{1}{t^2}(1-\zeta^2+\alpha)^2 * ((\varepsilon_{x\lambda}^{\mathrm{PBE}})^2 + (2\varepsilon_{x\lambda}^{\mathrm{PBE}}\varepsilon_{c\lambda}^{\mathrm{PBE}}) + (\varepsilon_{c\lambda}^{\mathrm{PBE}})^2) * (\tilde{u}/\lambda)^2\right], \quad (3.29)$$

which leads to the conclusion that $f_3^{\lambda} \rightarrow 1$ as λ^2 because the λ dependence of $1/t^2$ and $(\tilde{u}/\lambda)^2$ cancel, leaving the scaling behavior of $\varepsilon_{x\lambda}^{\mathrm{PBE}}$ as the dominant term.

3.3.4 Summary of the different range-separation functions

Having described the different range-separation functions, we now give a brief summary of their behavior in the cases mentioned in section 3.2.1. The energy contribution is determined by imposing the given condition for w or z in Eq. (3.8). A checkmark ✓is used to indicate that the exact condition is met, while an $\times$ means the condition was not satisfied properly.

Condition	Desired	w^{KSPS}	w^{prop}	z_1	z_2	z_3
A. High-density	E_x^{HF}	$\times$	✓	✓	✓	$\times$
B. One-electron	E_x^{HF}	$\times$	✓	✓	✓	✓
C. Iso-orbital	E_x^{HF}	$\times$	✓	✓	✓	✓
D. Low-density	E_x^{PBE}	$\times$	✓	$\times$	$\times$	$\times$
E. Two-electron	mix	$\times$	$\times$	✓	✓	✓
F. Uniform density	E_x^{PBE}	✓	✓	✓	✓	✓
G. Tail of density	E_x^{HF}	✓	$\times$	$\times$	$\times$	$\times$

Table 3.3: Summary of the different limits satisfied by the various range-separation functions defined in this chapter.

3.4 Computational details

The performance of the locally range-separated hybrids was assessed for atomization energies, ionization potentials, barrier heights and electron affinities. Ionization potentials, electron affinities, and barrier heights were taken from the G21IP, G21EA, BH76 and BH76RC subsets of the GMTKN30 test set.[111] Atomization energies tests were taken from the HEAT[112] and AE6 subset of the MGAE109[113] test sets. Calculations were performed with a development version of TURBOMOLE[51] using triple-zeta quality basis sets[114] (def2-TZVP) and very fine quadrature grids[53] (gridsize 4). Tightly-converged TPSS orbitals (energy to 10^{-8}a.u. and densities to 10^{-10}a.u.) were used as input to the non-self-consistent calculations. The effect of different orbitals was also tested, showing a small effect on the order of 10's of mH between hybrids, semi-local functionals, and Hartree Fock. Overall, the more exact exchange included in the orbitals, the higher the energy of the short-ranged HF exchange, and the more negative the semi-local contributions.

Method	$E_x^{sr-\mathrm{HF}}$	$E_x^{lr-\mathrm{PBE}} + E_c^{\mathrm{PBE}}$
PBE	-1.95944	-18.12771
PBE0	-1.94749	-18.14143
B-P	-1.95889	-18.13628
B3-LYP	-1.95535	-18.14233
TPSS	-1.95148	-18.14902
TPSSH	-1.94757	-18.15240
HF	-1.92651	-18.15605

Table 3.4: Range separated two-electron energy (in Hartree) of F_2 using different methods to compute the input orbitals, range-separation function z_1, def2-TZVP basis sets, and grid size 3.

Each range-separation function has a single multiplicative scale parameter β in order to give reasonable thermochemical results. The "optimal" parameter is given in Table 3.5 for each was determined by scanning the error in the atomization energy of water across six orders of magnitude. Given that closed-shell water is not the most strongly-correlated

system, a different parameter may fit better for accurate results for systems with strong static correlations.

	β
w^{KSPS}	0.02
w^{prop}	100
z_1	50
z_2	0.1
z_3	0.5

Table 3.5: Optimized scaling factors for the range-separation functions

3.5 Results

The different hybrids were tested on a variety of testsets that are meant to give a general description of thermochemistry. In all cases, Hartree-Fock has the largest error, and it is always an underestimate due to the lack of correlation. PBE and PBE0 significantly improve upon HF, but their performance, as is well known, tends to vary based on the property at hand; semi-local functionals have a difficult time describing anions that can be traced to the delocalization problem[6] and exact exchange tends to remedy that. The range-separated hybrids perform reasonably in most cases. The RSH of Krukau et. al does quite well for electron affinities, ionization potentials, and atomization energies. The z RSH more closely resembles HF-like numbers, in that the including too much exact exchange deteriorates the quality of the property. Comparing the RSH that use the different range partitioning, we see that short-range PBE with longe-ranged HF exchange on average does better than the inverse partitioning.

For the AE6 test set, the well-known underbinding for Hartree-Fock comes as no surprise, with every atomization energy being considerably too small. The performance of the locally RSHs also shows a similar trend: the mixing of HF exchange tends decrease the atomization

Testset	Ref	HF	PBE0	PBE	w^{KSPS}	w^{prop}	z_1
G21EA	-220.9	31.6	7.86	6.60	5.52	18.1	22.6
G21IP	257.6	20.4	3.75	3.91	4.55	7.6	14.1
AE6	390.9	126.4	4.91	14.3	5.2	22.8	17.1
HEAT	-212.5	86.9	2.97	9.09	7.50	17.8	30.2

Table 3.6: Performance of lrsh for various molecular properties. The reference values are the average of the test set and each method column is the mean absolute error in kcal/mol for that test set.

energy with respect to its semi-local GGA counterpart. In the limit as $z \to 0$, RSHs approach the GGA atomization energies, while $z \to \infty$ approaches Hartree-Fock plus semi-local correlation.

Molecule	Ref	HF	PBE0	PBE	z_1
SiH_4	322.3	-69.21	-7.30	-9.38	-22.6
SiO	192.0	-90.56	-10.49	3.69	-30.0
HCOCOH	633.3	227.79	0.34	29.60	-6.6
C_3 H_4	704.7	188.24	1.65	15.59	-21.3
S_2	101.6	-56.61	4.73	13.53	4.9
MAE		126.4	4.91	14.3	17.1
MSE		-126.4	-2.21	10.6	-15.1

Table 3.7: Atomization energies of small organics and inorganics. Values in kcal/mol.

Ionization potentials of some small molecules and atoms were computed with the results in Table 3.8. In this case, the statistics are not especially valuable due to the sample size. For the z RSHs, their performance closely mimicks that of Hartree-Fock, with minor improvements. The hybrids that use short-range PBE exchange instead, have a slightly more difficult time than even Hartree-Fock because the larger nuclear charge localizes the electron density and is more high-density like.

It should be noted that calculations using the proper-scaling z RSH performed on the HEAT testset yielded widely varying results. Errors in atomization energies tended to be anomalously large ($\sim$100 kcal/mol) for fluorine containing compounds. The exact cause of this large error was traced to poor energies of the fluorine atom itself. The fluorine atom was probed in

Molecule	Ref	HF	PBE	PBE0	w^{KSPS}	w^{prop}	z_1
O_2	277	279	281	285	289	270	278
PH	234	222	235	237	237	235	231
S_2	215	213	216	220	221	216	216
Li	123	123	129	128	131	221	114
O	314	276	323	318	320	306	335
C	260	249	266	265	265	223	265
MSE		-10.2	4.5	5	6.7	8	2.7
MAE		10.8	4.5	5	6.7	25.3	6.7

Table 3.8: Ionization potentials of small molecules and atoms. Values in kcal/mol.

a variety of ways but its cause is still under investigation. It is known that semi-local density functional approximations have a difficult time describing atomic systems. This hypothesis was excluded by studying the effect of input orbitals on the two-electron range-separated energy. Using Hartree-Fock, there was only a 20mH difference in the resulting energy. Between a semi-local (m)GGA and its hybrid variant, there was a difference of 10mH. The finest DFT grid available in TURBOMOLE was also used to exclude the possibility of errors due to the numerical integration. Basis sets modified to not contain steep basis functions, which are known to be difficult to integrate numerically, still resulted in extremely poor atomization energies. To this end, it is still unclear as to what causes the inaccurate total energy of fluorine atom.

In the case of the dissociation of H_2 molecule, the proper-scaling hybrids do not afford the correct limit of two hydrogen atoms and improve only marginally over Hartree-Fock. However, near the equilibrium bond distance, the behavior is significantly improved over Hartree-Fock and closely resembles PBE which gives good binding energies. It is also important to note that the hybrid PBE0 worsens the stretched-limit behavior.

For all of the proper-scaling hybrids, the correct dissociation limit of H_2^+ is recovered due to the α and ζ behaviors. The binding energy is slightly too large because of the inclusion of PBE correlation, but the curves closely follow the HF curve, which is exact for this system. The RSH of Krukau et. al, which does not scale to the high density limit or contain

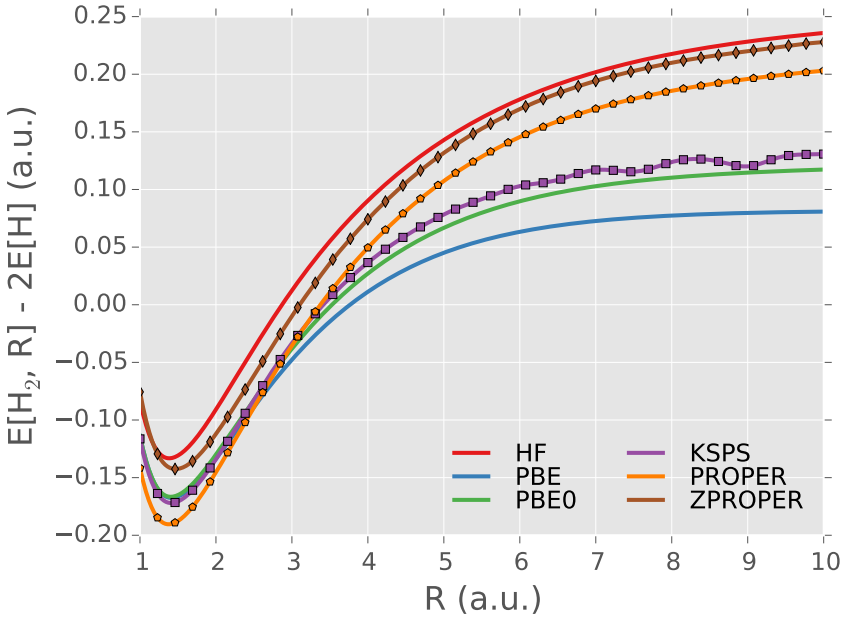

Figure 3.1: Ground state potential energy surfaces of H_2 computed using TPSS input orbitals, def2-TZVP basis sets and gridsize 3.

ingredients to distinguish one-electron systems does not dissociate the molecule correctly but it does improve upon PBE and its hybrid variant PBE0.

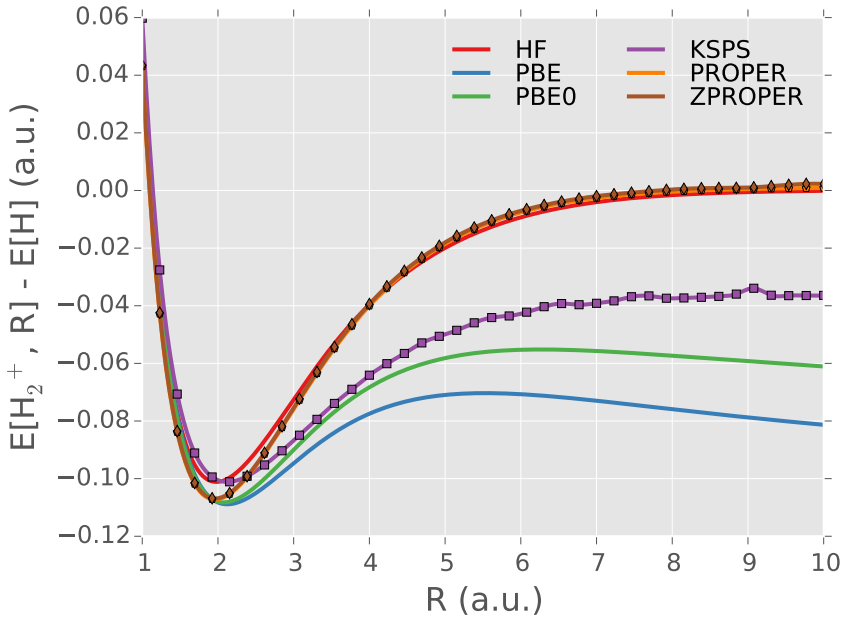

Figure 3.2: Ground state potential energy surface of H_2^+ computed using TPSS input orbitals, def2-TZVP basis sets and gridsize 3.

The previous examples of stretched H_2 and H_2^+ demonstrate the inherent tradeoff between self-interaction error and static correlation. While the hybrids that properly scale to the high-density limit, or non-interacting limit, are able to completely cancel the Coulomb self interaction, this makes it difficult to simultaneously describe the near-degeneracy of the HOMO and the LUMO of H_2 at the dissociation limit. Methods that only scale weakly to the high density limit like the RSH of Krukau et. al, are able to better describe the static correlation in stretched H_2 but cannot dissociate H_2^+.

3.6 Conclusions

Hybrid functionals have been a major player in the main-group quantum chemistry field for many years due to their touted performance in thermochemical measures. Their underlying behavior, however, is less than satisfactory because of the extremely strong dependence on the global hybrid mixing parameter. It is still unclear from a first principles perspective what the optimal value should be. This tends to have a more pragmatically accepted answer in that however much is necessary should be used. Recent work in the development of hybrid functionals has led us down the path to local and range-separated hybrids. These approximations take a more physically intuitive approach and are less empirically driven by virtue of explicitly incorporating physics into their construction.

Here, we proposed and benchmarked new range-separated hybrids that scale properly to the high-density limit in addition to satisfying other known limits of electronic systems. We computed a variety of thermochemical measures and compare them to the first reported 'locally range-separated hybrid' constructed by Krukau et. al. which was also implemented. It is clear that satisfying the high-density limit condition is not sufficient for highly accurate calculations of ionization potentials or atomization energies; however, a functional that does satisfy this limit tends to have predictable behavior for a variety of systems. In the case of

systems where static correlation, or near-degeneracies, are present, the functionals behave modestly, improving on Hartree-Fock, which is a total failure for atomization energies, but still could be improved further. A more flexible model that is able to capture the non-locality of static correlation would be a welcome partner to proper scaling exchange functionals.

Chapter 4

Real-space models of the static exchange kernel

4.1 Introduction

Kohn-Sham density functional theory[107] (DFT) has had a major impact on the field of computational sciences due to the relatively simple nature of the approximations and resulting low computational cost. Modeling hundreds to thousands of atoms using DFT has become routine[115] and the number of DFT citations is still growing rapidly.[116] However, the fact that there are so many different approximate functionals, each constructed with a particular property in mind, points to a theoretical deficiency. Semi-local functionals, as the name implies, are local functionals of the electron density evaluated with a model for the non-locality; approximations are made to incorporate non-local effects implicitly, e.g. by modeling the exchange-correlation hole. This has major ramifications in the calculation of properties and the widespread use of these methods only provides us with more examples of fundamental failures of semi-local approximations.

Constructing a correlation energy functional that is compatible with exact exchange has been tremendously difficult because the full non-locality of the exchange potential is challening to mimic in a semi-local correlation approximation. The random-phase approximation (RPA) provides such a non-local framework and is seamlessly compatible with exact exchange. It is also praised for its balanced description of long-ranged,[117] weak, and noncovalent interactions.[118,119] RPA's recent revival has been due to the advancements in reducing its computational cost.[118,120–123] With efficient algorithms becoming widely available, RPA is being applied to systems that were impossible to treat with conventional perturbative many body methods, where (near-)zero gaps cause a divergence in the correlation energy. It is also being thoroughly studied from a theoretical perspective, with links to ring coupled-cluster methods.[124,125]

Despite its ability to qualitatively describe challenging cases such as the multiple bond breaking in N_2, RPA tends to struggle with processes that do not conserve electron pairs; atomization energies of small molecules are often grossly underestimated.[126] These cases tend to be dominated by short-range correlations[127] that arise from, e.g. separating spatially neighboring spin-paired electrons. The combination of RPA correlation with a short-ranged semi-local correlation did little to improve atomization energies in finite systems, though.

In this Chapter, a non-local short-ranged exchange kernel is constructed and benchmarked. The underlying theoretical foundation is described in Section 4.2 A brief divergence is made to address the issue of instabilities that result from the inclusion of an exchange kernel in the RPA. The form of the kernel using two different short-ranged functions are presented in Section 4.3. A discussion of the implementation in MPGRAD is presented in Section 4.4 and preliminary results on some small systems are given in Section 4.5.

4.2 Theory

4.2.1 The Random-Phase approximation

There are many formulations of RPA available in the literature.[128–132] Here, we adopt the adiabatic-connection fluctuation-dissipation theorem (ACFDT) in a DFT context[133] as it provides a direct representation of the exchange-correlation kernel of interest. The exchange correlation energy is defined in terms of an integral over couling strength

$$E_{xc}[\rho] = \int_0^1 d\alpha\, W_\alpha[\rho]. \tag{4.1}$$

The coupling strength integrand W_α is defined as

$$W_\alpha[\rho] = \langle \Psi_\alpha | \hat{W} | \Psi_\alpha \rangle - \frac{1}{2} \int d^3r_1 d^3r_2 \frac{\rho(\mathbf{r}_1)\rho(\mathbf{r}_2)}{|\mathbf{r}_1 - \mathbf{r}_2|} \tag{4.2}$$

where $\hat{W}$ denotes the operator of the Coulomb interaction, and Ψ_α is the ground state of an N electron system with scaled interaction $\alpha\hat{W}$, whose ground state density is constrained at the density r of the physical ground state Ψ_1. W_α can be written in terms of the imaginary part of the linear density-density response function[86,134]

$$W_\alpha = W_0 - \Im \int_0^\infty \frac{d\omega}{2\pi} \int dx_1 dx_2 \frac{\chi_\alpha(x_1, x_2; \omega) - \chi_0(x_1, x_2; \omega)}{|\mathbf{r}_1 - \mathbf{r}_2|}. \tag{4.3}$$

Here, $\chi_\alpha(\omega)$ is the frequency-dependent density-density response function of a system with interation scaled by α and its density fixed at the physical density for all α, $\chi_0(\omega)$ is the Kohn-Sham non-interacting response function, and $x = (\mathbf{r}, \sigma)$ is a spin-space coordinate. χ_α can be obtained by solving a Dyson-type equation

$$\chi_\alpha(x_1, x_2; \omega) = \chi_0(x_1, x_2; \omega) + \int dx dx' \chi_0(x_1, x; \omega) f_\alpha^{Hxc}(x, x'; \omega) \chi_\alpha(x', x_2; \omega) \tag{4.4}$$

where

$$f_\alpha^{Hxc}(x_1, x_2; \omega) = \frac{\alpha}{|\mathbf{r}_1 - \mathbf{r}_2|} + f_\alpha^{xc}(x_1, x_2; \omega) \tag{4.5}$$

is the frequency-dependent Hartree-exchange-correlation kernel at coupling strength α which is decomposed into the Hartree and exchange-correlation contribution.[61] The Dyson-type equation can be inverted to give

$$\chi_\alpha(x_1, x_2; \omega) = \frac{\chi_0(x_1, x_2; \omega)}{[1 - \chi_0(x_1, x_2; \omega) f_\alpha^{Hxc}(x_1, x_2; \omega)]}. \tag{4.6}$$

The density-density response function can be expressed as the diagonal part of $\mathbf{\Pi}_\alpha$, the causal polarization propagator

$$\chi_\alpha(x_1, x_2; \omega) = \mathbf{\Pi}_\alpha(x_1, x_1, x_2, x_2; \omega). \tag{4.7}$$

$\mathbf{\Pi}_\alpha$ is a 2×2 supermatrix of dimension $2\times N_{ph}$, where N_{ph} is the dimension of the particle-hole space. The polarization propagator also satisfies an inverse matrix equation, more commonly known as the Bethe-Salpeter equation

$$\mathbf{\Pi}_\alpha(\omega) = \left[\mathbf{\Pi}_0(\omega)^{-1} - \alpha\mathbf{V} - \mathbf{K}_\alpha(\omega)\right]^{-1} \tag{4.8}$$

where $\mathbf{V}$ is the bare Coulomb interaction and $\mathbf{K}_\alpha(\omega)$ is a four-point kernel corresponding to a spatially non-local interaction. The direct (exchange-less) RPA is defined by taking the exchange-correlation kernel f_α^{xc} or K_α to zero yielding the corresponding equation for the RPA response function

$$\chi_\alpha^{RPA}(\omega) = \chi_0(\omega) + \chi_0(\omega)\left(\frac{\alpha}{|\mathbf{r} - \mathbf{r}'|}\right)\chi_\alpha^{RPA}(\omega). \tag{4.9}$$

4.2.2 Beyond RPA: exchange-correlation kernels

Despite RPA's success, there are still fundamental issues with its use. For example, when processes involving a change in the number of pairs of electrons, RPA tends to overbind due to spurious self-correlation. The self-correlation problem can be fixed by including exchange contributions. This is in analogy to the one-electron self-interaction error problem in DFT where the use of approximate exchange fails to cancel the electron's self-interaction that arises from the form of the Coulomb energy. Given the demonstrated good long-ranged behavior of RPA, it makes sense to add a short-ranged correction. This idea is not new and numerous attempts at combining long-ranged RPA correlation with short-ranged semi-local correlation corrections have been made.[127,135] The Petersilka-Grossman-Gross (PGG) exchange kernel is exact for one- and two-electron systems and behaves well at short-range.

When correcting the self-correlation problem of RPA, the issue of instabilities often arise[131]. This is especially true in the RPAX formulation, where the exact exchange kernel is included, and the SOX formulation, where exchange to second-order is included. The condition for a stable ground-state correlation energies and real (not imaginary) excitation energies within the ACFDT is

$$\int d^3r_1 d^3r_2 \tilde{\rho}_\sigma(\mathbf{r}_1) f_{\sigma\sigma}^{Hxc}(\mathbf{r}_1, \mathbf{r}_2) \tilde{\rho}_\sigma(\mathbf{r}_1) \geq 0 \tag{4.10}$$

where $\tilde{\rho}$ is an arbitrary density fluctuation. Recently, a renormalization of the non-interacting reference that enters the RPA equations was presented.[136] This amounted to a refactorizing of the matrix inverse that appears in the Bethe-Salpeter equation. This helps to avoid instabilities that arise from (near-) orbital degeneracies that come from the input reference state.

The renormalized beyond-RPA correction is computed conveniently in a molecular basis by rewriting the propagator in terms of the transition vectors

$$\Delta E_c^{b-RPA} = -\int_0^1 d\alpha \sum_{n,m} \alpha \frac{\left[(\mathbf{X}+\mathbf{Y})_m^{\alpha,T}\mathbf{B}^H(\mathbf{X}+\mathbf{Y})_n^{\alpha}\right]\left[(\mathbf{X}+\mathbf{Y})_n^{\alpha,T}\mathbf{K}_\alpha(\mathbf{X}+\mathbf{Y})_m^{\alpha}\right]}{\Omega_n^\alpha + \Omega_m^\alpha}. \quad (4.11)$$

Here, Ω_n^α and Ω_m^α are the interacting excitation energies and $\mathbf{X}_m^\alpha, \mathbf{Y}_m^\alpha$ are the interacting transition vectors. The renormalization removes the bare (unscreened) energy eigenvalue differences in the denominator and replaces them with the dressed (screened) orbital energy differences which dramatically decreases the severity of instabilities due to the reference state.

4.3 Non-local exchange kernels

The form of our exchange kernel was constructed by Ruszinsky and Perdew of Temple University. Our model exchange kernel is meant to satisfy the following constraints: (1) exactness for one-electron systems, (2) the correct high-density limit of two-electron singlets and the uniform electron gas, (3) real and symmetric under interchange of coordinates, and (4) proper spin resolution. Based on these constraints, two ansatz containing different short-ranged functions are

$$f_{\sigma\sigma'}^{x,Erf}(\mathbf{r}_1,\mathbf{r}_2) = -\delta_{\sigma\sigma'}\left[(1-x_\sigma)\mathrm{Erfc}[\sqrt{\tilde{c}(1-z_\sigma)^2}k_{F\sigma}|\mathbf{r}_1-\mathbf{r}_2| + x_\sigma]\right]/|\mathbf{r}_1-\mathbf{r}_2| \quad (4.12)$$

$$f_{\sigma\sigma'}^{x,Gaus}(\mathbf{r}_1,\mathbf{r}_2) = -\delta_{\sigma\sigma'}\left[(1-x_\sigma)e^{-\tilde{c}(1-z_\sigma)^2k_{F\sigma}^2|\mathbf{r}_1-\mathbf{r}_2|^2} + x_\sigma\right]/|\mathbf{r}_1-\mathbf{r}_2|. \quad (4.13)$$

Here, $z_\sigma = \tau_\sigma^W/\tau$ and $\tilde{c} = 0.625$ is used to obtain the correct second-order exchange energy of the uniform electron gas which is the high-density correction to the RPA correlation energy

per electron and

$$x_\sigma = \frac{bs_\sigma^4}{1 + bs\sigma^4} \tag{4.14}$$

where, $s_\sigma = |\nabla\rho|/2k_F\rho$ is the reduced gradient and b is a positive constant.

For one-electron systems, $z \to 1$ such that $f^x \to -1/|\mathbf{r}_1 - \mathbf{r}_2|$ which correctly cancels the RPA correlation contribution. For uniform systems, the reduced gradient $s \to 0$, leaving only the short-ranged portion that is fit via $\tilde{c}$ to recover the correct high-density limit correction to RPA. Its dependence only on the relative and center-of-mass coordinates forces the kernel to be symmetric under interchange of coordinates. For two-electron singlets, it is able to reproduce the results from the kernel of Petersilka, Grossman, and Gross.[137]

4.4 Computational details

All calculations were performed with a locally-modified version of MPGRAD.[138] MPGRAD computes Coulomb integrals on the fly in the AO basis, followed by a transformation to the MO basis before contraction with the first-order pair density. This has an asymptotic $O(N^5)$ scaling and is routine for basic second-order Møller-Plesset calculations. In our modified version, an addition N^5 call is made in order to compute the non-local integrals in the AO basis which are evaluated by the methods described in Chapter 2. The evaluation of the non-local integrals adds an additional $O(N)$ to the overall cost, bringing the total scaling to $O(N^6)$. With transformed integrals, diagonalization of M_α for each of the 7 α of the Gauss-Legendre quadrature, is the next most expensive step (see Ref. 126, Eq. 24). For calculations using the RPA-renormalized framework, only a simple modification to use the matrix containing the new non-local exchange integrals was necessary. Contraction with the second-order pair density yields the renormalized NEO correlation energy. Calculations are

all performed in C_1 symmetry on a single Intel Nehalem X5560 2.8GHz processor using 5GB of memory. Tightly converged TPSS orbitals (10^{-10} a.u for density, 10^{-9} a.u. for energy) are used as input to the post-Kohn-Sham calculations. A single SCF iteration of Hartree-Fock is performed on the same TPSS orbitals in order to compute the Hartree-exchange contributions to the electron-electron interaction.

4.5 Results

The behavior of the NEO kernels and other RPA-based methods are assessed for the stretching of H_2 and H_2^+, Figure 4.1. As expected, the NEO kernels are exact for H_2^+ due to the behavior of z. They significantly improve over Hartree-Fock for stretched H_2, but the effect of exchange in raising the correlation energy makes the dissociation limit worse than in RPA, which is known to describe static correlation well. Again, this is another case where reducing the self-interaction error comes at the cost of describing static correlation.

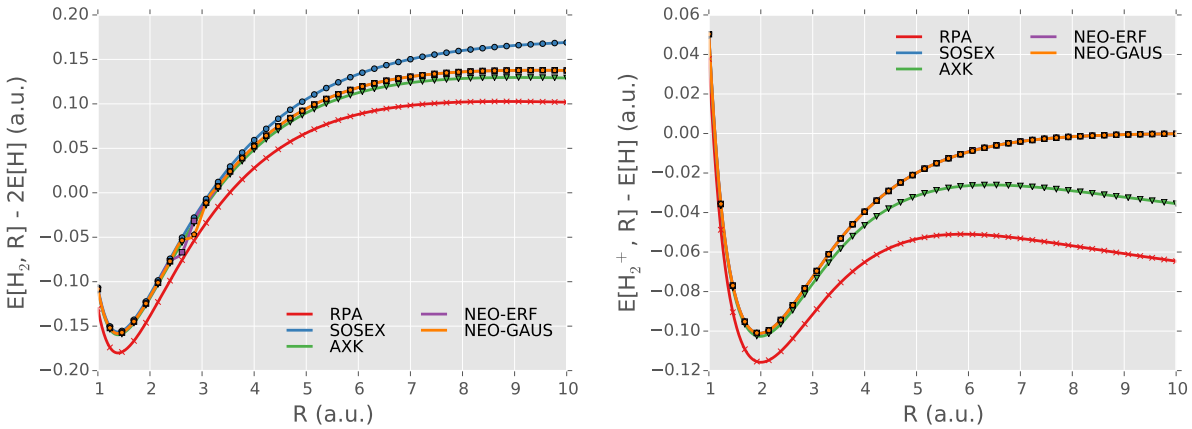

Figure 4.1: Potential energy surfaces of H_2 (left) and H_2^+ (right). Calculations were performed using def2-TZVP basis sets and gridsize 3.

Analyzing the behavior of the coupling-strength integrand gives us an idea of how our approximation behaves. At equilibrium, the coupling strength integrand of RPA is by far the

largest, which gives rise to the largest binding energy. Including exchange corrections of any kind raises the two-electron energy. At stretched distances, RPA retains the necessary curvature to describe the strong static correlation due to the near-degeneracy of the bonding and antibonding orbitals of H_2. The other methods significantly underestimate the correlation energy for this particular geometry.

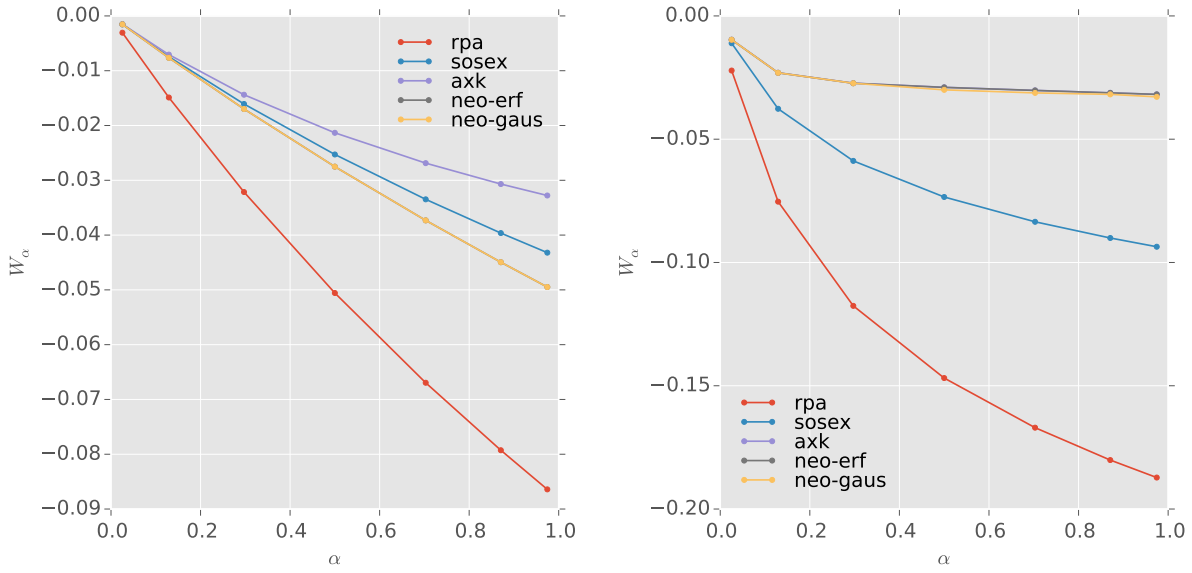

Figure 4.2: Coupling-strength decomposition of H_2 at equilibrium (left) and stretched (right) bond distances.

For the coupling-strength decomposition of H_2^+, there is little to note in the NEO integrand because it, like SOSEX, is exact for one-electron systems. The area between the curve and 0 is exactly 0 for both the stretched and equilibrium bond distances as it should be for one-electron systems. Additionally, it is seen that AXK significantly improves on RPA at the equilibrium bond distance but has a little effect on the dissociated limit.

In the case of the dissociation curve of He_2^+, the NEO kernels behave fairly well, giving close to the exact solution of He + He^+. However, the fluctuations in the Gaussian NEO kernel arise from instabilities, which are neglected in their contribution to the total correlation energy.

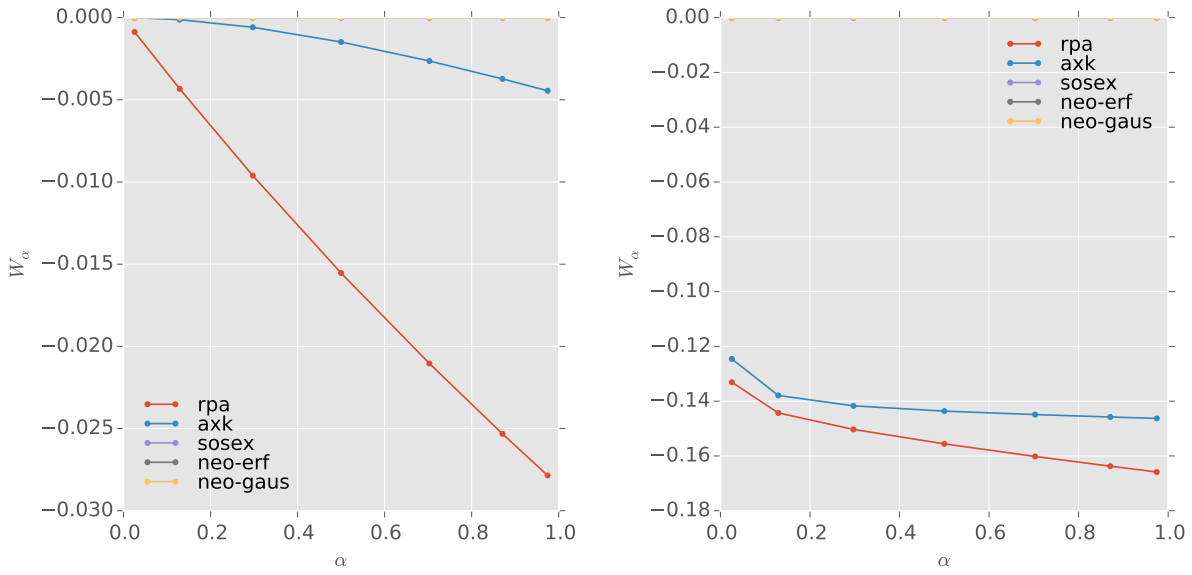

Figure 4.3: Coupling-strength decomposition of H_2^+ at equilibrium (left) and stretched (right) bond distances.

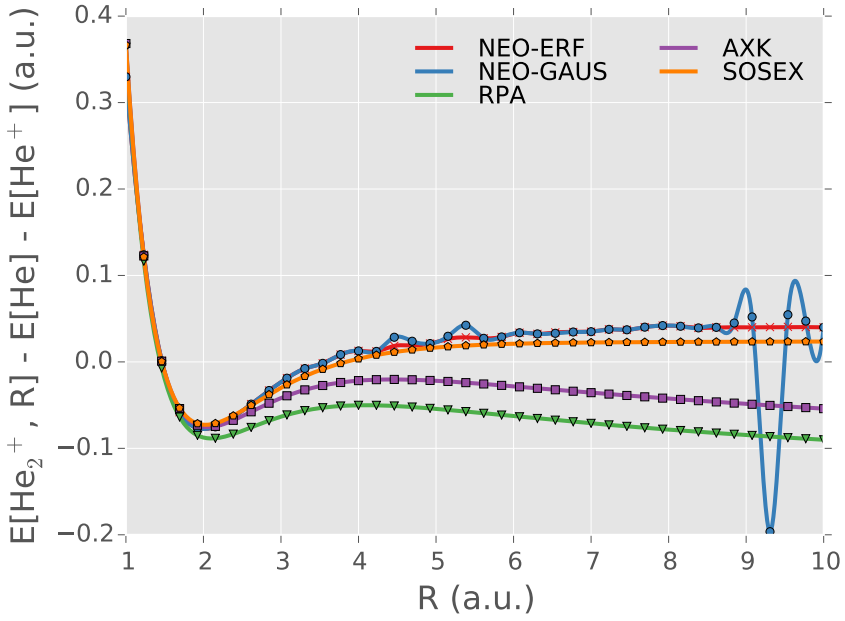

Figure 4.4: Potential energy surface of He_2^+. Calculation performed using def2-TZVP basis sets, gridsize 3.

The instabilities that are present in RPAX, also appear in our approximate NEO exchange kernel. For the case of water, we have negative eigenvalues for most values of the coupling strength, using the Gaussian version of the exchange kernel. Using the Error function kernel,

there are no instabilities. Similarly, using the renormalized picture, there are no instabilities.

α	Eigenvalue
2.544604382862070E-002	-37.8672170278448
2.544604382862070E-002	-18.5209604262274
0.129234407200303	-11.4475502380312
0.129234407200303	-4.07130330888484
0.500000000000000	-67.6156601719156
0.500000000000000	-35.9334957867156
0.702922575688699	-93.4437043339414
0.702922575688699	-51.4497158068690
0.870765592799697	-109.785332040867
0.870765592799697	-61.3849487921057

Table 4.1: Negative eigenvalues of M_α. Calculation was performed using def2-TZVP, gridsize 3, and the Gaussian NEO kernel.

4.6 Conclusions

The random-phase approximation is being considered as one of the strongest prospects for general purpose electronic structure calculations because of its non-perturbative nature, its ability to describe small-gap systems, and its compatibility with full exact exchange, making it free from one-electron self interaction error. It is not, however, without some issues; it is well known that RPA suffers from self-correlation, something that must be fixed by an exchange-correlation kernel f_{xc}. Recent work has seen increasing interest in directly approximating f_{xc} with moderate success.

Here, we constructed a short-ranged but non-local model to the exchange kernel in which physics is baked in via density dependence. Contrary to the present literature, we find that directly approximating f_{xc} using a non-local model may be more difficult than was previously understood. We demonstrate here that explicit inclusion of non-locality in the kernel leads to instabilities. Such instabilities can be mostly removed by taking a renormalized approach

that leads to a perturbative series which we truncate at first order. Instabilities still exist, however, due to the truncation. This leads us to to believe that the route to constructing beyond-RPA corrections should rather not be done by approximating f_{xc} but by continued development of non-local energy functionals where the behavior of the functional can be more controlled and is less erratic.

Chapter 5

Computational design of bioluminescent substrates

This chapter was done in collaboration with the Prescher group UCI. All experimental results are done in part by Dr. Rachel Steinhardt, Colin Rathbun, and Dr. Dave McCutcheon. It was conveniently extended into a pedagogical tool, with multiple high-school and undergraduate students participating.

5.1 Introduction

Recent years have seen a surge of interest in accessing novel luciferin scaffolds for bioluminescence imaging (BLI).[139–143] BLI relies on the enzyme-catalyzed production of light via luciferase enzymes and luciferin small molecules.[144] This reaction has been routinely used in vitro and in vivo for monitoring diverse biological processes.[145] However, a limited supply of robust, light-emitting luciferins pgqhas stymied efforts to visualize multicellular networks and other interactions. Efforts have been focused on developing analogs of D-luciferin, the na-

tive light-emitting substrate for firefly luciferase (Fluc).[139] Fluc catalyzes the activation and subsequent oxidation of D-luciferin, releasing photons of yellow-green light (Figure 5.1).[144] While the mechanism of photon release remains controversial and the subject of intense investigation, the most accepted version involves initial activation of the luciferin substrate (as a luciferyl-AMP anhydride).[144,146–150] Subsequent oxidation of this intermediate, followed by CO_2 release results in a singlet excited-state (S_1) oxyluciferin; this compound then emits light as it relaxes to a singlet ground state (S_0). Fluc can also catalyze light emission with a range of D-luciferin analogs,[145] and a similar mechanism is believed to be operative.

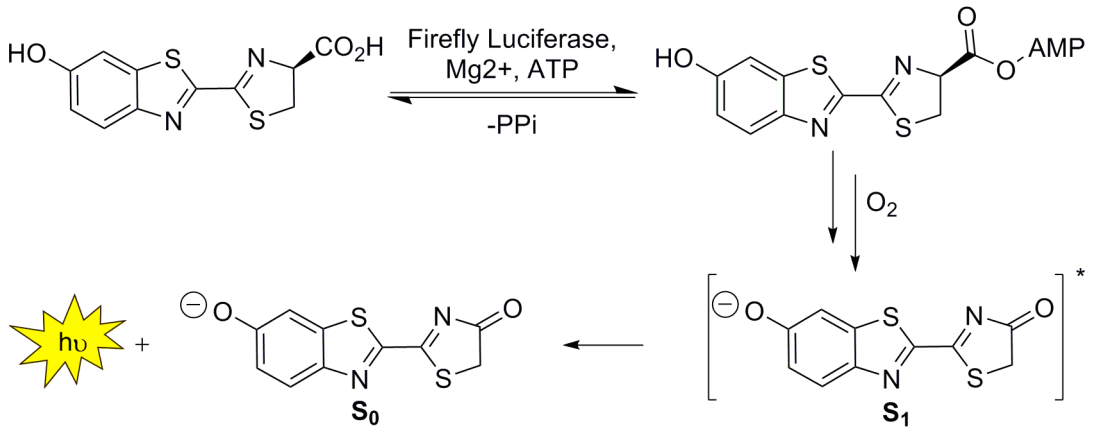

Figure 5.1: Mechanism of luciferase-mediated light production. Fluc catalyzes the adenylation/activation and oxidation of D-luciferin to oxyluciferin, releasing light in the process. The reaction proceeds through an excited state (S_1) oxyluciferin intermediate. Relaxation of this molecule to the ground state (S_0) is accompanied by photon release. Figure provided by the Prescher research group at UCI.

The most robust, light-emitting analogs share common features: strong electron-donating groups at the 6' position, extended π systems, and rigid cores.[143,151,152] However, plenty of analogs exist that meet these criteria, yet remain poor light emitters.[142,151,153] Some notable examples include heterocyclic luciferins (including benzimidazole and benxoxazole variants). Most of these molecules emit less light than D-luciferin when incubated with Fluc.[139,154] Whether the reduced bioluminescent intensities are due to inefficient processing by Fluc, or the inability of the luciferin to access an appropriate electronic excited state (S_1) remains difficult to elucidate. These uncertainties have confounded the development of new useful

luciferin analogs; there is no guarantee that a desired scaffold will be able to reach the appropriate electronic excited state or emit light efficiently from that state. Thus, an important long-term goal involves predicting viable light-emitting scaffolds prior to chemical synthesis. Accurate predictions would avoid time-consuming syntheses, streamlining the production of new bioluminescent tools.

There are several challenges involved in predicting robust luciferin emitters. Bioluminescent light production is a complex, multi-step process that involves chemical activation (versus the light-based excitation of fluorescence), thus, traditional fluorescence parameters do not apply. In this particular case, the light-emitting species is an oxyluciferin, the unstable and difficult to access product of the chemical activation.[155]

Here we present a joint experimental-computational design process for new luciferin analogs. All experimental work including syntheses and (bio)luminescence experiments were performed by the Prescher group at UCI; all computational work was performed by the Furche group at UCI. Time-dependent density functional theory[156] (TDDFT) was used to compute the vertical emission energy and oscillator strength of oxyluciferin from the first singlet excited state (S_1) of the planar geometry to the ground state (S_0). TDDFT has been successfully used to model luciferin absorption and emission spectra previously.[157–162] We demonstrate that the computed oscillator strength of this de-excitation is a qualitative measure for the chemiluminescence intensity. These calculations identified scaffolds that were likely to be robust light emitters, and upon synthesizing compounds of interest, we confirm the predictions using standard biochemical and BLI assays, even in live cells. This leads to a combined theoretical and experimental methodology which may be broadly applicable to bioluminescent probe design and aid in the selection of synthetic luciferin targets with desired optical properties.

5.2 Computational details

Ground-state geometry optimizations were performed using density functional theory (DFT) employing the non-empirical hybrid GGA functional PBE0.[57,98] To account for the diffuse nature of anionic complexes, split-valence basis sets with polarization and diffuse functions (def2-SVPD[163]) were employed. Structures were optimized with convergence criteria of 10^{-7} au, 10^{-8} au, and 10^{-3} au for energy, density, and Cartesian gradients, respectively, using fine numerical quadratures (m3). Ground-state minima were confirmed with analytical frequency analysis revealing no imaginary vibrational modes.[164] Geometry optimizations of the lowest singlet excited state were performed using TDDFT[165] and minima on the excited-state potential energy surfaces were verified by numerical second derivatives. Fluorescence emission intensities and wavelengths were obtained from the lowest excitation from the geometry of the S_1 surface minimum. All calculations were performed with the TURBMOLE quantum chemistry package.[51]

5.2.1 Limitations

We aim to establish a correlation between the intrinsic properties of luciferin chromophores and luminescence intensity. While PBE0 is one of the most accurate density functionals available for excitation energies and structures, it has a tendency to over-stabilize charge-transfer excited states[166]. Effects of the protein and solvent environment on the chromophore are neglected. Solvent effects have been shown to blue shift emission relative to in vacuo calculations,[158,159,161] while the protein environment is postulated to stabilize the phenolate-keto form of oxyluciferin.[167] Further, we only consider radiative emission here. Non-radiative processes such as intersystem crossing, energy transfer, or other quenching mechanisms may lead to considerably lower observed oscillator strengths. The compounds were primarily chosen by chemical intuition and synthetic feasibility, and further improvements may be

possible by systematic searches. The use of oscillator strengths as a measure of the emissive properties of the experimental setup is meant as a straight-forward way to gain a preliminary understanding. In experiments, however, a photon flux is measured. The photon flux is dependent both on the oscillator strength and the emission wavelength. Photon flux can be computed but the results here are put forth simply to establish a connection between the computed emission strength and experimentally observed (bio)chemiluminescence, which is a much more complicated process than what is modeled.

5.3 Results

We first calibrated our computational results by calculating the emission intensity of known luciferin analogs (Table 5.1). The predicted values correlated with the known bioluminescent emission in-tensities in most cases. For example, D-luciferin analogs lacking an electron-donating group at the 6' position were predicted to have low oscillator strengths. Such compounds are known to be poor bioluminescent emitters.[151,168,169] By contrast, D-luciferin analogs with 6'-amino substituents-known robust light emitters were predicted to have oscillator strengths on par with (or in some cases better than) the native Fluc substrate. In the case of 6'-dimethylaminoLuc, the steric bulk of the methyl groups can force an out-of-plane twisting, there-by breaking the conjugation across the molecule and drastically lowering its emission strength.[170–173] Similar decreased light emission have been observed for 6'-alkylated luciferins, including 6'-methoxyLuc, in addition to some fluorophores.[174–176]

Encouraged by these results, we used the same methodology to predict the emission strengths for novel luciferin architectures. These compounds included various electronically and sterically modified luciferins (Table 5.2). This latter category included scaffolds with substituents at the 4', 5', and 7' positions on the D-luciferin core.

Compound		Name	Oscillator Strength[a]	Rel. BLI[b]
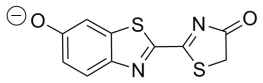		**D–Luc**	100	100
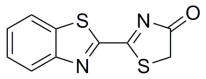		**6'–deoxyLuc**	1.4	<0.01[c]
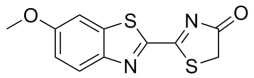		**6'–methoxyLuc**	57.2	<0.01
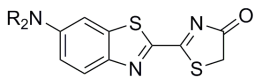	R_1, R_2 = H	**6'–aminoLuc**	91.9	61
	R_1 = Me R_2 = H	**6'–MeNHLH$_2$**	94.9	101
	R_1, R_2 = Me	**6'–Me$_2$NLH$_2$**	102.9	1
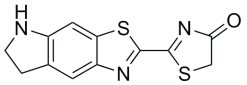	R = H	**CycLuc1**	127.6	38
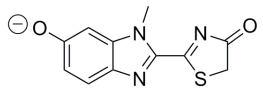		**NMeBenzLuc**	0.3	0.01

Table 5.1: Comparison of calculated oscillator strengths and bioluminescence emission intensities for known luciferins. [a] Calculated as a theoretical maximum. [b] Bioluminescence was measured using 100μM luciferin and 1μg recombinant luciferase. [c] No signal exceeding background was observed.

As expected, the calculated oscillator strengths for the 6'-deoxy compound (6'-deoxyLuc) and nitro-substituted scaffold 4'-NO_2Luc were substantially lower than D-luc. Both 6'-deoxyLuc and 4'-NO_2Luc reduce the amount of electron density at the 6' position of the luciferin ring; this type of modification is known to reduce luciferin light output.[177,178] Since the bioluminescent properties of these analogs are unknown, the reduction in light emission predicted by DFT could imply an inherent reduction in the light-emitting potential of the compound (as noted above). To avoid this confounding issue, we utilized a traditional chemiluminescent assay to measure their intrinsic abilities to produce light (Figure 5.2).[179–181] This non-enzymatic process mimics the enzymatic reaction itself, involving formation of an activated ester intermediate, followed by oxidation.[182] Indeed, White and others have previously shown that the luciferin excited state can be attained by treating activated luciferin esters (as AMP surrogates) with base (e.g., KOPh), in the absence of enzyme.[179] We were able to reproduce these results, observing strong emission from the activated ester of D-luciferin.

Compound	Name	Oscillator Strength[a]	Rel. BLI[b]	Rel. CLI[c]
	D-Luc	100	100	100 ± 11
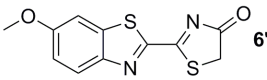	**6'–methoxyLuc**	57.2	<0.01[d]	0.157 ± 0.029
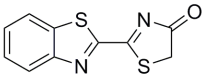	**6'–deoxyLuc**	1.4	<0.01	0.99 ± 0.11
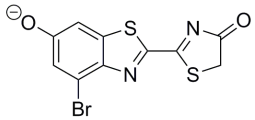	**4'–BrLuc**	86.1	3.1	5.31 ± 0.45
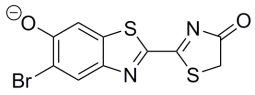	**5'–BrLuc**	104	46.0	15.1 ± 2.4
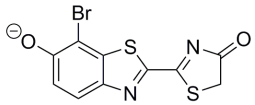	**7'–BrLuc**	79.3	3.4	15.8 ± 2.0
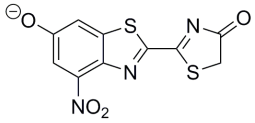	**4'–NO_2Luc**	25.8	0.5	0.06–0.47[e]
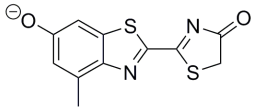	**4'–MeLuc**	93.3	23.1	46.5 ± 10.4

Table 5.2: Calculated oscillator strengths and measured bioluminescent photon production for novel luciferin analogs. [a] Calculated as a theoretical maximum. [b] Bioluminescence was measured using 100μM luciferin and 1μg recombinant luciferase. [c] Chemiluminescence was measured at approximately 25μM luciferin and 0.05M KOPh in DMSO. [d] No signal exceeding background was observed. [e] A range of measured values is given due to compound instability.

Control compounds (e.g., 6'-methoxyLuc and 6'-deoxyLuc) with weaker electron donation into the aromatic ring (a key feature of luciferins) did not produce this level of emission.

More interesting patterns emerged with the sterically modified compounds. DFT analyses were performed on a series of luciferins comprising modifications at the 4', 5', and 7' positions. In initial surveys, the site of substitution was predicted to minimally impact emission for a given substituent. However, the electron-withdrawing/donating character of the substituent itself was predicted to greatly impact the strength of the emission (i.e., the more electron-withdrawing substituents correlated with the weakest oscillator strengths), leading us to

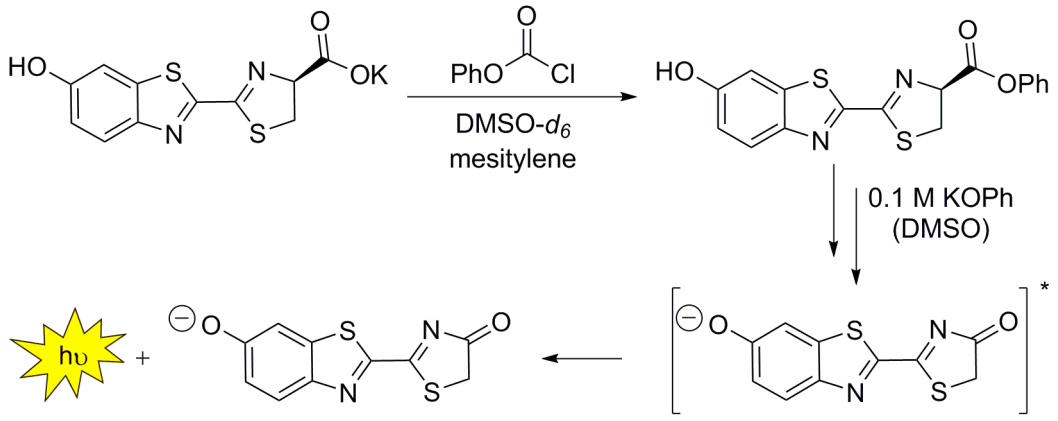

Figure 5.2: Chemiluminescent light production from luciferin analogs. Luciferin acids can be chemically activated to labile esters. Subsequent H-atom abstraction/oxidation generates light-emitting species. This procedure mimics the bioluminescent reaction mediated by Fluc. Figure provided by the Prescher research group at UCI.

move forward with the bromo-substituted compounds (4'-BrLuc, 5'-BrLuc, and 7'-BrLuc). Bromo substituents are inductive electron-withdrawing groups, yet ortho/para-directors in classic organic transformations. Thus, they fall in the "middle-of-the-road" considering their electronic impact. Methyl groups are classified solely as inductive donors, while nitro groups are classified as resonance acceptors. Bromo substituents are also sufficiently large to present a steric barrier for enzyme utilization and thus help us deconvolute the role of electronics vs. enzymatic processing. Last, these substituents offer unique opportunities for further analog development – as chemical handles for important classes of cross-coupling reactions.

When the bromo luciferins were subjected to the chemiluminescence assay pictured in Figure 5.2, light emission was observed for all compounds. The intensity of photon production was lower than that of D-luciferin, which was predicted by the DFT calculations (Figure 5.3). Within the analog series, the 5'-BrLuc and 7'-BrLuc compounds exhibited nearly the same levels of chemiluminescence. The photon emission values for the 4'-substituted luciferin (4'-BrLuc) were somewhat lower, but on par with the other two isomers (5', and 7'). The reduction in chemiluminescence relative to D-Luc can be attributed to electronic effects due to the presence of bromine. DFT calculations revealed two low-lying states that may

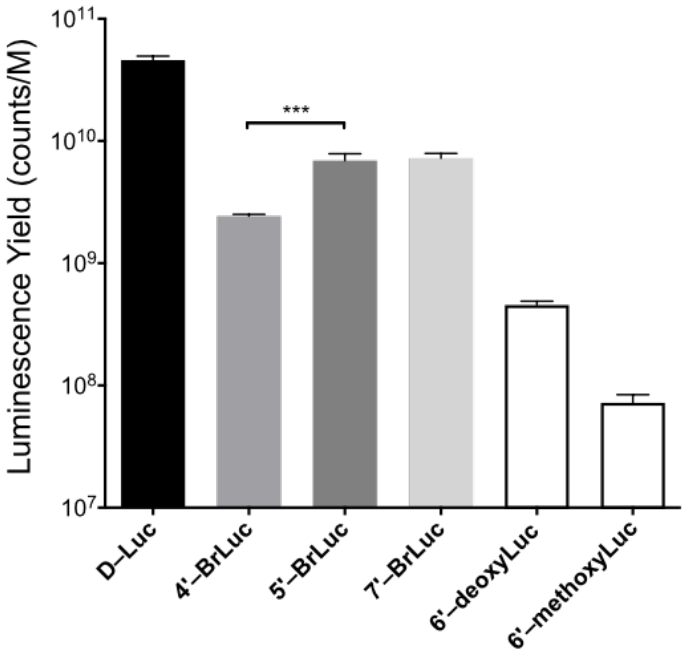

Figure 5.3: Bromo-substituted luciferins are capable of chemi-luminescent photon production. Measured counts were normalized to concentration. Error bars represent the standard error in the mean of at least 18 measurements over three days ***$p < 0.001$ (t-test). Figure provided by the Prescher research group at UCI.

play a major role in the deactivation of luciferin emission: (1) a triplet excited state and (2) a singlet twisted intramolecular charge-transfer (TICT) excited state. It is well known that in the case of (1) intersystem crossing leads to non-radiative relaxation and (2) that TICT states display near-zero oscillator strength ("dark") due to the broken conjugation of the π-system.[170] Luciferins with groups that can twist out of plane may have a lower-lying energetically twisted excited state responsible for the observed 'dark' behavior. In some cases, the TICT state was lower in energy than the planar S_1 state. In chemiluminescence experiments, one would expect the emission profile to derive from a Boltzmann-like distribution of torsional angles, only some of which are light-emitting, while the computational results represent a single excitation from a discrete nuclear configuration (either planar or twisted). TICT states may be underappreciated in luciferin emission and have important ramifications for orthogonal probe development. From a chemiluminscence perspective, both the experimental and computational data suggest that an increase in emission intensity can

be achieved by chemical modification at many positions on the luciferin core, as long as the electronic requisites are met by the appendage. However, if this extra steric bulk yields poor bioluminescence, the reduction in light emission must be attributed to poor enzyme utilization rather than an inherent inability to reach the necessary excited state.

When the three bromo analogs were analyzed with recombinant Fluc, a significant reduction in bioluminescent light emission was observed for both 7'-BrLuc and 4'-BrLuc. 5'-BrLuc retained robust light emission (Figure 5.4). This suggests that the 5'-BrLuc analog is more efficiently processed by Fluc than the 4' or 7' isomers (since chemiluminescent data suggest that the compounds are roughly capable of producing the same numbers of photons). Other luciferin analogs with rather bulky groups at the 5' position are also known to be processed efficiently by Fluc.[183] Indeed, recent crystal structure analyses of Fluc suggest that its active site has sufficient room to accommodate steric appendages at the 5' and 6' positions, but tends to be too crowded to fit large modifications at the 4' and 7' positions.

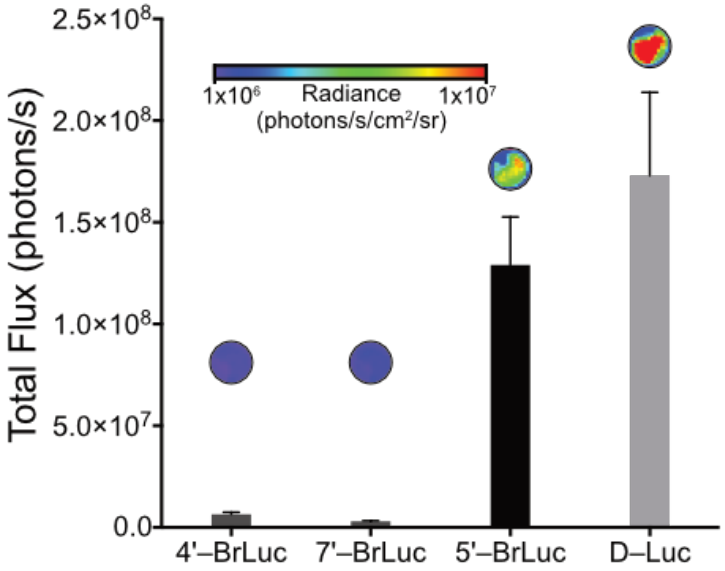

Figure 5.4: Differential bioluminescent photon production is similarly observed with Fluc-expressing cells treated with series of bromo luciferins. Compounds were administered to HEK293 sells stably expressing Fluc with a concentration of 100,000 cells per well. Imaging was performed at 37 degC. Compounds were diluted to the indicated concentration in PBS pH 7.4. For further details see supporting information. Sample images are included. Peak emission for all analogs at 100 μM. Figure provided by the Prescher research group at UCI.

Collectively, DFT calculations and in vitro assays suggest that the 5'-brominated analog would be suitable for BLI, while the 4' and 7' isomers are good starting points for orthogonal probe development. These compounds were further analyzed in cells. When the brominated compounds were incubated with Fluc-expressing HEK293 cells, robust light emission was observed from cultures treated with 5'-BrLuc. Minimal light was produced with 4'-BrLuc and 7'-BrLuc, consistent with the in vitro data. Interestingly, the light emission observed with 5'-BrLuc was similar to D-Luc. These data suggest that 5'-BrLuc may have superior cell permeability compared to the native probe. Though it performed worse than D-Luc in vitro, it performs better in cellulo at lower concentrations, implying superior cell permeability.

5.4 Conclusions

Limitations in multi-spectral and multi-component emission have spurred the development of luciferins with altered emission wavelengths, conjugation, caged probe development, and orthogonal pairs. The efficient development of such probes has been confounded by a lack of accurate models to predict robust light-emitting luciferins. Here, we report a link between density functional calculations and experimental results that allows for the a priori assessment of the light-emitting efficacy of new luciferin analogs with moderate relia-bility. Our calculations predict that a variety of sterically and electronically modified luciferins should be good bioluminescent emitters. However, the existence of other nearby excited states, the lack of a simulated protein environment, and the general difficulty of describing charge-transfer excitations using TDDFT, means that a predictive model based simply on the adiabatic emission from the S_1 state is not as reliable as one would hope. Enzymatic assays confirmed that the molecules retained their ability to bind the enzyme, but were poorly turned over by luciferase itself. It has also not escaped our attention that these groups can be further sterically modified using traditional cross-coupling reactions. These experiments

are ongoing in our laboratory and will be reported in due course. Future theoretical work could address environment effects, non-radiative quenching of luminescence, and systematic strategies to search chemical space for the best emitters. Our results establish a crucial precedence that luciferin scaffolds may be poor substrates for the native enzyme, but still capable of emission from a chemically-accessed excited state. These studies thus provide a rational basis for the design of synthetic luciferins and other bioluminescent reporters.

Chapter 6

Understanding the nature of new oxidation states of lanthanides

This chapter provides an introduction to work done in collaboration with the Evans group at UCI. The work was published in the Journal of the American Chemical Society in early 2015. Reprinted with the permission of, M.E. Fieser, M.R. MacDonald, B.T. Krull, J.E. Bates, J.W. Ziller, F. Furche, and W.J. Evans, "Structural, Spectroscopic, and Theoretical Comparison of Traditional vs Recently Discovered Ln^{2+} Ions in the [K(2.2.2-cryptand)][$(C_5H_4SiMe_3)_3Ln$] Complexes: The Variable Nature of Dy^{2+} and Nd^{2+}," *Journal of the American Chemical Society* **137**(1), 369 (2015).

For nearly a century, lanthanides, also known as the rare earth elements, were considered to be generally unreactive in redox reactions due to the stability of the +3 oxidation state[184] and the limited spatial extent of their valence $4f$ electrons.[185] While the reactivity of trivalent is strongly governed by their $4f$-orbital manifold, recently discovered +2 oxidation states for all of the lanthanides has shown that the $5d$-orbitals under an appropriate ligand field, can lie close in energy to the $4f$ orbitals, and be involved in interesting chemical processes.[186–188]

The chemistry of lanthanides is of increasing interest due to their unique electronic structure and large abundance relative to widely used precious metals such as platinum or irridium. Divalent lanthanides are strong reducing agents[189–191] and are used in bioengineered systems where an extremely strong reductant is necessary.[192] A bimetallic complex of yttrium, a lanthanide not expected to exist as a +2 ion, was shown to be able to reduce $(N_2)^{2-}$ by an additional electron originating from the $5d$ manifold of the metal complex, demonstrating the extremely potent reductive nature.[193] The significance of this reactivity is that yttrium was able to exhibit catalytic behavior like that of a transition metal and has many implications for industrial applications.

This work, done in collaboration with the Evans group at UCI, highlights the electronic structure of traditional divalent lanthanides (Eu, Yb, Sm, Tm, Nb, and Dy) that are isostructural to the lanthanides (Tb, Pr, Gd, Lu, Ho, Er, Y) that have recently been shown to exist in the +2 oxidation state, which goes against previously considered paradigms. New complexes of Eu, Yb, Sm, Tm, Nd, and Dy using the Cp' (Cp' = $C_5H_4SiMe_3$) and Cp" (Cp" = $C_5H_3(SiMe_3)_2$-1,3) ligand platforms were synthesized to make a direct study of the metal effect on the electronic structure of divalent lanthanides. Density functional theory (DFT) was used to study the ground-state of all complexes and the predicted structural properties described the bond-lengthening upon reduction with a high level of confidence. Time-dependent DFT was used to simulate the UV-vis spectra and qualitative agreement with experiment shows that Laporte allowed $4f \rightarrow 5d$ transitions dominate the spectra when

the lanthanides are in the +2 oxidation state. Both by experiment and computation, divalent complexes of Eu, Yb, Tm, and Sm have distinctly $4f^{n+1}$ ground-states, as expected. However, Nd and Dy, have more complicated electronic structure and can have their ground-state configuration easily modulated between $4f^{n+1}$ or $4f^n5d^1$ based on their surrounding ligand field. Neodymium is a special case where the orbital that is occupied upon one-electron reduction is a mixed $4f - 5d$ orbital (Figure 6.1). These findings shed light on the interesting and unexpected electronic structure of lanthanides and provide a way to tailor their electronics for many new applications.

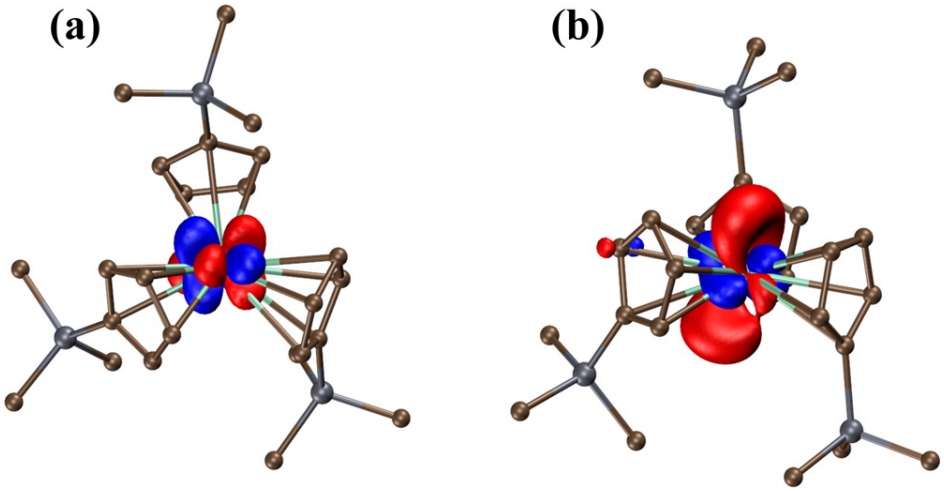

Figure 6.1: Molecular orbital plots of (a) the LUMO of Cp'$_3$Nd and (b) the HOMO of the one-electron reduced [Cp'$_3$Nd]$^-$. Plots reflect an isosurface value of 0.05.

JACS
JOURNAL OF THE AMERICAN CHEMICAL SOCIETY
Article
pubs.acs.org/JACS

Structural, Spectroscopic, and Theoretical Comparison of Traditional vs Recently Discovered Ln^{2+} Ions in the [K(2.2.2-cryptand)][$(C_5H_4SiMe_3)_3Ln$] Complexes: The Variable Nature of Dy^{2+} and Nd^{2+}

Megan E. Fieser, Matthew R. MacDonald, Brandon T. Krull, Jefferson E. Bates, Joseph W. Ziller, Filipp Furche,* and William J. Evans*

Department of Chemistry, University of California, Irvine, California 92697-2025, United States

Supporting Information

ABSTRACT: The Ln^{3+} and Ln^{2+} complexes, Cp'_3Ln, **1**, (Cp' = $C_5H_4SiMe_3$) and [K(2.2.2-cryptand)][Cp'_3Ln], **2**, respectively, have been synthesized for the six lanthanides traditionally known in +2 oxidation states, i.e., Ln = Eu, Yb, Sm, Tm, Dy, and Nd, to allow direct structural and spectroscopic comparison with the recently discovered Ln^{2+} ions of Ln = Pr, Gd, Tb, Ho, Y, Er, and Lu in **2**. **2-La** and **2-Ce** were also prepared to allow the first comparison of all the lanthanides in the same coordination environment in both +2 and +3 oxidation states. **2-La** and **2-Ce** show the same unusual structural feature of the recently discovered +2 complexes, that the Ln−(Cp′ ring centroid) distances are only about 0.03 Å longer than in the +3 analogs, **1**. The Eu, Yb, Sm, Tm, Dy, and Nd complexes were expected to show much larger differences, but this was observed for *only four of these traditional six* lanthanides. **2-Dy** and **2-Nd** are like the new nine ions in this tris(cyclopentadienyl) coordination geometry. A DFT-based model explains the results and shows that a $4f^n5d^1$ electron configuration is appropriate not only for the nine recently discovered Ln^{2+} ions in **2** but also for Dy^{2+} and Nd^{2+}, which traditionally have $4f^{n+1}$ electron configurations like Eu^{2+}, Yb^{2+}, Sm^{2+}, and Tm^{2+}. These results indicate that the ground state of a lanthanide ion in a molecule can be changed by the ligand set, a previously unknown option with these metals due to the limited radial extension of the 4f orbitals.

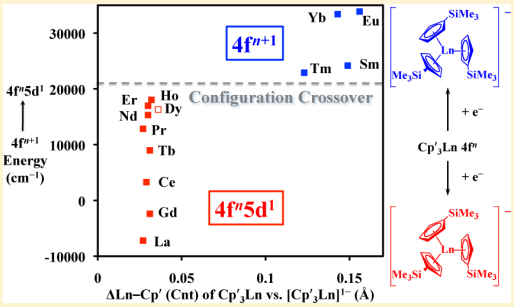

INTRODUCTION

For over 50 years, it was thought that only six lanthanide elements would form +2 ions. Eu^{2+}, Yb^{2+}, and Sm^{2+} were known since the 1920s in solution and in the solid state.[1−4] Tm^{2+}, Dy^{2+}, and Nd^{2+} were known only in the solid state[5−7] until 1997−2001 when the first solution examples were found.[8−14] The existence of just six Ln^{2+} ions was well justified on the basis of extensive solid state data and calculated redox potentials.[6,15−19] Solid state compounds formed under thermodynamic control at high temperature that contained +2 ions by stoichiometry, e.g., LnX_2,, were found to be $Ln^{2+}(X^{1-})_2$ salts only with Ln = Eu, Yb, Sm, Tm, Dy, and Nd. For the other lanthanides, the solids were best described as $Ln^{3+}(X^{1-})_2(e^{1-})$ materials with a delocalized electron in a conduction band;[16,20] i.e., Ln^{2+} did not form under these conditions. A "configuration crossover" was described for the difference between the six "pseudo-alkaline-earth lanthanides," i.e., Eu, Yb, Sm, Tm, Dy, and Nd, and the other lanthanides.[21]

A similar dichotomy was observed in solution based on calculated generic reduction potentials for conversion of a $4f^n$ Ln^{3+} ion to a $4f^{n+1}$ Ln^{2+} ion, Table 1. The calculated reduction potentials for the lanthanides beyond the traditional six Ln^{2+} ions known in the solid state were so negative, namely, −2.7 to −3.9 V vs NHE[17] (−3.1 to −4.3 V vs Fc/Fc^+),[23] that these ions would be expected to decompose all common solvents. Indeed, the high reactivity of even Dy^{2+} and Nd^{2+} with solvents suggested that the more reducing ions would be unstable in solution.[8−10,13,14,24−29]

Table 1. Calculated Ln^{3+}/Ln^{2+} Reduction Potentials of Yttrium and the Lanthanides[17,22]

Ln	potential (V vs NHE)	Ln	potential (V vs NHE)
Eu	−0.35	Y	−2.8
Yb	−1.15	Pr	−2.9
Sm	−1.55	Ho	−2.9
Tm	−2.3	Er	−3.1
Dy	−2.5	La	−3.1
Nd	−2.6	Ce	−3.2
Pm	−2.7	Tb	−3.7
Lu	−2.7	Gd	−3.9

However, it recently has been shown that Ln^{2+} ions are accessible for all of the lanthanides except Pm, which was not

Received: October 21, 2014
Published: December 26, 2014

DOI: 10.1021/ja510831n
J. Am. Chem. Soc. 2015, 137, 369−382

Scheme 1. Crystallographically Characterized Products of Reduction of Cp''_3Ln (Ln = La and Ce; $Cp'' = C_5H_3(SiMe_3)_2$-1,3) by Lappert et al.[30]

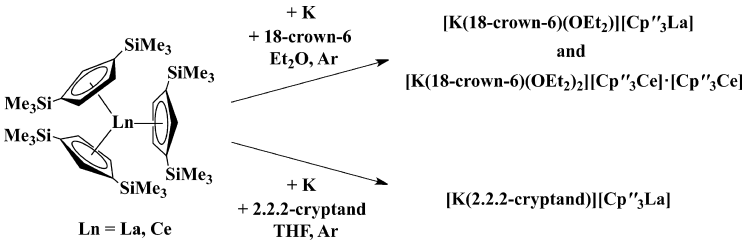

Scheme 2. Crystallographically Characterized Products of Reduction of Cp'_3Ln (Ln = Y, Pr, Gd, Tb, Ho, Er, Lu; $Cp' = C_5H_4SiMe_3$)[31−33]

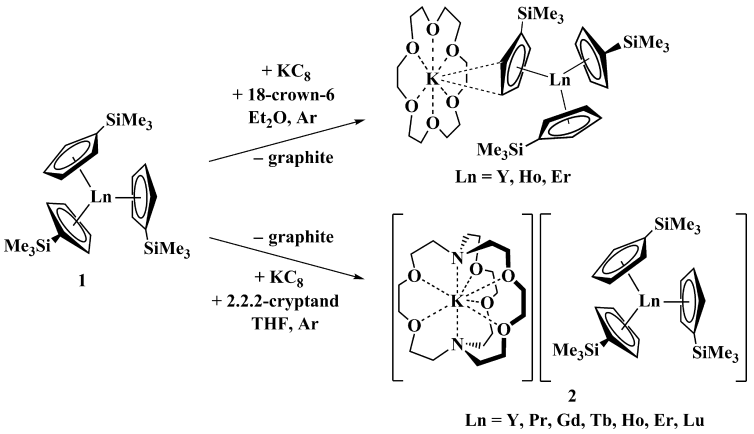

investigated because of its radioactivity. Complexes of nine new +2 ions, La^{2+}, Ce^{2+}, Pr^{2+}, Gd^{2+}, Tb^{2+}, Ho^{2+}, Er^{2+}, Y^{2+}, and Lu^{2+}, were synthesized via Schemes 1 and 2.[30−33] These new complexes had major structural differences compared to complexes of the traditional six +2 ions in that the difference in bond distances between a +2 ion complex and its +3 ion analog was small. Hence, all of the Ln^{2+} complexes in Schemes 1 and 2 have Ln−(cyclopentadienyl ring centroid) distances that are only 0.020−0.032 Å (~1%) longer than their Ln^{3+} analogs. This contrasted so sharply with the 0.10−0.20 Å (~6%) differences generally seen for complexes of Eu^{2+}, Yb^{2+}, Sm^{2+}, Tm^{2+}, Dy^{2+}, and Nd^{2+} compared to their Ln^{3+} counterparts[9,10,18,34−37] that there was initial skepticism that the new complexes contained +2 ions.

The large differences in bond distances between Ln^{2+} complexes of the traditional six Ln^{2+} lanthanides and their Ln^{3+} analogs are expected, since there are large differences between the radii of $4f^n$ Ln^{3+} and $4f^{n+1}$ Ln^{2+} ions and there is little metal−ligand interaction due to the contracted nature of the 4f orbitals. A typical example is that the average Sm−(C_5Me_5 centroid) and Sm−O distances in the Sm^{2+} complex $(C_5Me_5)_2Sm(THF)_2$ (2.599 and 2.633 Å, respectively)[38] are 0.176 and 0.173 Å longer than those in the compositionally similar Sm^{3+} compound $[(C_5Me_5)_2Sm(THF)_2][BPh_4]$ (2.423 and 2.457 Å).[39] Another example pertinent to this study is the 2.486 Å average Sm−(Cp″ centroid) distance in the Sm^{3+} complex, Cp''_3Sm,[40] vs the 2.676 Å analog in [K(18-crown-6)$(toluene)_2$][Cp''_3Sm].[35]

The small differences in bond distances in the +2 vs +3 complexes in Schemes 1 and 2 were similar to the small changes with changing oxidation state observed in transition metal complexes.[41] In transition metal complexes, the bonding is not simply a sum of ionic radii because there are covalent interactions between the metal d orbitals and the ligands. Since spectroscopic and theoretical analyses indicated that the Ln^{2+} ions in Schemes 1 and 2 had $4f^n5d^1$ and not $4f^{n+1}$ electron configurations ($4d^1$ for Y^{2+}), the small increases in bond distances could be explained by the d character in the configurations of the +2 ions. The accessibility of d^1 configurations for these ions was consistent with the crystal field splitting in the tris(cyclopentadienyl) ligand environment of these compounds.[42−47] In this trigonal field, the d_{z^2} orbital is lowest in energy. Apparently, its energy is low enough with respect to the 4f orbitals that the d_{z^2} orbital can be populated in the reduction reactions of Schemes 1 and 2.

Although a correlation existed between $4f^n5d^1$ electron configuration and Ln^{3+}/Ln^{2+} size differences for the +2 ions in Schemes 1 and 2 vs the traditional six +2 ions with $4f^{n+1}$ configurations, the size comparisons were not made on the same set of complexes. Accordingly, it was of interest to make the [K(2.2.2-cryptand)][Cp'_3Ln] complexes, **2**, of the traditional six +2 ions, Eu^{2+}, Yb^{2+}, Sm^{2+}, Tm^{2+}, Dy^{2+}, and Nd^{2+}, for direct comparison with those in Scheme 2. To include comparisons with the Ln^{2+} ions found by Lappert, Scheme 1, using one uniform ligand set, the Ln = La and Ce versions of **2** were also synthesized. To make the Ln^{3+}/Ln^{2+} bond distance comparisons, the Cp'_3Ln complexes, **1**, of Eu, Yb, Sm, Tm, and Dy also had to be synthesized and structurally characterized.

These syntheses and crystallographic analyses allow the first comparison of all the lanthanides in the same coordination environment in both +2 and +3 oxidation states. The results are described here along with a comparison of UV−vis spectra of

DOI: 10.1021/ja510831n
J. Am. Chem. Soc. 2015, 137, 369−382

the analogous complexes of the traditional six Ln^{2+} ions vs all the other Ln^{2+} ions in the series. The density functional theory (DFT) analysis of the structural and spectroscopic data have proven very valuable in understanding the results and are also reported.

EXPERIMENTAL SECTION

The syntheses and manipulations described below were conducted under argon with rigorous exclusion of air and water using glovebox, vacuum line, and Schlenk techniques. Solvents were sparged with UHP grade argon (Airgas) and passed through columns containing Q-5 and molecular sieves before use. NMR solvents (Cambridge Isotope Laboratories) were dried over NaK/benzophenone, degassed by three freeze−pump−thaw cycles, and vacuum-transferred before use. Anhydrous $LnCl_3$ (Ln = La, Ce, Nd, Sm, Dy, Yb),[48] $LnI_2(THF)_2$ (Ln = Eu, Yb),[49,50] $TmI_3(THF)_{3.5}$,[51] KC_8,[52] $AgBPh_4$,[53] KCp'[54] and Cp'_3Ln, **1-Ln** (Ln = La,[54] Ce,[55,56] Nd[57]), were prepared according to literature. 2.2.2-Cryptand, 4,7,13,16,21,24-hexaoxa-1,10-diazabicyclo[8.8.8]hexacosane (Acros Organics), was placed under vacuum (10^{-3} Torr) for 12 h before use. ^{1}H NMR (500 MHz) and ^{13}C NMR (125 MHz) spectra were obtained on a Bruker GN500 or CRYO500 MHz spectrometer at 298 K. For some paramagnetic compounds, ^{1}H NMR spectra could only be observed when a capillary tube containing pure deuterated solvent was placed in the paramagnetic solution to assist in properly locking and shimming the instrument. IR samples were prepared as KBr pellets, and the spectra were obtained on a Varian 1000 FT-IR spectrometer. Elemental analyses were performed on a PerkinElmer 2400 series II CHNS elemental analyzer. EPR spectra were collected using X-band frequency (9.3−9.8 GHz) on a Bruker EMX spectrometer equipped with an ER041XG microwave bridge, and the magnetic field was calibrated with DPPH (g = 2.0036). UV−vis spectra were obtained in THF at 298 K using a Varian Cary 50 Scan UV−vis spectrophotometer.

[K(2.2.2-cryptand)][Cp′$_3$La], 2-La. In an argon-filled glovebox, Cp'_3La, **1-La** (208 mg, 0.378 mmol), and 2.2.2-cryptand (142 mg, 0.377 mmol) were combined and dissolved in THF (2 mL). KC_8 (75 mg, 0.55 mmol) was quickly added to the stirred colorless solution. The reaction mixture immediately turned black/violet, and after 1 min of stirring, Et_2O (3 mL) was added and the mixture was filtered to remove a black precipitate, presumably graphite. The dark purple filtrate was cooled to −35 °C in the freezer for 1 h. The solution was layered with additional Et_2O (15 mL) and stored at −35 °C for 24 h to produce a black/purple crystalline solid. The mother liquor was decanted and the solids were rinsed with Et_2O (2 mL) and briefly dried under vacuum to yield **2-La** as a black/purple crystalline solid that analyzed as the solvate [K(2.2.2-cryptand)][Cp'_3La]·THF (230 mg, 59%). Black/purple single crystals of **2-La·THF**, suitable for X-ray diffraction, were grown from THF/Et_2O at −35 °C. IR: 3069m, 2946s, 2887s, 2820m, 1925w, 1577w, 1480m, 1447m, 1433m, 1405w, 1354s, 1301m, 1260m, 1237s, 1172s, 1135s, 1105s, 1082s, 1034s, 949s, 932m, 901s, 832s, 745s, 729m, 688w, 673m, 626m cm^{-1}. Anal. Calcd for $C_{42}H_{75}N_2O_6Si_3KLa{\cdot}C_4H_8O$: C, 53.21; H, 8.06; N, 2.70. Found: C, 52.83; H, 8.44; N, 2.74. UV−vis (THF) λ_{max}, nm (ε, M^{-1} cm^{-1}): 310 (4400), 433 (3900 shoulder), 502 (5600 shoulder), 554 (6500), 692 (2600 shoulder).

[K(2.2.2-cryptand][Cp′$_3$Ce], 2-Ce. As described for **2-La**, bright blue solids of **1-Ce** (189 mg, 0.342 mmol) and 2.2.2-cryptand (129 mg, 0.343 mmol) were dissolved in THF (2 mL) to form an amber solution, which was combined with KC_8 (65 mg, 0.48 mmol) to produce **2-Ce** as a black/purple crystalline solid that analyzed as the solvate [K(2.2.2-cryptand)][Cp'_3Ce]·THF (188 mg, 53%). Black/purple single crystals of **2-Ce·THF**, suitable for X-ray diffraction, were grown from THF/Et_2O at −35 °C. IR: 3070w, 2946s, 2888s, 2821m, 2486w, 1585w, 1480m, 1447m, 1434m, 1405w, 1355s, 1301m, 1260m, 1237s, 1172s, 1135s, 1107s, 1081s, 1035s, 950m, 932m, 901s, 832s, 746s, 730m, 673w, 626m cm^{-1}. Anal. Calcd for $C_{42}H_{75}N_2O_6Si_3KCe{\cdot}C_4H_8O$: C, 53.14; H, 8.05; N, 2.69. Found: C, 52.94; H, 8.37; N, 2.73. UV−vis (THF) λ_{max}, nm (ε, M^{-1} cm^{-1}): 385 (3800), 462 (4000 shoulder), 538 (4500), 635 (4700).

[K(2.2.2-cryptand)][Cp′$_3$Nd], 2-Nd. As described for **2-La**, dull green solids of **1-Nd** (206 mg, 0.370 mmol) and 2.2.2-cryptand (140 mg, 0.372 mmol) were dissolved in THF (2 mL) to form a light aquamarine-purple solution, which was combined with KC_8 (71 mg, 0.52 mmol) to produce **2-Nd** as a black/maroon-purple crystalline solid that analyzed as the solvate [K(2.2.2-cryptand)][Cp'_3Nd]·THF (106 mg, 27%). Black/maroon-purple single crystals of **2-Nd·THF**, suitable for X-ray diffraction, were grown from THF/Et_2O at −35 °C. IR: 3072m, 2946s, 2888s, 2824m, 2362w, 1925s, 1589w, 1480m, 1447m, 1435m, 1354s, 1301m, 1260m, 1236s, 1174s, 1135s, 1107s, 1082s, 1036s, 950s, 932m, 902s, 832s, 747s, 674w, 631m cm^{-1}. Anal. Calcd for $C_{42}H_{75}N_2O_6Si_3KNd{\cdot}C_4H_8O$: C, 52.93; H, 8.02; N, 2.68. Found: C, 52.58; H, 8.31; N, 2.71. UV−vis (THF) λ_{max}, nm (ε, M^{-1} cm^{-1}): 420 (4700), 483 (4200 shoulder), 654 (2000 shoulder).

Cp′$_3$Sm, 1-Sm. In an argon-filled glovebox, a sealable 100 mL side arm Schlenk flask equipped with a greaseless stopcock was charged with $SmCl_3$ (286 mg, 1.11 mmol), a magnetic stir bar, and Et_2O (20 mL). A solution of KCp′ (600 mg, 3.40 mmol) in Et_2O (20 mL) was added to the stirred slurry, and the mixture was stirred at room temperature for 12 h. The solvent was removed under vacuum from the resulting yellow mixture. Hexane (40 mL) was added to the reaction flask. The flask was attached to a Schlenk line, and the mixture was heated to reflux for 6 h. The solvent was removed under vacuum, and the flask was brought into a glovebox free of coordinating solvents. Additional hexane (30 mL) was added, and the resulting light orange suspension was filtered to remove white solids, presumably KCl and excess KCp′. The solvent was removed from the filtrate under vacuum. The resulting bright orange solids were extracted with pentane (10 mL), and removal of solvent under vacuum afforded **1-Sm** as a microcrystalline bright orange solid (525 mg, 84%). Bright orange single crystals of **1-Sm**, suitable for X-ray diffraction, were grown from pentane at −35 °C. ^{1}H NMR (C_6D_6): δ 22.28 (s, $C_5H_4SiMe_3$, 6H), 13.15 (s, $C_5H_4SiMe_3$, 6H), −3.69 (s, $C_5H_4SiMe_3$, 27H). IR: 3064w, 2953m, 2895m, 2714w, 2361w, 1872w, 1847w, 1745w, 1577w, 1442m, 1411w, 1364m, 1312w, 1243s, 1196w, 1178s, 1061w, 1042s, 998w, 903s, 832s, 773s, 750s, 685m, 631m cm^{-1}. Anal. Calcd for $C_{24}H_{39}Si_3Sm$: C, 51.27; H, 6.99. Found: C, 51.02; H, 6.67.

[K(2.2.2-cryptand)][Cp′$_3$Sm], 2-Sm. As described for **2-La**, a light orange solution of **1-Sm** (191 mg, 0.340 mmol) and 2.2.2-cryptand (128 mg, 0.340 mmol) in THF (2 mL) was combined with KC_8 (50 mg, 0.37 mmol) to produce **2-Sm** as a dark purple crystalline solid that analyzed as the solvate [K(2.2.2-cryptand)][Cp'_3Sm]·THF (171 mg, 48%). Dark purple single crystals of **2-Sm·THF**, suitable for X-ray diffraction, were grown from THF/Et_2O at −35 °C. IR: 3337w, 3270w, 3068m, 2948s, 2891s, 2824s, 2349w, 2086w, 1570s, 1480m, 1438s, 1354s, 1302m, 1260s, 1240s, 1183s, 1135s, 1107s, 1082s, 1035s, 950s, 932m, 904s, 832s, 737s, 677m, 628m cm^{-1}. Anal. Calcd for $C_{42}H_{75}N_2O_6Si_3KSm{\cdot}C_4H_8O$: C, 52.62; H, 7.97; N, 2.67. Found: C, 52.49; H, 8.34; N, 2.64. UV−vis (THF) λ_{max}, nm (ε, M^{-1} cm^{-1}): 360 (700), 402 (500), 509 (600), 566 (400 shoulder), 680 (200).

Cp′$_2$Eu(THF)$_2$, 3-Eu. In an argon-filled glovebox, a solution of KCp′ (368 mg, 2.09 mmol) in THF (6 mL) was added to a stirred pale yellow-green slurry of $EuI_2(THF)_2$ (560 mg, 1.02 mmol). The mixture immediately turned bright orange. After 2 h of stirring, the mixture was centrifuged to remove white solids, presumably KI, and the bright red-orange supernatant was stirred while hexane (5 mL) was added slowly. The white solids that precipitated were removed via filtration, and the filtrate was concentrated to 1 mL under reduced pressure. The thick oil was layered with Et_2O (15 mL) and stored at −35 °C for 2 d, which produced red-orange crystals that were suitable for X-ray diffraction. The mother liquor was decanted and the crystals were dried under vacuum to yield **3-Eu** as a bright red-orange solid (404 mg, 69%). IR: 3083w, 3058w, 2951m, 2888m, 2699w, 2361w, 1868w, 1558w, 1440m, 1398w, 1354m, 1306w, 1244s, 1182m, 1106w, 1038s, 904s, 834s, 793m, 776s, 762s, 749s, 685w, 641m, 629m cm^{-1}. Anal. Calcd for $C_{16}H_{26}Si_2Eu$: C, 45.06; H, 6.14. Found: C, 44.93; H, 6.09.

DOI: 10.1021/ja510831n
J. Am. Chem. Soc. 2015, 137, 369−382

[K(2.2.2-cryptand)][Cp′$_3$Eu], 2-Eu. In an argon-filled glovebox, a solution of KCp′ (31 mg, 0.18 mmol) and 2.2.2-cryptand (66 mg, 0.18 mmol) in THF (1 mL) was added to a stirred solution of Cp′$_2$Eu(THF)$_2$, **3-Eu** (100 mg, 0.175 mmol), in THF (1 mL). An immediate color change from bright red-orange to dark magenta-purple resulted. After 5 min of stirring, the solution was concentrated to ∼0.5 mL under reduced pressure, layered with Et_2O (6 mL), and stored at −35 °C for 2 d to produce dark purple crystals, suitable for X-ray diffraction. The mother liquor was decanted and the crystals were briefly dried under vacuum to yield **2-Eu** as a dark purple crystalline solid that analyzed as the solvate [K(2.2.2-cryptand)]-[Cp′$_3$Eu]·THF (150 mg, 82%). Dark purple single crystals of **2-Eu·THF**, suitable for X-ray diffraction, were grown from THF/Et_2O at −35 °C. IR: 3068m, 2948s, 2892s, 2825m, 1480w, 1447m, 1438m, 1361s, 1354s, 1302m, 1259m, 1239s, 1183m, 1135s, 1105s, 1082s, 1035s, 950s, 932m, 904s, 832s, 746s, 687w, 677w, 639w, 628m cm^{-1}. Anal. Calcd for $C_{42}H_{75}N_2O_6Si_3KEu{\cdot}C_4H_8O$: C, 52.54; H, 7.79; N, 2.61. Found: C, 52.43; H, 7.98; N, 2.62. UV−vis (THF) λ_{max}, nm (ε, M^{-1} cm^{-1}): 483 (300), 559 (200 shoulder).

Cp′$_3$Eu, 1-Eu. In an argon-filled glovebox, $AgBPh_4$ (191 mg, 0.447 mmol) was added to a stirred dark magenta-purple solution of [K(2.2.2-cryptand)][Cp′$_3$Eu]·THF, **2-Eu** (427 mg, 0.406 mmol), in THF (10 mL). Within 1 min of stirring, the mixture became dark black/red in color. Black solids, presumably Ag^0, were removed via filtration, and the solvent was removed under vacuum. The tacky residue was stirred in hexane (10 mL) for 30 min, filtered to remove a white solid, presumably [K(2.2.2-cryptand)][BPh_4], and the solvent was removed under vacuum. Several cycles of dissolution in hexane and removal of solvent yielded **1-Eu** as a dark red microcrystalline solid (183 mg, 80%). Dark red crystals of **1-Eu**, suitable for X-ray diffraction, were grown from a concentrated pentane solution at −35 °C. ^{1}H NMR (C_6D_6): δ 53.32 (br s, $C_5H_4SiMe_3$, 27H), 47.60 (br s, $C_5H_4SiMe_3$, 6H), −26.25 (br s, $C_5H_4SiMe_3$, 6H). IR: 3063w, 2953m, 2895w, 2807w, 2361w, 1744w, 1444w, 1405w, 1361m, 1311w, 1243m, 1193w, 1177m, 1044m, 903m, 884w, 833s, 792m, 771s, 751s, 685m, 631m, 533s cm^{-1}. Anal. Calcd for $C_{24}H_{39}Si_3Eu$: C, 51.13; H, 6.97. Found: C, 51.24; H, 6.97.

Cp′$_3$Dy, 1-Dy. As described for **1-Sm**, in an argon-filled glovebox, $DyCl_3$ (492 mg, 1.83 mmol) and KCp′ (1.00 g, 5.67 mmol) were combined to produce **1-Dy** as a microcrystalline bright yellow solid (906 mg, 86%). Bright yellow single crystals of **1-Dy**, suitable for X-ray diffraction, were grown from pentane at −35 °C. ^{1}H NMR (C_6D_6): δ 141 (br s, $C_5H_4SiMe_3$, 6H), −216 (br s, $C_5H_4SiMe_3$, 27H). IR: 3966w, 3914w, 3554w, 3471w, 3067w, 2953m, 2895m, 2717w, 2619w, 2422w, 2385w, 2349w, 2284w, 2233w, 2080w, 1997w, 1932w, 1873w, 1782w, 1753, 1655w, 1555w, 1443m, 1414m, 1400m, 1366m, 1313m, 1243s, 1198m, 1178s, 1063m, 1042s, 904s, 869s, 834s, 796s, 776s, 752s, 685m, 631m cm^{-1}. Anal. Calcd for $C_{24}H_{39}Si_3Dy$: C, 50.19; H, 6.84. Found: C, 49.79; H, 6.74.

[K(2.2.2-cryptand)][Cp′$_3$Dy], 2-Dy. As described for **2-La**, a light yellow solution of **1-Dy** (158 mg, 0.275 mmol) and 2.2.2-cryptand (103 mg, 0.274 mmol) in THF (2 mL) was combined with KC_8 (52 mg, 0.38 mmol) to produce **2-Dy** as a black/dark maroon-purple crystalline solid that analyzed as the solvate [K(2.2.2-cryptand)]-[Cp′$_3$Dy]·THF (124 mg, 43%). Dark purple/green single crystals of **2-Dy·THF**, suitable for X-ray diffraction, were grown from THF/Et_2O at −35 °C. IR: 3078w, 2947m, 2888s, 2825m, 2360w, 1480w, 1447w, 1354m, 1301w, 1260m, 1236m, 1176m, 1135m, 1105s, 1082s, 1036s, 950m, 932w, 903m, 831s, 751m, 673w, 626w cm^{-1}. Anal. Calcd for $C_{42}H_{75}N_2O_6Si_3KDy{\cdot}C_4H_8O$: C, 52.02; H, 7.88; N, 2.64. Found: C, 51.92; H, 8.22; N, 2.63. UV−vis (THF) λ_{max}, nm (ε, M^{-1} cm^{-1}): 483 (3400), 644 (1000 shoulder).

Cp′$_3$Tm, 1-Tm. As described for **1-Sm**, in an argon-filled glovebox, $TmI_3(THF)_{3.5}$ (743 mg, 0.926 mmol) and KCp′ (502 mg, 2.85 mmol) were combined to produce **1-Tm** as a microcrystalline bright yellow solid (510 mg, 95%). Bright yellow single crystals of **1-Tm**, suitable for X-ray diffraction, were grown from pentane at −35 °C. ^{1}H NMR (C_6D_6): δ 153.9 (s, $C_5H_4SiMe_3$, 27H), −32.8 (br s, $C_5H_4SiMe_3$, 6H), −454 (br s, $C_5H_4SiMe_3$, 6H). IR: 3077w, 2953m, 2895w, 2716w, 2361w, 1934w, 1873w, 1760w, 1662w, 1566w, 1443m, 1414m, 1366m, 1314m, 1243s, 1197w, 1178m, 1064m, 1043s, 905m, 834s, 798s, 782s, 752s, 686m, 632m, 564w, 531w cm^{-1}. Anal. Calcd for $C_{24}H_{39}Si_3Tm$: C, 49.63; H, 6.77. Found: C, 49.64; H, 7.04.

[K(2.2.2-cryptand)][Cp′$_3$Tm], 2-Tm. As described for **2-La**, a light yellow solution of **1-Tm** (258 mg, 0.444 mmol) and 2.2.2-cryptand (167 mg, 0.444 mmol) in THF (2 mL) was combined with KC_8 (79 mg, 0.58 mmol) to produce **2-Tm** as a black/brown crystalline solid that analyzed as the solvate [K(2.2.2-cryptand)]-[Cp′$_3$Tm]·THF (313 mg, 66%). Dark brown single crystals of **2-Tm·THF**, suitable for X-ray diffraction, were grown from THF/Et_2O at −35 °C. IR: 3076w, 2948m, 2890s, 2825m, 2764w, 2731w, 2360w, 2341w, 1480w, 1447m, 1382m, 1397w, 1361m, 1354s, 1302m, 1259m, 1240s, 1182m, 1135s, 1105s, 1082s, 1035s, 950m, 932w, 905m, 833s, 748s, 735s, 687w, 677w, 630w, 552w cm^{-1}. Anal. Calcd for $C_{42}H_{75}N_2O_6Si_3KTm{\cdot}C_4H_8O$: C, 51.71; H, 7.83; N, 2.62. Found: C, 51.32; H, 8.27; N, 2.64. UV−vis (THF) λ_{max}, nm (ε, M^{-1} cm^{-1}): 416 (600), 550 (400), 634 (300 shoulder), 794 (100 shoulder).

Cp′$_3$Yb, 1-Yb. As described for **1-Sm**, in an argon-filled glovebox, $YbCl_3$ (751 mg, 2.72 mmol) and KCp′ (1.52 g, 8.62 mmol) were combined to produce **1-Yb** as a microcrystalline forest green solid (338 mg, 22%). Before the pentane extraction, a significant amount of red solids were observed and identified as [Cp′$_2$Yb(μ-Cl)]$_2$ through X-ray diffraction.[58] Dark green single crystals of **1-Yb**, suitable for X-ray diffraction, were grown from pentane at −35 °C. ^{1}H NMR (C_6D_6): δ 44.2 (s, $C_5H_4SiMe_3$, 27H), 43.8 (s, $C_5H_4SiMe_3$, 6H), −21.5 (br s, $C_5H_4SiMe_3$, 6H). IR: 2954m, 2895w, 2388w, 2236w, 2086w, 1933w, 1760w, 1663w, 1568w, 1527w, 1444m, 1410w, 1365m, 1313w, 1244s, 1198m, 1177s, 1063m, 1044s, 906s, 834s, 778s, 752s, 686m, 631m cm^{-1}. Anal. Calcd for $C_{24}H_{39}Si_3Yb$: C, 49.29; H, 6.72 Found: C, 48.65; H, 6.69.

Cp′$_2$Yb(THF)$_2$, 3-Yb. As described for **3-Eu**, in an argon-filled glovebox, $YbI_2(THF)_2$ (790 mg, 1.38 mmol) and KCp′ (500 mg, 2.83 mmol) were combined to produce **3-Yb** as a dark purple diamagnetic solid as identified by ^{1}H NMR spectroscopy[58] (679 mg, 83%).

[K(2.2.2-cryptand)][Cp′$_3$Yb], 2-Yb. As described for **2-Eu**, in an argon-filled glovebox, Cp′$_2$Yb(THF)$_2$, **3-Yb** (664 mg, 1.12 mmol), 2.2.2-cryptand (423 mg, 1.12 mmol), and KCp′ (200 mg, 1.13 mmol) were combined to produce **2-Yb·THF** as emerald green crystals that were suitable for X-ray diffraction (906 mg, 75%). ^{1}H NMR (THF-d_8): δ 5.93 (s, $C_5H_4SiMe_3$, 6H), 5.73 (s, $C_5H_4SiMe_3$, 6H), 3.51 (s, OCH_2CH_2O, 12H), 3.48 (t, $^3J_{HH}$ = 4.5 Hz, NCH_2CH_2O, 12H), 2.50 (t, $^3J_{HH}$ = 4.5 Hz, NCH_2CH_2O, 12H), 0.14 (s, $C_5H_4SiMe_3$, 27H). ^{13}C NMR (C_6D_6): δ 117.0 ($C_5H_4SiMe_3$), 110.7 ($C_5H_4SiMe_3$), 109.2 ($C_5H_4SiMe_3$), 71.3 (OCH_2CH_2O), 68.4 (NCH_2CH_2O), 54.8 (NCH_2CH_2O), 1.6 ($C_5H_4SiMe_3$). IR: 3075w, 2949m, 2890m, 2826m, 1480w, 1438m, 1354s, 1302m, 1259m, 1240s, 1183m, 1135s, 1105s, 1081s, 1035s, 945s, 932m, 905s, 832s, 738s, 677m, 638m, 630m, 571m cm^{-1}. Anal. Calcd for $C_{42}H_{75}N_2O_6Si_3KYb{\cdot}C_4H_8O$: C, 51.51; H, 7.80; N, 2.61. Found: C, 51.13; H, 7.81; N, 2.47. UV−vis (THF) λ_{max}, nm (ε, M^{-1} cm^{-1}): 335 (900 shoulder), 378 (800), 534 (50), 684 (200).

X-ray Data Collection, Structure Determination, and Refinement. Crystallographic details for compounds **2-La**, **2-Ce**, **2-Nd**, **1-Sm**, **2-Sm**, **1-Eu**, **2-Eu**, **1-Dy**, **2-Dy**, **1-Tm**, **2-Tm**, **1-Yb**, and **2-Yb** are summarized in the Supporting Information. **1-Ln** complexes for all the lanthanides (except unknown Pm) are isomorphous, as are all the complexes in the series **2-Ln**.

Computational Details. Density functional theory (DFT) calculations were carried out on **1-Ln** and the anion of **2-Ln** for Ln = Nd, Sm, Eu, Dy, Tm, and Yb using the hybrid meta-generalized gradient approximation functional TPSSH.[59,60] All computations were performed using the TURBOMOLE program package.[61] Small-core effective core potentials (ECPs),[62] along with triple-ζ basis sets (def-TZVP),[63] were employed for heavy atoms, and augmented polarized split-valence basis sets (def2-SVPD)[64] were employed for light atoms. Solvation effects were taken into account through the continuum solvation model (COSMO)[65] using the dielectric constant of THF (ε = 7.520).[66] Time dependent DFT (TDDFT)[67] calculations were performed to simulate the UV−vis spectrum of **2**. A full description of the computational methods is supplied in the Supporting Information.

DOI: 10.1021/ja510831n
J. Am. Chem. Soc. 2015, 137, 369−382

RESULTS

Synthesis of Cp′$_3$Ln (Ln = Sm, Dy, Tm). The synthesis of the previously unknown Cp′$_3$Ln complexes, **1** (Ln = Sm, Eu, Dy, Tm, Yb), needed as precursors in this study and for structural comparison, was attempted following the published syntheses of analogs of the other metals.[31−33,54−57] For Ln = Sm and Dy, the reaction of 3 equiv of KCp′ with $LnCl_3$ generated the desired bright orange Cp′$_3$Sm, **1-Sm**, and bright yellow Cp′$_3$Dy, **1-Dy**, Scheme 3. Since the analogous metal

Scheme 3. Routes for Synthesizing Cp′$_3$Ln Compounds, 1, from Lanthanide Trihalide Starting Materials

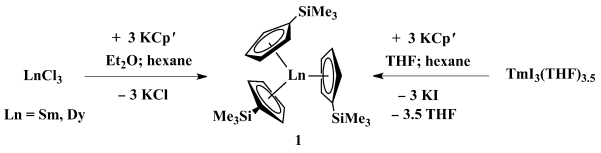

trichloride reaction was not as successful with thulium, bright yellow Cp′$_3$Tm, **1-Tm**, was prepared from the iodide precursor, $TmI_3(THF)_{3.5}$,[51] with 3 equiv of KCp′, Scheme 3. **1-Sm**, **1-Dy**, and **1-Tm** were characterized by X-ray crystallography (see Supporting Information) and were found to be isomorphous with the other **1-Ln** complexes.[31−33,54−57]

Synthesis of Cp′$_3$Ln (Ln = Eu, Yb) and [K(2.2.2-cryptand)][Cp′$_3$Ln] (Ln = Eu, Yb). Attempts to make Cp′$_3$Eu, **1-Eu**, from $EuCl_3$ according to Scheme 1 were not successful. This was not unexpected, since it is known that the reaction of 3 equiv of NaC_5Me_5 with $EuCl_3$ resulted in the isolation of the Eu^{2+} complex $(C_5Me_5)_2Eu(THF)$ rather than $(C_5Me_5)_3Eu$.[68] Similarly, the reaction of $EuCl_3$ with 2 equiv of KCp^R [Cp^R = $C_5H_4CH(SiMe_3)_2$] to make Cp^R_2EuCl yielded only the Eu^{2+} complex, $Cp^R_2Eu(THF)_2$.[27] This preference to form +2 complexes for europium and ytterbium is attributed to stabilization due to the half-filled and completely filled 4f electron configurations, $4f^7$ and $4f^{14}$, respectively, and the concomitant low reduction potentials, Table 1. To circumvent these problems, a reverse approach was used involving first the synthesis of the +2 complexes, **2**, and then subsequent oxidation to form the +3 compounds, **1**, needed for structural comparison.

Both $EuI_2(THF)_2$[50] and $YbI_2(THF)_2$[49] react with 2 equiv of KCp′ to produce Cp′$_2$Eu(THF)$_2$, **3-Eu**, and Cp′$_2$Yb(THF)$_2$, **3-Yb**, as bright orange-red and purple crystalline solids, respectively, eq 1. Complex **3-Yb** had been previously

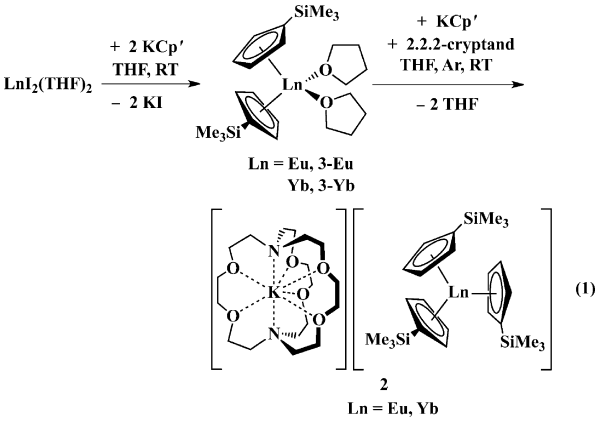

synthesized by Na(Hg) reduction of [Cp′$_2$Yb(μ-Cl)]$_2$, and its identity was verified by ^{1}H NMR spectroscopy.[58] Although **3-Eu** was too paramagnetic to be observed by NMR, single-crystal X-ray diffraction confirmed its composition and structure. The structure of **3-Eu** is isomorphous with **3-Yb**, but the low quality data precluded a detailed structural discussion.

To obtain the desired [K(2.2.2-cryptand)][Cp′$_3$Ln] products, **2-Eu** and **2-Yb**, K(2.2.2-cryptand)Cp′ was added to **3-Eu** and **3-Yb**, eq 1. Lappert reported a similar reaction in 1998 involving Cp″$_2$Sm, KCp″, and 18-crown-6 to make [K(18-crown-6)(toluene)$_2$][Cp″$_3$Sm] [Cp″ = $C_5H_3(SiMe_3)_2$].[35] Purple **2-Eu** and emerald **2-Yb** were characterized by X-ray crystallography (Figure 1), IR spectroscopy, and elemental

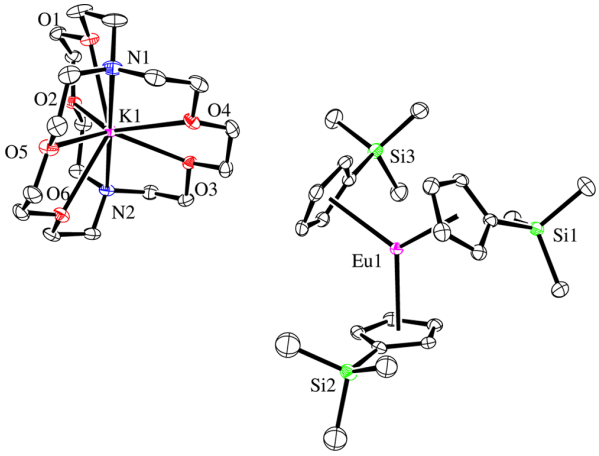

Figure 1. Molecular structure of [K(2.2.2-cryptand)][Cp′$_3$Eu], **2-Eu**, with thermal ellipsoids drawn at the 50% probability level. One set of disordered carbons in a disordered trimethylsilyl group, a disordered cocrystallized THF, and hydrogen atoms are omitted for clarity.

analysis. Complex **2-Yb** exhibited a ^{1}H NMR spectrum that was characteristic of a diamagnetic compound, which is consistent with its electron configuration being $4f^{14}$ and not $4f^{13}5d^1$.

The Eu^{3+} complex, Cp′$_3$Eu, **1-Eu**, needed for structural comparison was made by oxidation of [K(2.2.2-cryptand)][Cp′$_3$Eu], **2-Eu**, with $AgBPh_4$. The dark red product was identified by X-ray crystallography, elemental analysis, and IR spectroscopy, eq 2. The Yb^{3+} analog, **1-Yb**, was also synthesized

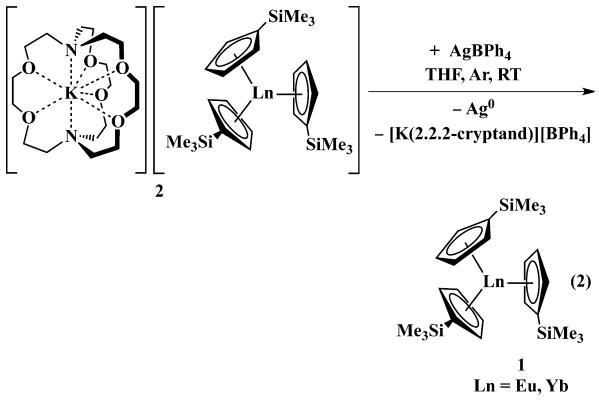

DOI: 10.1021/ja510831n
J. Am. Chem. Soc. 2015, 137, 369−382

by the oxidation of [K(2.2.2-cryptand)][Cp′$_3$Yb], **2-Yb**, with $AgBPh_4$ and identified by X-ray crystallography, eq 2. The green **1-Yb** can also be synthesized by reacting 3 equiv of KCp′ with $YbCl_3$, Scheme 3, although the latter reaction produced significant amounts of the known byproduct, [Cp′$_2$Yb(μ-Cl)]$_2$.[69]

Synthesis of [K(2.2.2-cryptand)][Cp′$_3$Ln], 2 (Ln = La, Ce, Nd, Sm, Dy, Tm). Following the procedure previously reported for Ln = Pr, Gd, Tb, Y, Ho, Er, and Lu,[33] which required short reaction times and fast isolation procedures, the Cp′$_3$Ln complexes **1-La**, **1-Ce**, **1-Nd**, **1-Sm**, **1-Dy**, and **1-Tm** were reacted with KC_8 in the presence of 2.2.2-cryptand in THF under argon. These reactions yielded deeply colored crystalline products, all of which were determined by X-ray crystallography to be [K(2.2.2-cryptand)][Cp′$_3$Ln], **2**, eq 3.

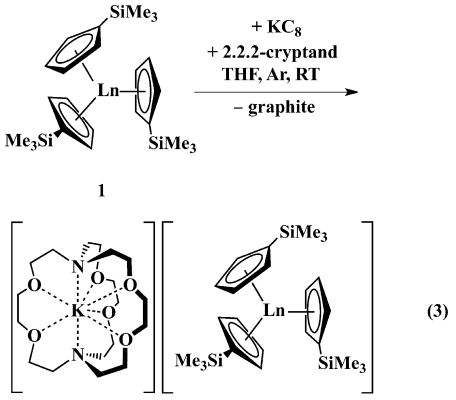

(3)

The lanthanum complex, **2-La**, displays an isotropic EPR spectrum, Figure 2, that is very similar to the La^{2+} spectra

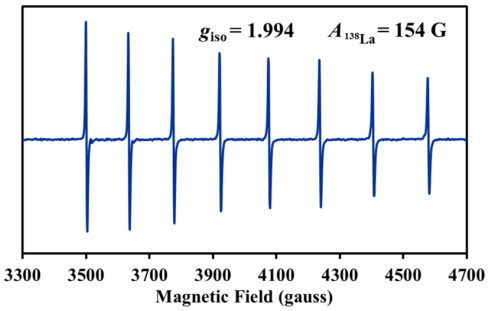

Figure 2. Room temperature X-band EPR spectrum of [K(2.2.2-cryptand)][Cp′$_3$La], **2-La**, in THF under argon.

reported for the [Cp″$_3$La]$^{1-}$ anion by Lappert et al.[30,70] The octet pattern is evidence of an unpaired electron coupled to the $I = {}^7/_2$ nuclear spin of ^{138}La (99.9% natural abundance). The large average coupling constant of 154 G and the g_{iso} value of 1.994 (similar to the 133.5 G and g_{av} = 1.990 of [Cp″$_3$La]$^{1-}$) are both indicative of a metal-centered radical and consistent with the $5d^1$ configuration assigned to La^{2+}.[30] These EPR data can also be compared to the data on the $6d^1$ Th^{3+} complexes, [$C_5H_3(SiMe_3)_2$-1,3]$_3$Th,[71,72] [$C_5H_3(SiMe_2{}^tBu)_2$-1,3]$_3$Th,[71] (C_5Me_5)$_2$[^{i}PrNC(Me)N^{i}Pr]Th,[73] [K(DME)$_2$]-{[$C_8H_6(Si{}^tBuMe_2)_2$]$_2$Th},[74] and (C_5Me_4H)$_3$Th[75] that have EPR spectra with g values of 1.87–1.92.

Structural Comparisons. Crystallographic information was obtained on the Ln^{3+} complexes **1** (Sm, Eu, Dy, Tm, and Yb) to complement that already in the literature (La,[54] Ce,[55,56] Nd[57]) so that a direct structural comparison of **1** and **2** could be made for these metals to add to the data already available on the other metals in the series.[33] The differences between the Ln–(Cp′ centroid) distances of **1** and **2** for Ln = La and Ce, 0.027 and 0.029 Å, respectively, match the small differences observed between **1** and **2** for the Ln^{2+} ions in Scheme 2 where Ln = Y,[31] Ho,[32] Er,[32] Tb,[33] Pr,[33] Gd,[33] Lu[33] (0.027–0.032 Å) and between Scheme 1 complexes Cp″$_3$La and [Cp″$_3$La]$^{1-}$ (0.020–0.032 Å).[30] These small changes in bond length are typical in transition metal chemistry[41] and are consistent with the assignment of a $4f^n5d^1$ configuration rather than a $4f^{n+1}$ configuration for the +2 ions of these lanthanide metals. The $5d^1$ configuration has previously been assigned[30] to La^{2+} in [Cp″$_3$Ln]$^{1-}$, and yttrium necessarily has a $4d^1$ configuration.

In contrast to these small differences, the differences in Ln–(Cp′ centroid) distances of **1** and **2** for *four of the traditional six* divalent lanthanides are larger: 0.156 Å (Eu), 0.143 Å (Yb), 0.147 Å (Sm), and 0.123 Å (Tm) (Table 2, listed in the order of increasingly negative Ln^{3+}/Ln^{2+} reduction potentials in Table 1). These larger values match the 0.10–0.20 Å differences found historically for metal–ligand bonds in Ln^{2+} complexes of Eu, Yb, Sm, Tm, Dy, and Nd[9,10,18,34–37] when compared to their Ln^{3+} analogs. These four 0.123–0.156 Å differences in Ln–(Cp′ centroid) distances between **1** and **2** are consistent with those expected for a $4f^{n+1}$ Ln^{2+} complex vs a $4f^n$ Ln^{3+} species. This consistently large difference is attributed to the special nature of the 4f orbitals and their limited radial extension that minimizes metal ligand interaction and causes these complexes to behave more as complexes of "free ions" rather than d-block complexes. Both the spectroscopy and magnetism of complexes of these traditional Ln^{2+} ions support this free ion view.[16,17,76–81]

Although four of the traditional six Ln^{2+} ions in complexes of **2** have large Ln–(Cp′ centroid) distances compared to the Ln^{3+} analogs, **1**, complexes of Dy^{2+} and Nd^{2+} do not (Table 2). The Ln^{3+}/Ln^{2+} difference between **1** and **2** for Dy is 0.036 Å and for Nd is 0.030 Å. This puts these two metals in the same category as the metals that are expected to have $4f^n5d^1$ configurations in the +2 oxidation state. Hence, in this comparison of the structures of **1** and **2** for all the lanthanides, the complexes of Ln = Eu, Yb, Sm, and Tm fall into one class and the complexes of Ln = La, Ce, Pr, Nd, Gd, Tb, Dy, Ho, Er, and Lu fall into the other class.

The data on **1** and **2** for Ln = Dy and Nd contrast with most of the data in the literature to date on Dy^{2+} and Nd^{2+} complexes. In general, Shannon radii for eight-coordinate Dy^{2+} and Nd^{2+} are 0.163 and 0.181 Å larger than those of Dy^{3+} and Nd^{3+}, respectively.[37] These numbers are based on solid state structures obtained up to 1976 before molecular examples of Dy^{2+} and Nd^{2+} were known.[9,10] Molecular examples of these ions also show the same trend. For example, the Ln–I distances in $NdI_2(THF)_5$[10] are 0.22 Å larger than those in [$NdI_2(THF)_5$]$^{1+}$.[36] A Dy^{3+} analog of $DyI_2(DME)_3$[9] is not available for comparison, but the Dy–I distances are actually longer than expected compared to the analogous isomorphous $SmI_2(DME)_3$,[82] which has long Sm–I distances typical of a $4f^{n+1}$ Sm^{2+} ion.

DOI: 10.1021/ja510831n
J. Am. Chem. Soc. 2015, 137, 369–382

Table 2. Experimental and Calculated Average Ln−(Cp′ Centroid) Distances (Å) in Cp'_3Ln, 1, and [K(2.2.2-cryptand)][Cp'_3Ln], 2, for the Traditional Six +2 Ions, Eu, Yb, Sm, Tm, Dy, and Nd, Listed in the Order of Ln^{3+}/Ln^{2+} Reduction Potentials (Table 1)[17,22]

	experimental		calculated	
compd	Ln−(Cp′ centroid)$_{avg}$	difference	Ln−(Cp′ centroid)$_{avg}$	difference
1-Eu/2-Eu	2.451/2.607	0.156	2.485/2.604	0.117
1-Yb/2-Yb	2.365/2.508	0.143	2.391/2.495	0.104
1-Sm/2-Sm	2.461/2.608	0.147	2.470/2.600	0.130
1-Tm/2-Tm	2.379/2.502	0.123	2.385/2.501	0.116
1-Dy/2-Dy	2.407/2.443	0.036	2.490/2.563	0.073
1-Nd/2-Nd	2.489/2.519	0.030	2.489/2.509	0.020

In the course of this structural analysis, Si−C bond distances were also analyzed for **1** and **2**, since it has been suggested that the electron added to **1** to make **2** could go into the ligands and be reflected in longer Si−C(Me) or Si−C(ring) bonds.[33] Full data are given in the Supporting Information, but there is no discernible difference between the Si−C distances in **1** and **2** for any of the metals. For example, the average Si−C(Me) distance for **2-Y** is 1.872 Å vs 1.868 Å for **1-Y**. This is quite similar to the average Si−C(Me) distances of 1.873 Å for **2-Eu** and 1.867 Å for **1-Eu**.

UV−Visible Spectroscopy. The UV−vis spectra of **2-La**, **2-Ce**, **2-Dy**, and **2-Nd** are shown in Figure 3 along with the spectra for **2-Y**, which necessarily contains a $4d^1$ ion, and **2-Lu**, which is a $5d^1$ complex since the f shell of the $4f^{14}$ Lu^{3+} ion is filled. These spectra are very similar to those of **2-Gd**, **2-Tb**, **2-Ho**, and **2-Er** complexes previously analyzed to have $4f^n5d^1$ ground states.[32,33] Each complex has intense absorptions with extinction coefficients of 3000−4000 M^{-1} cm^{-1} in the high energy visible region. The spectra differ greatly from those of the corresponding Ln^{3+} complexes **1**. The +3 complexes have low extinction coefficients, since the 4f−4f transitions are Laporte forbidden, and display narrow line widths, since vibronic broadening is minimal due to the limited radial extension of the 4f orbitals.

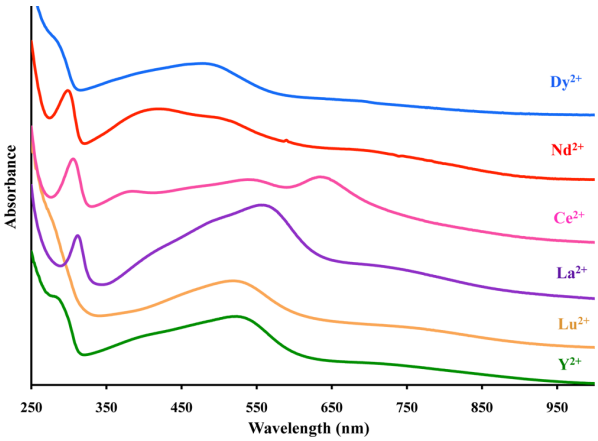

Figure 3. Stacked plot of experimental UV−vis spectra of [K(2.2.2-cryptand)][Cp'_3Ln], **2**, for Ln = La, Ce, Nd, and Dy in comparison to Y and Lu, in THF at 298 K. Maximum extinction coefficients for absorption at wavelengths greater than 350 nm (M^{-1} cm^{-1}) follow: Y (4500), Lu (4500), La (4400), Ce (4700), Nd (4700), Dy (3400).

The UV−vis spectra of **2-Eu**, **2-Yb**, **2-Sm**, and **2-Tm** are dramatically different from those of the other [K(2.2.2-cryptand)][Cp'_3Ln] complexes as shown in Figure 4. For these four metals, the absorptions have lower extinction coefficients, $\varepsilon \leq 900$ M^{-1} cm^{-1}, compared to the other **2-Ln** complexes including **2-Dy** and **2-Nd**, also shown for comparison in Figure 4. This difference in absorbance is visually noticeable: solutions of **2-Eu**, **2-Yb**, **2-Sm**, and **2-Tm** are less intensely colored than those of the other analogs of **2**. The absorptions of the traditional $4f^{n+1}$ Ln^{2+} ions are attributed to Laporte allowed 4f−5d transitions.[76]

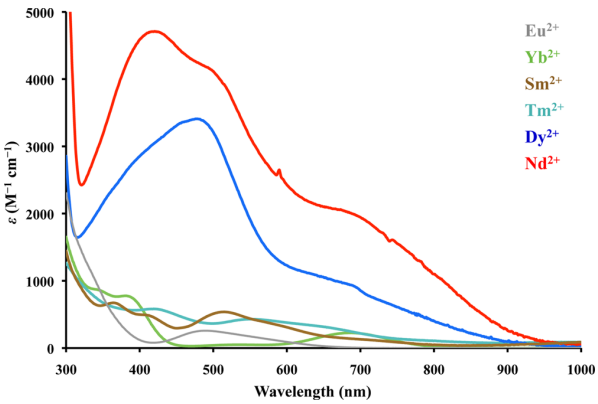

Figure 4. Experimental UV−vis spectra of [K(2.2.2-cryptand)][Cp'_3Ln], **2** (Ln = Nd, Sm, Eu, Dy, Tm, Yb), in THF at 298 K.

THEORETICAL ANALYSIS

Density functional theory (DFT) calculations were performed on both Cp'_3Ln, **1**, and $[Cp'_3Ln]^{1-}$, **2**, for the six lanthanides that traditionally have +2 oxidation states, Ln = Eu, Yb, Sm, Tm, Dy, and Nd, to compare with the calculations reported earlier on the new divalent ions.[32,33]

Ln^{3+}. Because of the presence of many low-lying excited states and small HOMO−LUMO gaps, self-consistent field calculations of open-shell lanthanide compounds are notoriously difficult to converge. Nevertheless, calculations on the Ln^{3+} complexes **1** converged smoothly in each case except for Dy. For Eu, Yb, Sm, Tm, and Nd, the lowest energy structures matched crystallographic data within a few hundredths of an angstrom (Table 2) as observed previously for the other lanthanides.[32,33] In the case of the $4f^9$ Dy^{3+} ion, convergence thresholds were initially lowered and Fermi smearing of occupation numbers with simulated annealing was used.[83] Once a reasonable structure was obtained, energy and density thresholds were tightened and the calculation converged to an integer $4f^9$ occupation.

DOI: 10.1021/ja510831n
J. Am. Chem. Soc. 2015, 137, 369−382

Eu^{2+}, Yb^{2+}, Sm^{2+}, and Tm^{2+}. The computed structures of the anionic complexes **2**, $[Cp'_3Ln]^{1-}$, for the four metals, Ln = Eu, Yb, Sm, and Tm, agree well with the structural and spectroscopic data presented above. For each of these metals, the calculations predict structures of **2** that match the experimental data (Table 2). For these four metals, the differences between the Ln−(Cp′ centroid) distances of the calculated structures of **1** and **2** are significantly larger than the 0.023−0.034 Å difference calculated for Ln = Pr, Gd, Tb, Ho, Er, Y, and Lu.[32,33] Specifically, the DFT calculated Ln^{3+}/Ln^{2+} bond length differences for these four metals in **2** vs **1** are Eu, 0.12 Å; Yb, 0.10 Å; Sm, 0.13 Å; Tm, 0.12 Å. The calculations agree with the larger differences found for these ions experimentally in this paper and in other studies.[9,10,18,34−37,82]

The calculations on Eu, Yb, Sm, and Tm also reveal a different character of the LUMO of the trivalent **1** and the HOMO of the anion of divalent **2** compared to the other metals. For Ln = Pr, Gd, Tb, Ho, Er, Y, and Lu, both the LUMO of **1** and HOMO of **2** appear to be almost identical d_{z^2} orbitals.[32,33] However, for Eu and Yb, the LUMO of **1** and the HOMO of **2** are similar six-lobe 4f-like orbitals (Supporting Information). For Sm and Tm, the LUMO of **1** and the HOMO of **2** differ: the LUMO of **1** is a six-lobe 4f orbital, while the HOMO of **2** resembles a 4f orbital with eight lobes, Figure 5 (Supporting Information for Sm). The LUMOs of **1**

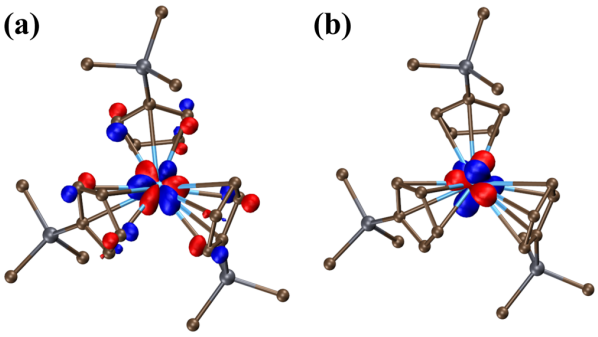

Figure 5. Molecular orbital plots of (a) the 134a orbital (LUMO) of **1-Tm** and (b) the 133a orbital (HOMO) of the anion in **2-Tm**, using a contour value of 0.05.

for these four ions have significant ligand character as shown in Figure 5 for **1-Tm** which has 41% ligand character by Mulliken population analysis.[84] The fully optimized structures of the anion of **2-Ln** for Ln = Eu, Yb, Sm, and Tm all contain an entirely metal-based HOMO.

The energy difference between $4f^{n+1}$ and $4f^n5d^1$ configurations for Eu, Yb, Sm, and Tm was estimated by the Δ self-consistent field method. This resulted in 4f to 5d transfer energies of 51.8 kcal/mol (18 100 cm^{-1}) for Eu, 49.6 kcal/mol (17 300 cm^{-1}) for Yb,[85] and 29.3 kcal/mol (10 200 cm^{-1}) for Tm. These numbers can be compared with the differences between the $4f^n$ and $4f^n5d^1$ levels obtained experimentally from atomic spectra of the Ln^{2+} ions: Eu, 96.9 kcal/mol (33 900 cm^{-1}); Yb, 95.5 kcal/mol (33 400 cm^{-1}); Sm, 70.0 kcal/mol (24 500 cm^{-1}); Tm, 65.5 kcal/mol (22 900 cm^{-1}).[86]

Natural population analysis (NPA) supports the notion that the Ln^{2+} complexes, $[Cp'_3Eu]^{1-}$, $[Cp'_3Yb]^{1-}$, $[Cp'_3Sm]^{1-}$, and $[Cp'_3Tm]^{1-}$, each have approximately one electron added to the f orbitals in comparison to the Ln^{3+} Cp'_3Ln complexes, Table 3. This suggests $4f^7$, $4f^{14}$, $4f^6$, and $4f^{13}$ ground states for

Table 3. NPA Comparison between Cp'_3Ln and $[Cp'_3Ln]^{1-}$ [a]

	$Cp'_3Ln/[Cp'_3Ln]^{1-}$		difference	
Ln	4f e^{1-}	4d and 5d e^{1-}	4f e^{1-}	4d and 5d e^{1-}
Eu	6.556/6.952	10.989/10.675	+0.396	−0.214
Yb	13.465/13.919	10.989/10.725	+0.454	−0.264
Sm	5.373/5.927	11.111/10.702	+0.554	−0.409
Tm	12.277/12.911	11.110/10.746	+0.634	−0.364
Dy	8.936/8.981	11.062/10.899	+0.045	−0.163
Nd	3.221/3.530	11.188/11.177	+0.309	−0.011
La	0.016/0.018	0.934/1.222	+0.002	+0.288

[a]The number of 4f electrons (left) and the number of 4d and 5d electrons combined (right) are compared for the two complexes.

$[Cp'_3Eu]^{1-}$, $[Cp'_3Yb]^{1-}$, $[Cp'_3Sm]^{1-}$, and $[Cp'_3Tm]^{1-}$, respectively. This matches all previous data on +2 ions of these metals including the structurally similar [K(18-crown-6)$(toluene)_2$][Cp''_3Sm].[35] Specifically, Table 3 shows that for Eu, Yb, Sm, and Tm, the sum of 4d and 5d electron density does not change much between the Ln^{3+} complex and the Ln^{2+} complex and even decreases, whereas the 4f electron density increases from the +3 ion to the +2 ion. For Nd and Dy, the changes in 4f and 5d population are smaller. This can be attributed to partially mixed 4f/5d ground-state configurations. The situation for La is very different: each ion has very little 4f character, and the 5d population increases.

The UV−vis spectra of **2-Ln** were simulated using TDDFT calculations that take into account solvent effects via a continuum solvent model COSMO.[65] Figure 6 shows the experimental and calculated spectra for these Ln^{2+} complexes.

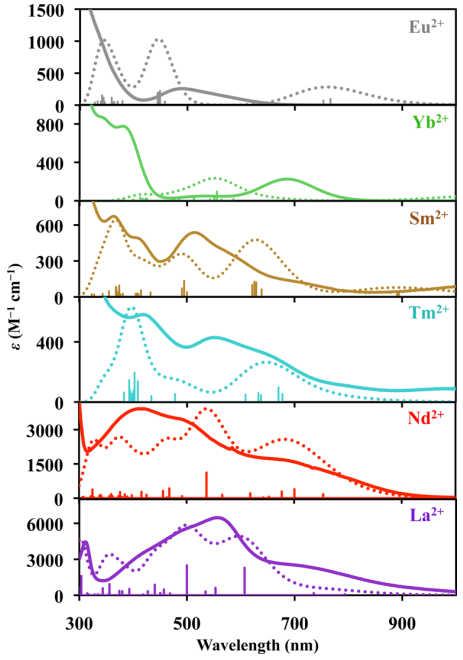

Figure 6. Experimental (solid) and calculated (dotted) UV−vis spectra of [K(2.2.2-cryptand)][Cp'_3Ln], **2** (Ln = Eu, Yb, Sm, Tm, Nd), in THF at 298 K, with pertinent theoretical excitations shown as vertical lines and theoretical extinction coefficients scaled up by a factor to best match the experimental. Calculated UV−vis spectra for **2-Dy** are shown in Figure 9.

DOI: 10.1021/ja510831n
J. Am. Chem. Soc. 2015, 137, 369−382

Examination of the largest calculated transitions in the spectra of the Eu, Yb, Sm, and Tm complexes corroborates the traditional view that the absorptions arise from 4f−5d transitions[76] (see Table S19 in the Supporting Information). Several transitions originate from primarily occupied 4f orbitals that lie below the HOMO level to the 5d LUMO.

Nd^{2+}. In the case of Ln = Nd, the LUMO of **1-Nd** has primarily 4f orbital character, but the HOMO of **2-Nd** has d_{z^2} orbital character, Figure 7. Although there is no requirement

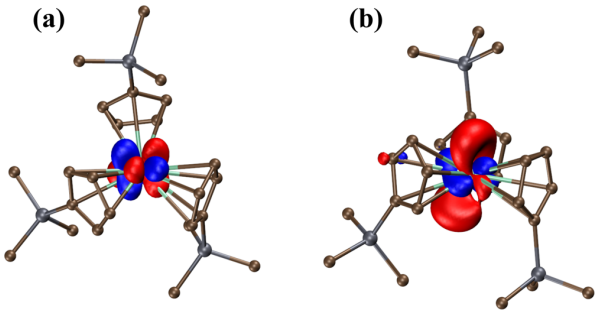

Figure 7. Molecular orbital plots of (a) the 131a orbital (LUMO) of **1-Nd** and (b) the 131a orbital (HOMO) of the anion in **2-Nd**, using a contour value of 0.05.

that the LUMO of the +3 ion should match the HOMO of the +2 ion, this Nd result differed from all previous calculations comparing **1** and **2**.[32,33] With all the other metals, the LUMO of **1** and the HOMO of **2** were either both d orbitals or both f orbitals. Close inspection of the HOMO of **2-Nd** shows that although it is primarily d_{z^2} in nature, the torus of the orbital appears to divide into four small lobes that suggest partial 4f character. Mulliken analysis[84] of this orbital suggests that the 90% metal contribution to the orbital comprises 29% d and 60% f.

The difference in Ln−(Cp′ centroid) distances of the calculated structures of **1-Nd** and **2-Nd** was 0.020 Å, similar to the experimentally determined value, 0.030 Å. This puts Nd in the category of the Ln^{2+} complexes with $4f^n5d^1$ configurations. The calculated Nd UV−vis spectrum is consistent with this assignment in that the major transitions are metal to ligand and not f to d as in the spectra for Eu, Yb, Sm, and Tm.

Dy^{2+}. As mentioned above, the calculations for dysprosium were problematic even at the Dy^{3+} level. Calculations on **2-Dy** predicted a $4f^{10}$ configuration, i.e., a $4f^{n+1}$ configuration like that of Eu, Yb, Sm, and Tm, even though the structural and spectroscopic information suggested that Dy^{2+} is more like the Ln^{2+} complexes with $4f^n5d^1$ configurations. The LUMO of **1-Dy** and the HOMO of **2-Dy** match: both are 4f orbitals with six lobes, Figure 8. The vertical excitation energy to the $5d^1$ occupation is calculated to be 17.8 kcal/mol. This is smaller than the 29.3−51.8 kcal/mol values calculated for Eu, Yb, and Tm (see above) and is consistent with Dy being a "crossover" element[21] in the **2** series where the 4f and 5d energy levels are so similar that there is difficulty elucidating the ground states. The difference in Ln−(Cp′ centroid) distances of the calculated structures of **1-Dy** and **2-Dy** was 0.073 Å. This is intermediate between the experimentally found 0.020−0.032 Å differences of Ln^{2+} complexes with $4f^n5d^1$ configurations and the 0.123−0.156 Å differences of the $4f^{n+1}$ complexes.

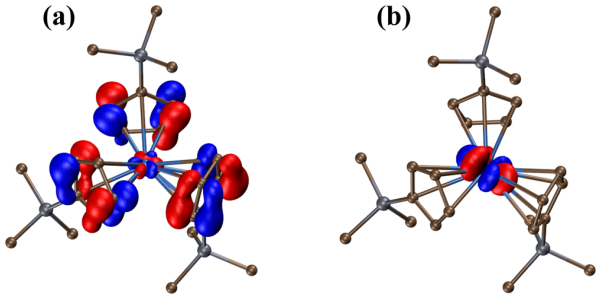

Figure 8. Molecular orbital plots of (a) the 134a orbital (LUMO) of **1-Dy** and (b) the 130a orbital (HOMO) of the anion in **2-Dy**, using a contour value of 0.05.

The UV−vis spectra of **2-Dy** were also simulated for both the ground state $4f^{10}$ configuration and a higher lying $4f^95d^1$ configuration, Figure 9. The simulated spectrum for the

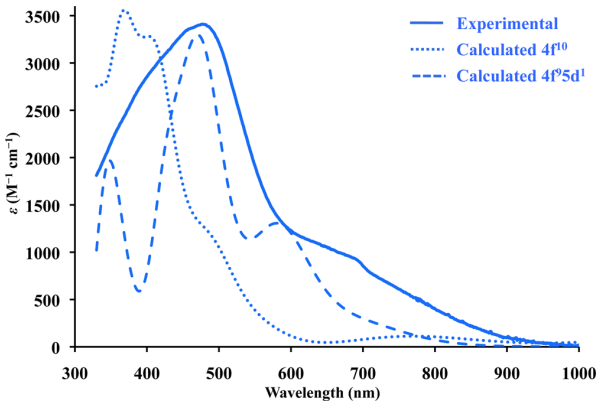

Figure 9. Experimental UV−vis spectrum of [K(2.2.2-cryptand)][Cp'_3Dy], **2-Dy**, in THF at 298 K (solid line) with calculated spectra using a $4f^{10}$ ground state configuration (dotted) and a higher lying $4f^95d^1$ state configuration. Theoretical extinction coefficients are scaled up by a factor of 12 000 for the $4f^{10}$ configuration and 2700 for the $4f^95d^1$ configuration.

$4f^95d^1$ case matches the experimental spectrum much better than that of the $4f^{10}$ configuration. Hence, although DFT predicts the $4f^{n+1}$ configuration to be more stable, the spectroscopic data are more consistent with a $4f^n5d^1$ ground state.

DISCUSSION

Synthesis. The synthesis, isolation, and structural determination of the Cp'_3Ln, **1**, and [K(2.2.2-cryptand)][Cp'_3Ln], **2**, compounds have been accomplished for all nonradioactive lanthanides. This provides the rare opportunity to directly compare analogous complexes of all the lanthanides as well as yttrium in the same coordination environment in both the +3 and +2 oxidation states. Making direct structural and electronic comparisons of the entire rare earth series with a single ligand set is challenging, since the steric requirements for thermally stable and crystalline complexes can often change across the series as the radial size diminishes. Fortunately, this was not a problem with the $(Cp'_3)^{3-}$ ligand set with the metals in both the +2 and +3 oxidation states.

DOI: 10.1021/ja510831n
J. Am. Chem. Soc. 2015, 137, 369−382

Structural Data. All members of the Cp'_3Ln, **1**, series are isomorphous; their structures vary only slightly from metal to metal because of the gradually changing radial size of the metal ion. This change in average Ln−(Cp′ centroid) distance vs atomic number, Figure 10, follows a quadratic decay as described previously in the literature.[87,88]

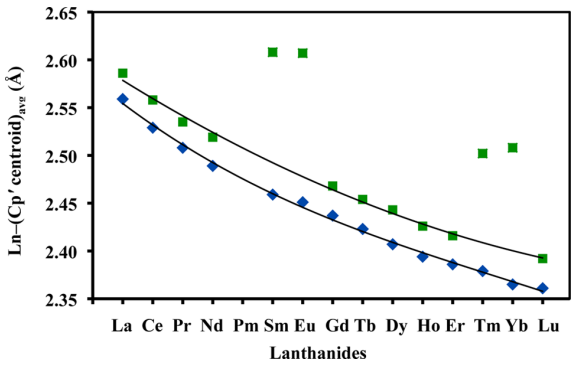

Figure 10. Plot of average Ln−(Cp′ centroid) distances in Cp'_3Ln, **1** (blue diamonds), and in [K(2.2.2-cryptand)][Cp'_3Ln], **2** (green squares), for each lanthanide metal.

Since the average Ln−(Cp′ centroid) distances in [K(2.2.2-cryptand)][Cp'_3Ln], **2**, for La, Ce, Pr, Nd, Gd, Tb, Dy, Ho, Er, and Lu are about 0.03 Å longer than those in the corresponding complexes of **1**, plotting these distances for these metals in Figure 10 gives a curve that is similar to that for the complexes of the +3 ions. Since the differences in Ln−(Cp′ centroid) bond distances for **1** vs **2** with Ln = Eu, Yb, Sm, and Tm, 0.123−0.156 Å, are much larger than the 0.03 Å difference for the other metals, their points lie significantly above the trend lines in Figure 10.

The structural differences between the complexes of Eu, Yb, Sm, Tm and the complexes of the 10 other lanthanides, La, Ce, Pr, Nd, Gd, Tb, Dy, Ho, Er, and Lu, as well as Y, can be explained by two different electron configurations for their Ln^{2+} ions. With Eu, Yb, Sm, and Tm, large differences are found because reduction of a $4f^n$ Ln^{3+} ion generates a $4f^{n+1}$ Ln^{2+} ion. Since there is little interaction of the 4f orbitals with the ligands, the bond distances are simple sums of ionic radii. Since the ionic radii of $4f^{n+1}$ Ln^{2+} ions are typically 0.1−0.2 Å larger than the $4f^n$ Ln^{3+} ions,[37] the metal−ligand bond distances in the complexes are similarly larger. With La, Ce, Pr, Nd, Gd, Tb, Dy, Ho, Er, and Lu, small differences are found because reduction of a $4f^n$ Ln^{3+} ion generates a $4f^n5d^1$ Ln^{2+} ion for the lanthanides and a $4d^1$ ion for yttrium. Since the d orbitals can interact with the ligands, the bond distances are not necessarily simple sums of ionic radii. This is typical in transition metal complexes in which many factors contribute to bond distances and simple correlations with oxidation states are not observed.[41]

Spectral Data. The UV−vis spectral data on the complexes, [K(2.2.2-cryptand)][Cp'_3Ln], **2**, match the structural results above. The set of four ions, Eu^{2+}, Yb^{2+}, Sm^{2+}, and Tm^{2+}, in **2** display different UV−vis spectra from those of the rest. The spectra for La^{2+}, Ce^{2+}, Pr^{2+}, Nd^{2+}, Gd^{2+}, Tb^{2+}, Dy^{2+}, Ho^{2+}, and Er^{2+} have overall shapes and intensities similar to those seen for the Y^{2+} and Lu^{2+} ions that are necessarily $4d^1$ and $4f^{14}5d^1$ systems, respectively.[31−33] The DFT calculations indicate that they arise from metal to ligand transitions. The spectra for Eu^{2+}, Yb^{2+}, Tm^{2+}, and Sm^{2+} complexes of **2** have different shapes and are weaker in intensity than the $4f^n5d^1$ complexes. They can be modeled as 4f−5d transitions occurring from a $4f^{n+1}$ ground state.[76]

"Set of Four" vs "Traditional Six" Ln^{2+} Ions. An unusual feature about the structural and spectroscopic data reported here is that complexes of Dy^{2+} and Nd^{2+} ions have properties consistent with $4f^n5d^1$ configurations rather then the traditional $4f^{n+1}$ configurations obtained by adding an electron to a $4f^n$ Ln^{3+} ion. The data in this study suggest that the $(Cp'_3)^{3-}$ ligand set can change the ground state from $4f^{n+1}$ to $4f^n5d^1$ for these two ions. Hence, the previous classification of +2 lanthanide ions into the traditional six $4f^{n+1}$ ions with Ln = Eu, Yb, Sm, Tm, Dy, and Nd and the nontraditional $4f^n5d^1$ ions with Ln = La, Ce, Pr, Gd, Tb, Ho, Er, and Lu and $4d^1$ Y must be modified in the sense that this dichotomy is apparently dependent on the ligand environment. In some coordination environments, specifically the $(Cp'_3)^{3-}$ ligand set, Dy and Nd can adopt the $4f^n5d^1$ electron configuration. With this $(Cp'_3)^{3-}$ set of ligands, there are only four traditional $4f^{n+1}$ Ln^{2+} ions.

Solid State Precedent for $4f^n5d^1$ Character in Nd^{2+} and Dy^{2+} Complexes. In 1976, a high pressure study of NdI_2 indicated that the pseudo-alkaline-earth SrI_2 structure of this compound consistent with the salt, $Nd^{2+}(I^{1-})_2$, changed with pressure to give a structure like the $Ln^{3+}(I^{1-})_2(e^{1-})$ structures found for La, Ce, and Pr.[89] This was interpreted as a crossover from a $4f^4$ to a $4f^35d^1$ configuration for the Nd^{2+} ion under pressure. This constitutes a solid state precedent for the molecular example of **2-Nd** that shows the variable nature of the electron configuration of Nd^{2+} depending on the coordination environment.

Another interesting solid state structure involving Nd was the complex $[(C_5H_2{}^tBu_3)_2Nd(\mu\text{-}I)K(18\text{-crown-}6)]$.[14] This Nd^{2+} complex had a solid state structure with the Nd−(ring centroid) distance only 0.05 Å larger than that in $(C_5H_2{}^tBu_3)_2Nd(\mu\text{-}Cl)AlMe_3$,[90] the closest example cited for comparison. This 0.05 Å distance was the smallest increase of bond distances in a Nd^{3+} complex vs a Nd^{2+} complex observed to date for traditional Ln^{2+} complexes and seemed strange. In light of the structure of **2-Nd**, this may suggest that this is related to the variable character of Nd^{2+} electron configurations depending on coordination environment. This difference taken with the somewhat smaller than expected difference of **2-Tm** vs **1-Tm**, namely, 0.12 Å, may be indications of a continuum of bond distances in Ln^{2+} complexes that have $4f^{n+1}$ and $4f^n5d^1$ configurations of similar energy.

When this $[(C_5H_2{}^tBu_3)_2Nd(\mu\text{-}I)K(18\text{-crown-}6)]$ complex was published, its structural parameters were compared[14] favorably with the Dy^{2+} complexes $[(C_5H_2{}^tBu_3)_2Dy(\mu\text{-}X)K(18\text{-crown-}6)]$, where X = Br and BH_4.[13] We examined the metal−(ring centroid) distances for these Dy^{2+} structures compared to their Dy^{3+} analogs and found that these two pairs also show a very small difference. The difference in Ln−(ring centroid) distance for $[(C_5H_2{}^tBu_3)_2Dy(\mu\text{-}Br)K(18\text{-crown-}6)]$ vs $(C_5H_2{}^tBu_3)_2DyBr$ is 0.038 Å, and the difference between $[(C_5H_2{}^tBu_3)_2Dy(\mu\text{-}BH_4)K(18\text{-crown-}6)]$ and $(C_5H_2{}^tBu_3)_2Dy(BH_4)$ is 0.01 Å.[13] Hence, the $[(C_5H_2{}^tBu_3)_2Dy(\mu\text{-}X)K(18\text{-crown-}6)]$ complexes also provide precedent for Ln^{2+} complexes whose Ln−(ring centroid) distances are not much larger than those of the Ln^{3+} analogs. It seems possible that these Dy^{2+} complexes could also have $4f^95d^1$ configurations rather than $4f^{10}$ and constitute more examples that Dy is a crossover metal in this regard.

DOI: 10.1021/ja510831n
J. Am. Chem. Soc. 2015, 137, 369−382

Solid State Data on Ln^{2+} Ions in Alkaline Earth Halide Matrices. The molecular data reported here can also be compared with spectroscopic and magnetic data on solids in which Ln^{3+} ions were doped into MX_2 hosts (M = Ca, Sr, Ba; X = F, Cl) and irradiated with γ radiation from a ^{60}Co source at 77 K. The data were analyzed as arising from Ln^{2+} ions trapped in a crystalline cubic lattice of halide ions.[76,91−94] The spectroscopic data supported $4f^{n+1}$ ground states for the Ln^{2+} ions except for Gd^{2+} that "probably has f^7d for its ground configuration" and Ce^{2+} and Tb^{2+} that were considered "borderline" cases.[94] For La^{2+}, a $5d^1$ configuration was considered likely.[94,95] These results are consistent with the fact that La, Ce, Gd, and Tb have the lowest $4f^{n+1}$ to $4f^n5d^1$ promotional energies (see below). Additional spectroscopic and paramagnetic resonance data on Ho^{2+} generated under these conditions were also interpreted in terms of a $4f^{11}$ configuration.[91,92] A later study of Ce^{2+} showed data consistent with a $4f^15d^1$ ground state.[93] Subsequent analysis of the La, Ce, Gd, Tb, Lu, and Y results interpreted the data based on a model of "two electrons trapped by a trivalent-rare-earth fluorine-vacancy nearest neighbor complex."[96]

These data provide further support that the ligand field environment can affect the ground state electronic configuration of the Ln^{2+} ions. Since the ligand field splitting in a cubic environment lowers two d orbitals rather than a single d orbital as found for d_{z^2} in the trigonal environment of the $(Cp'_3)^{1-}$ ligand set, the d orbital stabilization may not be sufficient to make d orbital population energetically competitive with f orbital population. Hence, the trapped Ln^{2+} ions adopt the traditional $4f^{n+1}$ configuration in this cubic coordination environment.

DFT Calculations. The DFT calculations support the overall view that the +2 ions of Eu, Yb, Sm, and Tm in the molecular complexes **2** are different from the +2 ions of La, Ce, Pr, Gd, Tb, Ho, Er, Y, and Lu in **2** and that Dy and Nd are intermediate and could align with either group. Calculations on the complexes of the metals, Ln = La, Pr, Gd, Tb, Ho, Er, Y, and Lu, indicate the LUMOs for **1** and the HOMOs for **2** are primarily $5d_{z^2}$ ($4d_{z^2}$ for Y). In contrast, for Eu, Yb, Sm, and Tm, the LUMO for **1** and the HOMO for **2** are both 4f orbitals, with significant ligand character only observed in the LUMO for **1**. Calculations on the differences in Ln−(Cp′ centroid) distances between **1** and **2** and the UV−vis spectra for these two sets of ions fit their respective ground states.

For the two intermediate cases, Dy and Nd, the calculations indicate a near degeneracy of the $4f^{n+1}$ and $4f^n5d^1$ configurations. For such multi-reference states, the present semi-local DFT methodology cannot be expected to be accurate. In the case of Nd, the f-like LUMO of **1-Nd** does not match the d-like HOMO of **2-Nd**, but the structural difference between these compounds matches experimental data and is consistent with a $4f^35d^1$ ground state. For Dy, the ground state of the minimum energy structure for $[Cp'_3Dy]^{1-}$ does not match the best ground state for estimating the UV−vis spectra. Dy appears to be the element in the **2** series where the two electronic states are closest in energy.

A Continuum between Models. The $4f^{n+1}$ and $4f^n5d^1$ models are two extremes of a simple single electron approximation model that does not fully describe the actual electronic state in **2**. The HOMO of **2-Nd** shown in Figure 7 provides a pictorial example of this in that it has components that look both d-like and f-like. It was noted above that the differences in Ln−(Cp′ centroid) distances between **1** and **2** for the set of four decrease in the order of their Ln^{3+}/Ln^{2+} reduction potentials: Eu, 0.156 Å, −0.35 V; Yb, 0.143 Å, −1.15 V; Sm, 0.149 Å, −1.55 V; Tm, 0.123 Å, −2.3 V.[17] The smaller difference for Tm may reflect an actual electronic state that involves a blending of both electronic extremes. The fact that Dy and Nd may be "crossover" elements that can adopt either electronic state depending on the ligand set may explain the small 0.01−0.05 Å differences between the Ln−(Cp^{ttt} centroid) distances of $[(C_5H_2{}^tBu_3)_2Nd(\mu\text{-}I)K(18\text{-crown-}6)]$[14] and $[(C_5H_2{}^tBu_3)_2Dy(\mu\text{-}X)K(18\text{-crown-}6)]$ (X = Br, BH_4)[13] and their Ln^{3+} analogs. The Nd^{2+} and Dy^{2+} ions in these complexes may have considerable $4f^n5d^1$ character.

The $4f^{n+1}$ to $4f^n5d^1$ promotion energies for free Ln^{2+} ions[86] can provide information about the relative accessibility of the 5d orbitals from metal to metal. In Figure 11, the $4f^{n+1}$ to $4f^n5d^1$ promotion energies are plotted against the differences in Ln−(Cp′ centroid) distance between **1** and **2**. This is a crude diagram, but it can be used to raise some questions regarding Ln^{2+} ions.

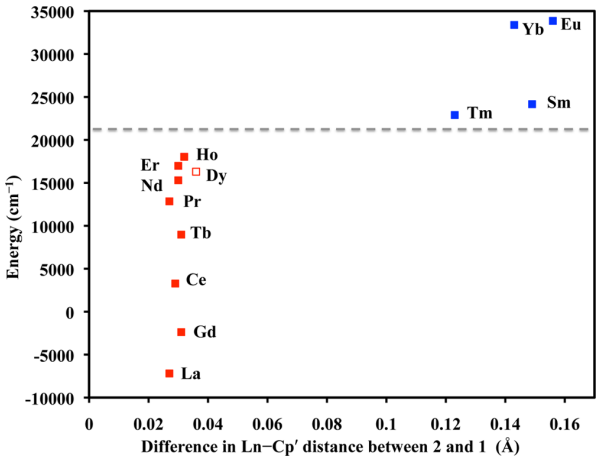

Figure 11. Plot of the $4f^{n+1}$ to $4f^n5d^1$ promotion energies (only an estimated energy is available for Dy) vs the differences in Ln−(Cp′ centroid) distances of **2** and **1**.[86] The gray dashed line indicates the barrier in promotion energies to reduce the $4f^n$ Cp'_3Ln to a $4f^{n+1}$ (blue squares on right) or $4f^n5d^1$ (red squares on left) configuration of $[Cp'_3Ln]^{1-}$.

The gray dotted line above 20 000 cm^{-1} suggests there is a threshold energy level that allows the $4f^n5d^1$ configuration to be the ground state. This presumably relates to the amount of crystal field stabilization that is accessible from the $(Cp'_3)^{3-}$ ligand set in **2**. When a crystal field can stabilize a d orbital to this extent, formation of a $4f^n5d^1$ +2 ion should be possible. We are actively searching for other coordination geometries that will do that. The plot also suggests that if a ligand field could provide slightly more d orbital stabilization than found with the $(Cp'_3)^{3-}$ ligand set, Tm and Sm might also form $4f^n5d^1$ +2 ions.

This plot also shows the similarities in promotion energies between Ho and Er and Nd and Dy. The positions of Dy and Nd near the dotted line can explain why they are crossover elements that can form both $4f^{n+1}$ and $4f^n5d^1$ divalent ions. However, the similar energies of Ho and Er might suggest they could also form $4f^{n+1}$ +2 ions if promotion energy were the only factor involved. The fact that $4f^{n+1}$ complexes of Ho^{2+} and

DOI: 10.1021/ja510831n
J. Am. Chem. Soc. 2015, 137, 369−382

Er^{2+} have not been identified in solution suggests that more factors are involved and this is too simplistic a view.

CONCLUSION

Direct comparison of the +3 and +2 ions of all the lanthanides (except Pm, which was not studied because of its radioactivity) in a single uniform coordination environment is now possible for the first time with the complexes, Cp'_3Ln, **1**, and $[K(2.2.2\text{-cryptand})][Cp'_3Ln]$, **2**, respectively. This allows comparison of the properties of **2** for the traditional six Ln^{2+} ions, Eu^{2+}, Yb^{2+}, Sm^{2+}, Tm^{2+}, Dy^{2+}, and Nd^{2+}, long known in solid state and solution chemistry with the properties of **2** with the new nine ions La^{2+}, Ce^{2+}, Pr^{2+}, Gd^{2+}, Tb^{2+}, Y^{2+}, Ho^{2+}, Er^{2+}, and Lu^{2+} recently discovered in molecular complexes via Schemes 1 and 2. The results indicate that the former grouping of the six traditional +2 ions with $4f^{n+1}$ ground states and the new nine +2 ions with $4f^n5d^1$ ground states should be modified. In the $(Cp'_3)^{3-}$ coordination environment of **2**, Dy^{2+} and Nd^{2+} have properties consistent with $4f^n5d^1$ ground states. In **2**, only four of the elements traditionally known to form +2 ions, namely, Eu, Yb, Sm, and Tm, have structural and spectroscopic properties consistent with $4f^{n+1}$ ground states. Hence, at this point we can identify three categories of Ln^{2+} ions: one group that forms traditional $4f^{n+1}$ ions, a second group that forms $4f^n5d^1$ ions, and a third group of metals that can cross over between configurations depending on the coordination environment. In the coordination environment of **2**, the first class has four members, Eu, Yb, Sm, and Tm, the second class has nine members, La, Ce, Pr, Gd, Tb, Ho, Y, Er, and Lu, and the third class has two, Dy and Nd. In other coordination environments, the numbers in each class may be different depending on the effect of the ligand field on d orbital availability. It is also possible that other categories are yet to be found.

DFT calculations on **1** and **2** are consistent with this analysis. The properties of the traditional set of four as well as the set of nine are well matched by the calculations. The problematic nature of the calculations on the crossover ions, Dy^{2+} and Nd^{2+}, is consistent with the presence of two electronic states that are close in energy for each ion. These metals could adopt either configuration depending on subtle differences in the coordination environment.

The 4f−5d promotion energies of the Ln^{2+} ions are also consistent with these three sets of Ln^{2+} ions. The four traditional divalent ions have the highest promotion energies and the new nine ions the lowest. Dy and Nd have promotion energies at the borderline between these two other sets. Since Tm, Er, Ho, Dy, and Nd all have promotion energies at the borderline, further studies of Ln^{2+} complexes should evaluate data with the possibility that either electron configuration could be present.

More generally, these results show that the ligand set can change the ground electronic state in Ln^{2+} complexes. This has not been observed with Ln^{3+} complexes where the limited radial extension of the 4f orbitals leads to minimal interaction with the ligand set and where the 5d orbitals are too high in energy to contribute significantly. For the +2 ions, the 5d orbitals are lower in energy. Apparently, with complexes of the Ln^{2+} ions, the proper ligand field can lower the energy of the 5d orbitals with respect to the 4f orbitals such that 5d can be part of the ground state. The trigonal environment of the $(Cp'_3)^{3-}$ ligand set is ideal for this purpose, since a single d orbital is stabilized.

In these special ligand fields, the $4f^n5d^1$ configuration is more accessible than the $4f^{n+1}$ ground state for most of the lanthanides so that reduction of Ln^{3+} to Ln^{2+} is possible with potassium. The Ln^{3+}/Ln^{2+} redox potentials calculated for $4f^n$ Ln^{3+} to $4f^{n+1}$ Ln^{2+} reduction, Table 1, do not apply in the ligand environments that stabilize the 5d orbitals. It will be interesting to determine the range of ligand environments that will stabilize the 5d orbitals and if the accessibility of the 5d orbitals will allow isolation of complexes of Ln^{1+}.

ASSOCIATED CONTENT

Supporting Information

Additional computational details, spectroscopic information, crystallographic data collection, structure solution, and refinement (PDF); X-ray diffraction details of compounds **2-La** (CCDC no. 1025259), **2-Ce** (1025260), **2-Nd** (1025261), **1-Sm** (1025315), **2-Sm** (1025262), **1-Eu** (1025316), **2-Eu** (1025374), **1-Dy** (1025317), **2-Dy** (1025375), **1-Tm** (1025318), **2-Tm** (1025376), **1-Yb** (1025319), and **2-Yb** (1025377) (CIF); and DFT-optimized structural coordinates for **1-Nd**, **1-Sm**, **1-Eu**, **1-Dy**, **1-Tm**, **1-Yb**, and the anions in **2-Nd**, **2-Sm**, **2-Eu**, **2-Dy**, **2-Tm**, and **2-Yb** (XYZ). This material is available free of charge via the Internet at http://pubs.acs.org.

AUTHOR INFORMATION

Corresponding Authors

filipp.furche@uci.edu
wevans@uci.edu

Notes

The authors declare no competing financial interest.

ACKNOWLEDGMENTS

We thank the U.S. National Science Foundation for support of this research under Grant CHE-1265396 (W.J.E.) and Grant CHE-1213382 (F.F.), as well as Professor A. S. Borovik for assistance with EPR and UV−vis spectroscopy and Dr. Norman Edelstein for helpful discussions.

REFERENCES

(1) Meyer, G. In *The Rare Earth Elements: Fundamentals and Applications*; Atwood, D. A., Ed.; Wiley: Chichester, U.K., 2012.
(2) Matignon, C.; Cazes, E. C. *Ann. Chim. Phys.* **1906**, *8*, 417−426.
(3) Jantsch, G.; Skalla, N. *Z. Anorg. Allg. Chem.* **1929**, *185*, 49−64.
(4) Klemm, W.; Bommer, H. *Z. Anorg. Allg. Chem.* **1937**, *231*, 138−171.
(5) Corbett, J. D. *Rev. Chim. Miner.* **1972**, *10*, 289.
(6) Meyer, G. *Chem. Rev.* **1988**, *88*, 93−107.
(7) Meyer, G. *Z. Anorg. Allg. Chem.* **2007**, *633*, 2537−2552.
(8) Bochkarev, M. N.; Fedushkin, I. L.; Fagin, A. A.; Petrovskaya, T. V.; Ziller, J. W.; Broomhall-Dillard, R. N. R.; Evans, W. J. *Angew. Chem., Int. Ed. Engl.* **1997**, *36*, 133−135.
(9) Evans, W. J.; Allen, N. T.; Ziller, J. W. *J. Am. Chem. Soc.* **2000**, *122*, 11749−11750.
(10) Bochkarev, M. N.; Fedushkin, I. L.; Dechert, S.; Fagin, A. A.; Schumann, H. *Angew. Chem., Int. Ed.* **2001**, *40*, 3176−3178.
(11) Evans, W. J. *Coord. Chem. Rev.* **2000**, *206*, 263−283.
(12) Evans, W. J. *Inorg. Chem.* **2007**, *46*, 3435−3449.
(13) Jaroschik, F.; Nief, F.; Le Goff, X.-F.; Ricard, L. *Organometallics* **2007**, *26*, 1123−1125.
(14) Jaroschik, F.; Momin, A.; Nief, F.; Le Goff, X.-F.; Deacon, G. B.; Junk, P. C. *Angew. Chem., Int. Ed.* **2009**, *48*, 1117−1121.
(15) Meyer, G.; Meyer, H.-J. *Chem. Mater.* **1992**, *4*, 1157−1168.
(16) Meyer, G.; Wickleder, M. S. *Handbook on the Physics and Chemistry of Rare Earths*; Elsevier Science B. V.: Amsterdam, 2000; Vol. *28*.

DOI: 10.1021/ja510831n
J. Am. Chem. Soc. 2015, 137, 369−382

(17) Morss, L. R. *Chem. Rev.* **1976**, *76*, 827−841.
(18) Bochkarev, M. N. *Coord. Chem. Rev.* **2004**, *248*, 835−851 and references therein.
(19) Nief, F. *Dalton Trans.* **2010**, *39*, 6589−6598 and references therein.
(20) Corbett, J. D. *Rev. Chim. Miner.* **1973**, *10*, 239−257.
(21) Meyer, G. *Angew. Chem., Int. Ed.* **2008**, *47*, 4962−4964.
(22) Mikheev, N. B.; Auerman, L. N.; Rumer, I. A.; Kamenskaya, A. N.; Kazakevich, M. Z. *Russ. Chem. Rev.* **1992**, *61*, 1805.
(23) Connelly, N. G.; Geiger, W. E. *Chem. Rev.* **1996**, *96*, 877−910.
(24) Gun'ko, Y. K.; Hitchcock, P. B.; Lappert, M. F. *J. Organomet. Chem.* **1995**, *499*, 213−219.
(25) Al-Juaid, S.; Gun'ko, Y. K.; Hitchcock, P. B.; Lappert, M. F.; Tian, S. J. *J. Organomet. Chem.* **1999**, *582*, 143−152.
(26) Bochkarev, M. N.; Fagin, A. A. *Chem.—Eur. J.* **1999**, *5*, 2990−2992.
(27) Hitchcock, P. B.; Lappert, M. F.; Tian, S. *Organometallics* **2000**, *19*, 3420−3428.
(28) Evans, W. J.; Allen, N. T.; Ziller, J. W. *Angew. Chem., Int. Ed.* **2002**, *41*, 359−361.
(29) Nief, F.; Turcitu, D.; Ricard, L. *Chem. Commun.* **2002**, 1646−1647.
(30) Hitchcock, P. B.; Lappert, M. F.; Maron, L.; Protchenko, A. V. *Angew. Chem., Int. Ed.* **2008**, *47*, 1488−1491.
(31) MacDonald, M. R.; Ziller, J. W.; Evans, W. J. *J. Am. Chem. Soc.* **2011**, *133*, 15914−15917.
(32) MacDonald, M. R.; Bates, J. E.; Fieser, M. E.; Ziller, J. W.; Furche, F.; Evans, W. J. *J. Am. Chem. Soc.* **2012**, *134*, 8420−8423.
(33) MacDonald, M. R.; Bates, J. E.; Ziller, J. W.; Furche, F.; Evans, W. J. *J. Am. Chem. Soc.* **2013**, *135*, 9857−9868.
(34) Evans, W. J.; Foster, S. E. *J. Organomet. Chem.* **1992**, *433*, 79−94.
(35) Gun'ko, Y. K.; Hitchcock, P. B.; Lappert, M. F. *Chem. Commun.* **1998**, 1843−1844.
(36) Huebner, L.; Kornienko, A.; Emge, T. J.; Brennan, J. G. *Inorg. Chem.* **2004**, *43*, 5659−5664.
(37) Shannon, R. D. *Acta Crystallogr., Sect. A* **1976**, *32*, 751−767.
(38) Evans, W. J.; Grate, J. W.; Choi, H. W.; Bloom, I.; Hunter, W. E.; Atwood, J. L. *J. Am. Chem. Soc.* **1985**, *107*, 941−946.
(39) Evans, W. J.; Ulibarri, T. A.; Chamberlain, L. R.; Ziller, J. W.; Alvarez, D. J. *Organometallics* **1990**, *9*, 2124−2130.
(40) Evans, W. J.; Keyer, R. A.; Ziller, J. W. *J. Organomet. Chem.* **1990**, *394*, 87−97.
(41) For example, Cp_2TiCl_2 (Clearfield, A.; Warner, D. K.; Saldarriaga-Molina, C. H.; Ropal, R.; Bernal, I. *Can. J. Chem.* **1975**, *53*, 1622−1629) and $[Cp_2Ti(\mu\text{-}Cl)]_2$ (Jungst, R.; Sekutowski, D.; Davis, J.; Luly, M.; Stucky, G. *Inorg. Chem.* **1977**, *16*, 1645−1655) have average C(η^5-Cp) bond lengths of 2.370 and 2.350 Å, respectively. Similarly, Cp_4Zr (Rogers, R. D.; Bynum, R. V.; Atwood, J. L. *J. Am. Chem. Soc.* **1978**, *100*, 5238−5239) and Cp_3Zr (Lukens, W. L., Jr.; Andersen, R. A. *Organometallics***1995**, *14*, 3435−3439) both have the same average Zr−C(η^5-Cp) bond length of 2.58 Å.
(42) Lauher, J. W.; Hoffmann, R. *J. Am. Chem. Soc.* **1976**, *98*, 1729−1742.
(43) Bursten, B. E.; Rhodes, L. F.; Strittmatter, R. J. *J. Am. Chem. Soc.* **1989**, *111*, 2758−2766.
(44) Bursten, B. E.; Rhodes, L. F.; Strittmatter, R. J. *J. Am. Chem. Soc.* **1989**, *111*, 2756−2758.
(45) Strittmatter, R. J.; Bursten, B. E. *J. Am. Chem. Soc.* **1991**, *113*, 552−559.
(46) Denning, R. G.; Harmer, J.; Green, J. C.; Irwin, M. *J. Am. Chem. Soc.* **2011**, *133*, 20644−20660.
(47) Lukens, W. W., Jr.; Andersen, R. A. *Organometallics* **1995**, *14*, 3435−3439.
(48) Taylor, M. D. *Chem. Rev.* **1962**, *62*, 503−511.
(49) Girard, P.; Namy, J. L.; Kagan, H. B. *J. Am. Chem. Soc.* **1980**, *102*, 2693−2698.
(50) Heckmann, G.; Niemeyer, M. *J. Am. Chem. Soc.* **2000**, *122*, 4227−4228.
(51) Izod, K.; Liddle, S. T.; Clegg, W. *Inorg. Chem.* **2004**, *43*, 214−218.
(52) Bergbreiter, D. E.; Killough, J. M. *J. Am. Chem. Soc.* **1978**, *100*, 2126−2134.
(53) Jordan, R. F.; Echols, S. F. *Inorg. Chem.* **1987**, *26*, 383−386.
(54) Peterson, J. K.; MacDonald, M. R.; Ziller, J. W.; Evans, W. J. *Organometallics* **2013**, *32*, 2625−2631.
(55) Stults, S. D.; Andersen, R. A.; Zalkin, A. *Organometallics* **1990**, *9*, 115−122.
(56) Krinsky, J. L.; Minasian, S. G.; Arnold, J. *Inorg. Chem.* **2011**, *50*, 345−357.
(57) Minasian, S. G.; Krinsky, J. L.; Rinehart, J. D.; Copping, R.; Tyliszczak, T.; Janousch, M.; Shuh, D. K.; Arnold, J. *J. Am. Chem. Soc.* **2009**, *131*, 13767−13783.
(58) Lappert, M. F.; Yarrow, P. I. W.; Atwood, J. L.; Shakir, R.; Holton, J. *J. Chem. Soc., Chem. Commun.* **1980**, 987−988.
(59) Staroverov, V. N.; Scuseria, G. E.; Tao, J.; Perdew, J. P. *J. Chem. Phys.* **2003**, *119*, 12129−12137.
(60) Bates, J. E.; Furche, F. *J. Chem. Phys.* **2012**, *137*, 164105/1−16105/10.
(61) *TURBOMOLE*, version 6.5; TURBOMOLE GmbH: Karlsruhe, Germany, 2013; http://www.turbomole.com.
(62) Cao, X.; Dolg, M. *J. Mol. Struct.: THEOCHEM* **2002**, *581*, 139−147.
(63) Weigend, F.; Ahlrichs, R. *Phys. Chem. Chem. Phys.* **2005**, *7*, 3297−3305.
(64) Rappoport, D.; Furche, F. *J. Chem. Phys.* **2010**, *133*, 134105/1−134105/11.
(65) Klamt, A.; Schueuermann, G. *J. Chem. Soc., Perkin Trans. 2* **1993**, 799−805.
(66) *CRC Handbook of Chemistry and Physics*, 81st ed.; Lide, D. R., Ed.; CRC Press: Boca Raton, FL, 2008; Chapter 8, p 136.
(67) Bauernschmitt, R.; Ahlrichs, R. *Chem. Phys. Lett.* **1996**, *256*, 454−464.
(68) Tilley, T. D.; Anderson, R. A.; Spencer, B.; Ruben, H.; Zalkin, A.; Templeton, D. H. *Inorg. Chem.* **1980**, *19*, 2999−3003.
(69) Spirlet, M.-R.; Goffart, J. *J. Organomet. Chem.* **1995**, *493*, 149−151.
(70) Cassani, M. C.; Lappert, M. F.; Laschi, F. *Chem. Commun.* **1997**, 1563−1564.
(71) Kot, W. K.; Shalimoff, G. V.; Edelstein, N. M.; Edelman, M. A.; Lappert, M. F. *J. Am. Chem. Soc.* **1988**, *110*, 986−987.
(72) Blake, P. C.; Edelstein, N. M.; Hitchcock, P. B.; Kot, W. K.; Lappert, M. F.; Shalimoff, G. V.; Tian, S. *J. Organomet. Chem.* **2001**, *636*, 124−129.
(73) Walensky, J. R.; Martin, R. L.; Ziller, J. W.; Evans, W. J. *Inorg. Chem.* **2010**, *49*, 10007−10012.
(74) Parry, J. S.; Geoffrey, G. L.; Coles, S. J.; Hursthouse, M. B. *J. Am. Chem. Soc.* **1999**, *121*, 6867−6871.
(75) Siladke, N. A.; Webster, C. L.; Walensky, J. R.; Takase, M. K.; Ziller, J. W.; Grant, D. J.; Gagliardi, L.; Evans, W. J. *Organometallics* **2013**, *32*, 6522−6531.
(76) Dieke, G. H.; Crosswhite, H. M.; Crosswhite, H. *Spectra and Energy Levels of Rare Earth Ions in Crystals*; Interscience Publishers: New York, 1968.
(77) Emeléus, H. J.; Sharpe, A. G. *Modern Aspects of Inorganic Chemistry*; Routledge & Kegan Paul: London, 1973; Vol. 4.
(78) Bünzli, J. C. G.; Choppin, G. R. *Lanthanide Probes in Life, Chemical, And Earth Sciences: Theory and Practice*; Elsevier: Amsterdam, 1989.
(79) Cotton, S. *Lanthanide and Actinide Chemistry*; Wiley: Chichester, U.K., 2006.
(80) Atwood, D. A. *The Rare Earth Elements: Fundamentals and Applications*; Wiley: Chichester, U.K., 2012.
(81) Evans, W. J.; Hozbor, M. A. *J. Organomet. Chem.* **1987**, *326*, 299−306.
(82) Evans, W. J.; Broomhall-Dillard, R. N. R.; Ziller, J. W. *Polyhedron* **1998**, *17*, 3361−3370.

DOI: 10.1021/ja510831n
J. Am. Chem. Soc. 2015, 137, 369−382

(83) Nava, P.; Sierka, M.; Ahlrichs, R. *Phys. Chem. Chem. Phys.* **2003**, *5*, 3372−3381.
(84) Mulliken, R. S. *J. Chem. Phys.* **1955**, *23*, 1833−1840.
(85) For unknown reasons, the calculation on Sm was more difficult and a corresponding value for Sm was not obtained. The calculation for Yb used def2-SVP, while the calculations for Eu and Tm used def2-SVPD basis sets.
(86) Dorenbos, P. *J. Phys.: Condens. Matter* **2003**, *15*, 575−594.
(87) Seitz, M.; Oliver, A. G.; Raymond, K. N. *J. Am. Chem. Soc.* **2007**, *129*, 11153−11160 and references therein.
(88) Quadrelli, E. A. *Inorg. Chem.* **2002**, *41*, 167−169.
(89) Beck, H. P. *Z. Naturforsch.* **1976**, *31b*, 1548−1549.
(90) Walter, M. D.; Bentz, D.; Weber, F.; Schmitt, O.; Wolmershäuser, G.; Sitzmann, H. *New J. Chem.* **2007**, *31*, 305−318.
(91) Sabisky, E. S. *Phys. Rev.* **1966**, *141*, 352−362.
(92) Weakliem, H. A.; Kiss, Z. J. *Phys. Rev.* **1967**, *157*, 277−290.
(93) Alig, R. C.; Kiss, Z. J.; Brown, J. P.; McClure, D. S. *Phys. Rev.* **1969**, *186*, 276−284.
(94) McClure, D. S.; Kiss, Z. J. *J. Chem. Phys.* **1963**, *39*, 3251−3257.
(95) O'Connor, J. R.; Chen, J. H. *Bull. Am. Phys. Soc.* **1963**, *8*, 231.
(96) Staebler, D. L.; Schnatterly, S. E. *Phys. Rev. B* **1971**, *3*, 516−526.

DOI: 10.1021/ja510831n
J. Am. Chem. Soc. 2015, 137, 369−382

Chapter 7

Unusual behavior of Group V d^0 transition metals

This chapter provides an introduction to work done in collaboration with the Heyduk group at UCI. The work was published in Dalton Transactions in late 2014. Reproduced from Ref. S. Hananouchi, B.T. Krull, J.W. Ziller, F. Furche, and A.F. Heyduk, "Metal effects on ligand non-innocence in Group 5 complexes of the redox-active [ONO] pincer ligand," *Dalton Transactions* **43**, 17991 (2014) with permission from the Royal Society of Chemistry.

Small-molecule activation via multi-electron transfer is at the heart of many important chemical transformations including widely used industrial processes such as nitrogen fixation.[194] The most effective catalysts rely on the rarest of metals, e.g. platinum, iridium, or rhodium. These metals are effective catalysts because they promote the transfer of pairs of, rather than single, electrons.[195] Because of the scarcity of such metals, however, there is considerable interest in the development of efficient catalysts based on cheaper, more earth-abundant materials as a way to make larger-scale uses more feasible. Early transition metals are cheaply available and are widely used in metathesis pathways[196,197] but tend to promote one-electron processes, which are difficult to control and are prone to degradation.[195] Recent revival in the use of early transition metals in bond-activation has been due to a deeper understanding of their electronic structure and how it can be exploited.

Redox active ligands provide a route to bring reactivity to transition metals who were once thought to be relatively poorly catalysts. Redox active ligands can exist in multiple oxidation states that are accessible by chemical and electrical means and have frontier orbitals energetically lower than the d manifold of the metal center.[198,199] The first appearance of redox active ligands can be traced back to the 1960's where complexes of divalent metals such as copper and nickel could be oxidized at the ligand without perturbing the metal center.[200,201] More recent studies showed that tetrahedral zirconium complexes using redox active ligands were able to facilitate nitrene transfer with moderate success, despite their formally d^0 electronic structure.[202] This is due to the strong interaction between metal and ligand, where the electron addition or removal process can take place at the ligand but is mediated by the empty d manifold of the metal center. The bonding nature of complexes containing redox active ligands is generally difficult to describe using only experimental techniques and computational tools have been increasingly important for their elucidation.[203,204]

The focus of this work is to understand the interplay between group V transition metals vanadium, niobium, and tantalum, and the redox active ligand ONO. The ONO ligand ($ONOH_3$

= bis(3,5-di-*t*ert-butyl-2-phenol)amine, Figure 7.1) is a tri-dentate tri-anionic ligand that is known to exist in three oxidation states, the quinone (-1), semi-quinone (-2), and catecholate (-3) forms. The ligand binds the transition metal center in a facial orientation and has also been shown to act as a bridge between two metal centers.[202,205] Group V transition metals were chosen because of their strong electron deficiency which is compatible with the tri-anionic ONO ligand, and their previously demonstrated inclination towards the promotion of four-electron processes.[202] Density functional theory (DFT) and its linear-response extension, time-dependent DFT (TDDFT) were used to study the ground-state structures and simulate UV-vis spectra, respectively, of [ONO]MCl_2L (M = V, L = THF; M = Nb, Ta, L = Et_2O) and the one-electron oxidized analogs [ONO]MCl_3 (M = V, Nb, Ta). The computed metrical parameters for the different species were in good agreement with the experimentally observed ones. Qualitatively, the UV-vis spectra were also in good agreement with experimental results. While niobium and tantalum are both well described by a +5 oxidation state, closed-shell d^0 electronic structure, complexes of vanadium were more stable in the d^1 configuration, or +4 oxidation state, due to the contracted nature of the $3d$ orbitals. EPR measurements suggesting an open-shell singlet diradical was corroborated by spin-symmetry broken DFT calculations that lead to a lower energy minimum for the open-shell singlet solution compared to the closed-shell singlet solution like that in Nb and Ta. Despite the d^1 configuration of the vanadium complexes, their reactivity was similar to that of their niobium and tantalum analogs.

Dalton Transactions

PAPER

View Article Online
View Journal | View Issue

Cite this: *Dalton Trans.*, 2014, **43**, 17991

Metal effects on ligand non-innocence in Group 5 complexes of the redox-active [ONO] pincer ligand†

Steven Hananouchi, Brandon T. Krull, Joseph W. Ziller, Filipp Furche* and Alan F. Heyduk*

Received 24th July 2014,
Accepted 13th October 2014

DOI: 10.1039/c4dt02259a

www.rsc.org/dalton

Isostructural vanadium, niobium and tantalum complexes of bis(3,5-di-*tert*-butyl-2-phenol)amine ([ONO]H_3), were prepared and characterized to evaluate the impact of the metal ion on redox-activity of the ligand platform. New vanadium and niobium complexes with the general formula, [ONO]MCl_2L (M = V, L = THF, **1-V**; M = Nb, L = Et_2O, **1-Nb**) were prepared and structurally analysed by X-ray crystallography. The solid-state structures indicate that the niobium derivative is electronically analogous to the tantalum analog **1-Ta**, containing a reduced (ONO) ligand and a niobium(V) metal ion, [ONO^{cat}]$Nb^{V}Cl_2(OEt_2)$; whereas, the vanadium derivative is best described as a vanadium(IV) complex, [ONO^{sq}]$V^{IV}Cl_2$(THF). One-electron oxidation was carried out on all three metal complexes to afford [ONO]MCl_3 derivatives (**3-V**, **3-Nb**, **3-Ta**). For all three derivatives, oxidation occurs at the (ONO) ligand. In the cases of niobium and tantalum, electronically similar complexes characterized as [ONO^{sq}]$M^{V}Cl_3$ were obtained and for vanadium, ligand-based oxidation led to the formation of a complex best described as [ONO^{q}]$V^{IV}Cl_3$. All complexes were characterized by spectroscopic and electrochemical methods. DFT and TD-DFT calculations were used to probe the electronic structure of the complexes and help verify the different electronic structures stemming from changes to the coordinated metal ion.

Introduction

The interactions between a transition metal ion and a redox-active ligand are central to the ability of these two entities to work together in a redox reaction. Recently, coordination complexes of redox-active ligands have attracted considerable interest for use in multi-electron small-molecule activation reactions and in redox-based catalytic reactions.[1–4] The ability of the metal and ligand to work together to facilitate such reactivity lies in the sharing or delocalization of ligand-based valence electrons onto the coordinated transition metal.[5] The delocalization of the ligand-based electron pair is determined by the spatial overlap of the ligand and metal frontier orbitals as well as by the relative energies of these orbitals. Previous studies of electron delocalization have focused on bipyridyl ruthenium complexes containing one or more catecholate-type ligands and have elucidated the effect of ligand donor atom in the degree of delocalization.[6] Studies of $[ML_2]^n$ (M = Ni^{II}, Pd^{II}, Pt^{II}; L = phenylenediamine-type ligand; n = −2, −1, 0, +1, +2) also have been conducted.[7–10] While these latter studies provided insight into communication between the two redox-active ligands, the large ligand-field stabilization energies (LFSEs) associated with the square-planar d^8 metal center precluded significant changes in the distribution of electrons between the ligands and the metal. For early transition metal complexes with low d electron counts and small LFSEs, we might expect significant changes in the distribution of valence electrons between the metal and ligand for isostructural members of a metal period. Structural, spectroscopic, and computational studies could then be used to highlight the influence of the metal ion on the electronic properties of a complex with a redox-active ligand.

In order to elucidate electronic properties in a coordination complex as a function of the metal ion, a series of isostructural and isoelectronic metal complexes were targeted in which the electronic properties could be interrogated both experimentally and theoretically. We have previously prepared tantalum complexes containing the redox-active (ONO) ligand platform ((ONO^{cat})H_3 = bis(3,5-di-*tert*-butyl-2-phenol)amine) in all three ligand oxidation states summarized in Fig. 1.[2,11]

Department of Chemistry, 1102 Natural Sciences 2, University of California, Irvine, CA 92697-2025, USA. E-mail: aheyduk@uci.edu, filipp.furche@uci.edu

† Electronic supplementary information (ESI) available: ^{1}H NMR spectra for **1-V**, **1-Nb**, [$BnNEt_3$][**2-V**] and [$BnNEt_3$][**2-Nb**]. Cyclic voltammograms for [$BnNEt_3$][**2-M**] (M = V, Nb, Ta). Computational and crystallographic data for all reported complexes. CCDC 1015033–1015036. For ESI and crystallographic data in CIF or other electronic format see DOI: 10.1039/c4dt02259a

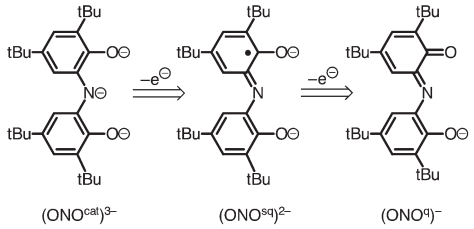

Fig. 1 Oxidation states of the (ONO) ligand platform.

Notably the electronic structure of the $S = 1/2$ complex (ONO)$TaCl_3$ could be interrogated by structural, spectroscopic, and electrochemical techniques, providing a concise view of the metal–ligand interaction. This discovery prompted us to pursue analogous niobium and vanadium complexes of the (ONO) ligand platform in order to evaluate how these changes to the central metal ion would influence the overall properties of the redox-active ligand complex.

This paper presents the synthesis of six new (ONO) complexes of niobium and vanadium along with both experimental and theoretical treatments of their electronic structure. In addition to the synthetic challenges associated with the preparation of these complexes, a clear trend in the electronic structural characteristics emerges, with the vanadium complexes showing the strongest non-innocent redox character ultimately leading to ligand-to-metal charge transfer in the ground state electronic structure. The metal–ligand interactions were probed by structural, electronic and EPR spectroscopic, electrochemical and density functional methods.

Results and discussion

Synthesis and characterization of V, Nb, and Ta complexes

Access to (ONO)MCl_2L complexes of vanadium, niobium, and tantalum required different synthetic strategies. As previously reported,[11] the trimethyltantalum complex, $TaMe_3Cl_2$ reacted with $(ONO^{cat})H_3$ to liberate three equivalents of methane and form (ONO)$TaCl_2(OEt_2)$ (**1-Ta**) in reasonably high yields; however, the thermal sensitivity of $TaMe_3Cl_2$ prompted the development of a new route starting from $TaCl_5$. Addition of a dilute solution (less than 1 M) of $(ONO^{cat})Li_3$ in 50 : 1 toluene–ether to a suspension of $TaCl_5$ in toluene gave **1-Ta** as a red powder in quantitative yield after normal workup to remove LiCl. An identical procedure was used to prepare the niobium analog, (ONO)$NbCl_2(OEt_2)$ (**1-Nb**) from $NbCl_5$ as shown in Scheme 1. The niobium product formed as a dark purple powder that was readily characterized by ^{1}H NMR spectroscopy. Resonances were observed at 1.26 and 1.37 ppm for the *tert*-butyl groups of the (ONO) ligand, while the (ONO) ligand aryl resonances were observed at 6.92 and 7.10 ppm. Resonances for a single coordinated diethyl ether molecule were apparent as a triplet at 1.07 ppm and a quartet at 3.54 ppm.

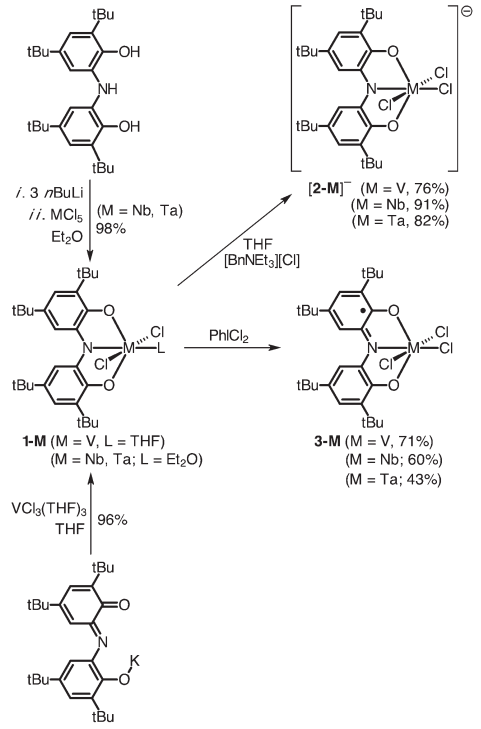

Scheme 1

Synthesis of the vanadium complex, (ONO)VCl_2 (**1-V**), was achieved by a redox pathway using vanadium(III) and the two-electron-oxidized quinonate form of the (ONO) ligand as summarized in Scheme 1. Dropwise addition of a cold solution of $(ONO^q)K$ in THF to a cold solution of $VCl_3(THF)_3$ in THF resulted in a color change from pink to dark purple. Stirring the reaction mixture for 12 h at room temperature afforded **1-V** as a dark purple solid in high yield after workup to remove KCl. The vanadium complex is diamagnetic and showed NMR resonances consistent with those observed for the tantalum and niobium homologues **1-Ta** and **1-Nb**, respectively.

The solid-state molecular structures of **1-V** and **1-Nb** were determined by single-crystal X-ray diffraction experiments both to interrogate gross structural features of the complexes and to elucidate the oxidation state of the (ONO) ligand. Fig. 2 shows an ORTEP diagram of **1-V**; the niobium complex, **1-Nb**, is structurally analogous. Table 1 collects selected metrical parameters for **1-V** and **1-Nb** alongside previously published data for **1-Ta**. All three complexes showed distorted octahedral geometry about the metal center. The (ONO) ligand adopts a meridional coordination geometry in each case along with trans chloride ligands and a single coordinated solvent molecule located trans to the (ONO) nitrogen. The restricted bite angle of the (ONO) ligand results in O–M–O angles that range from 150° for vanadium to 155° for the larger niobium and tantalum metal ions. As expected, the metal–ligand bond lengths are shortest for **1-V**, consistent with the smaller radius of vanadium relative to the heavier Group 5 metals. Within the (ONO) ligands, the C–O and C–N bond distances, typically a

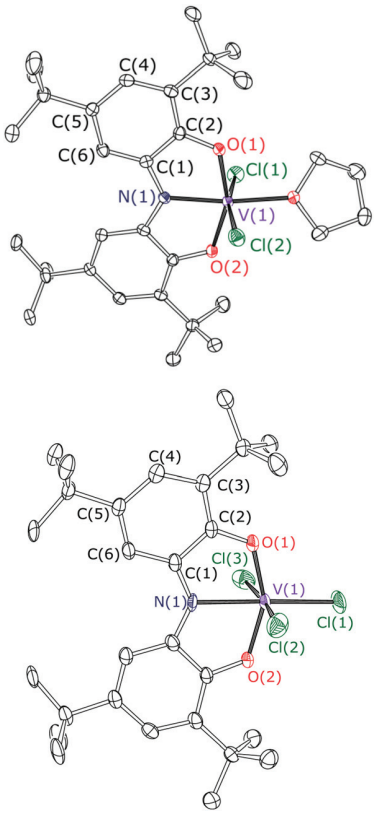

Fig. 2 ORTEP diagrams of (ONO)VCl_2(THF) (**1-V**, *top*) and (ONO)VCl_3 (**3-V**, *bottom*). Thermal ellipsoids are shown at 50% probability. Hydrogen atoms and solvent molecules have been omitted for clarity.

useful metric for assigning ligand oxidation state, are shortest for **1-V** (1.33 Å and 1.39 Å, respectively) and get longer for niobium and tantalum. The C–C bond distances within six-membered rings of the (ONO) ligands are similar across all three structures.

The UV-vis absorption spectra of the **1-M** complexes are dominated by intense absorptions throughout the visible region of the electromagnetic spectrum (Fig. 3). All three complexes show a strong high-energy absorption that is sensitive to the metal with the absorption for **1-V** appearing at 305 nm whereas **1-Nb** and **1-Ta** are blue-shifted to 290 nm and 284 nm, respectively. While **1-Ta** shows a series of shoulders and weaker absorptions from 325 nm to 900 nm, **1-V** and **1-Nb** show well-defined and strong absorptions in the visible region. The niobium complex shows two well defined peaks of unequal intensity at 365 nm and 545 nm while the vanadium complex shows two overlapping, equal-intensity absorptions at 500 and 550 nm alongside a weaker shoulder near 650 nm. These low-energy absorptions in **1-V** are reminiscent of the optical absorptions observed for $V^{IV}[ONO^{sq}]_2$.[12,13]

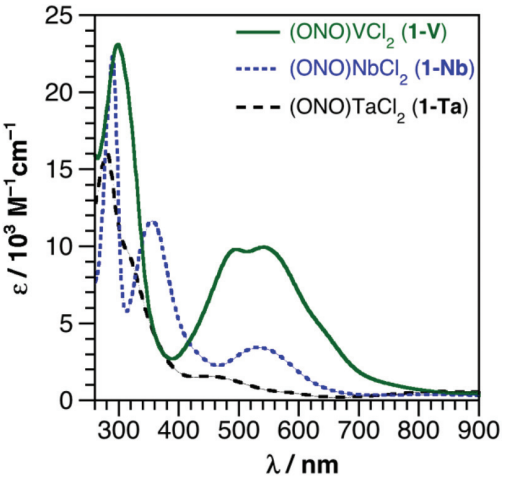

Fig. 3 Electronic absorption spectra of (ONO)VCl_2(THF) (**1-V**), (ONO)-$NbCl_2(OEt_2)$ (**1-Nb**), and (ONO)$TaCl_2(OEt_2)$ (**1-Ta**) in THF.

Table 1 Selected bond lengths (Å) for (ONO)VCl_2(THF)·THF (**1-V**·Et_2O), (ONO)$NbCl_2(OEt_2)$·Et_2O (**1-Nb**·Et_2O), and (ONO)$TaCl_2(OEt_2)$·Et_2O (**1-Ta**·Et_2O). Computed bond-lengths (PBE0/TZVP) are indicated in brackets

	1-V		1-Nb		1-Ta[a]	
M–Cl(1)	2.3399(9)	[2.3185]	2.4123(5)	[2.3781]	2.367(2)	[2.3781]
M–Cl(2)	2.3443(9)	[2.3173]	2.3893(5)	[2.3789]	2.388(3)	[2.3789]
M–O(3)	2.0632(18)	[2.1103]	2.2181(12)	[2.3219]	2.183(7)	[2.3219]
M–O(1)	1.811(2)	[1.8314]	1.9020(11)	[1.8999]	1.877(6)	[1.8999]
M–O(2)	1.819(2)	[1.8036]	1.8953(11)	[1.8991]	1.894(6)	[1.8991]
M–N(1)	1.9955(19)	[2.0562]	2.0714(12)	[2.0507]	2.040(7)	[2.0507]
O(1)–C(2)	1.336(3)	[1.3183]	1.3632(19)	[1.3454]	1.359(10)	[1.3454]
O(2)–C(16)	1.327(3)	[1.3142]	1.3619(19)	[1.3426]	1.423(11)	[1.3426]
N(1)–C(1)	1.381(4)	[1.3614]	1.407(2)	[1.3963]	1.405(13)	[1.3963]
N(1)–C(15)	1.390(3)	[1.3655]	1.411(2)	[1.3968]	1.431(12)	[1.3968]
C(1)–C(2)	1.412(4)	[1.4257]	1.405(2)	[1.4032]	1.410(13)	[1.4032]
C(2)–C(3)	1.409(4)	[1.4108]	1.398(2)	[1.3881]	1.392(13)	[1.3881]
C(3)–C(4)	1.376(4)	[1.3910]	1.391(2)	[1.3971]	1.396(14)	[1.3971]
C(4)–C(5)	1.410(4)	[1.4163]	1.401(2)	[1.3902]	1.391(14)	[1.3902]
C(5)–C(6)	1.389(4)	[1.3867]	1.389(2)	[1.3944]	1.384(14)	[1.3944]
C(6)–C(1)	1.400(4)	[1.4096]	1.405(2)	[1.3870]	1.434(13)	[1.3870]

[a] Taken from ref. 2.

Attempts to measure electrochemical data on complexes **1-M** resulted in the observation of sample decomposition. Speculating that the coordinated solvent molecule in complexes **1-M** could be problematic, anionic trichloride complexes, $[(ONO)MCl_3]^-$, were prepared from **1-M** to facilitate the electrochemical studies. The addition of a stoichiometric quantity of $[BnNEt_3][Cl]$ to THF solutions of **1-M** resulted in the formation of the salts $[BnNEt_3][(ONO)MCl_3]$ ($[BnNEt_3]$-[**2-M**], M = V, Nb, Ta) in 76–91% isolated yields (Scheme 1). ^{1}H NMR features for the trichloride anions include a slight upfield shift for the (ONO) ligand proton resonances, the appearance of resonances associated with one equivalent of the $[BnNEt_3]^+$ cation, and the loss of resonances associated with the coordinated solvent molecule.

Access to anions $[$**2-M**$]^-$ allowed for the acquisition of electrochemical data on the three complexes. Fig. 4 shows the differential pulse voltammetry (DPV) data for $[BnNEt_3]$[**2-M**] in MeCN solutions containing 1 mM analyte and 100 mM $[Bu_4N][PF_6]$. Cyclic voltammograms (see ESI†) were also collected, but due to the highly irreversible nature of the redox events at normal scan rates, DPV provided a clearer picture of the oxidation processes for the complexes. Data were collected using a standard three-electrode configuration with a glassy carbon working electrode, a platinum counter electrode, and a silver wire pseudo-reference electrode. All potentials are referenced to the $[Cp_2Fe]^{+/0}$ couple using an internal reference. All three complexes show a one-electron oxidation event at modest potentials. For the tantalum anion $[$**2-Ta**$]^-$, the first oxidation appears at +0.33 V *vs.* $[Cp_2Fe]^{+/0}$. For niobium and vanadium complexes $[$**2-Nb**$]^-$ and $[$**2-V**$]^-$, the first oxidation was anodically shifted by 100 mV and 120 mV, respectively. A second oxidation for $[$**2-Ta**$]^-$ and $[$**2-Nb**$]^-$ appears at +0.68 V and +0.74 V, respectively, but with decreased intensity. The signal for the second oxidation of $[$**2-V**$]^-$ appears at 0.70 V but with even weaker intensity than observed for the niobium and tantalum complexes. We attribute the lower intensity of the second oxidation events to chemical irreversibility stemming from the formation of a highly reactive $[(ONO)MCl_3]^+$ cation. In the case of tantalum, it is known that the complex can accept a seventh ligand,[11] which would lead to the irreversible electrochemical behavior. When the electrochemical potential was increased to 1.3 V on samples of $[$**2-V**$]^-$, a third oxidative event was observed corresponding to the oxidation of free chloride anion.

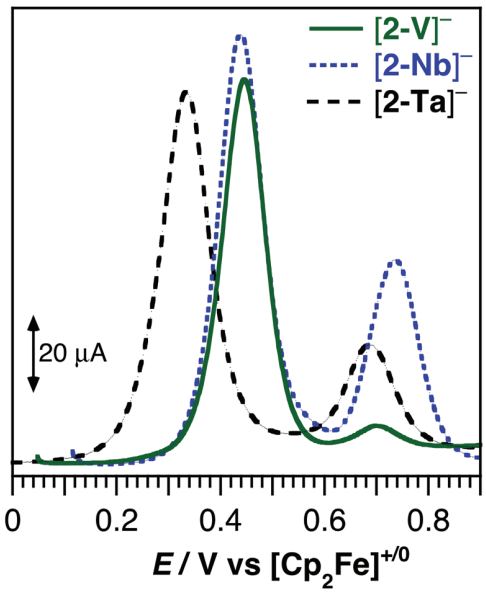

Fig. 4 Differential pulse voltammograms of $[BnNEt_3][(ONO)VCl_3]$ ($[BnNEt_3]$[**2-V**]), $[BnNEt_3][(ONO)NbCl_3]$ ($[BnNEt_3]$[**2-Nb**]), and $[BnNEt_3]$-$[(ONO)TaCl_3]$ ($[BnNEt_3]$[**2-Ta**]). Data were collected using a glassy-carbon working electrode in MeCN solution containing 0.1 M $[Bu_4N][PF_6]$.

Given the modest potentials for the first oxidation of complexes $[$**2-M**$]^-$, attempts were made to chemically access the one-electron oxidized products. The paramagnetic trichloride complex $(ONO)TaCl_3$ (**3-Ta**) has been prepared previously by the reaction of **1-Ta** with one half of an equivalent of $PhICl_2$ as a chlorine atom source;[11] the same procedure afforded $(ONO)NbCl_3$ (**3-Nb**) and $(ONO)VCl_3$ (**3-V**) as microcrystalline green solids in good yields. Consistent with the one-electron oxidation of a diamagnetic compound, all **3-M** complexes are paramagnetic. Crystals of **3-Nb** and **3-V** suitable for X-ray diffraction were obtained from toluene solutions of each complex that were chilled to −35 °C.

In accordance with the structure of **3-Ta**, both **3-V** and **3-Nb** are six-coordinate, distorted octahedral complexes in the solid state. An ORTEP diagram of **3-V** is presented in Fig. 2 and **3-Nb** is structurally analogous. Select metrical data for **3-V** and **3-Nb** are presented alongside data for **3-Ta** in Table 2. Whereas **3-Nb** and **3-Ta** crystallized in isostructural orthorhombic space groups (*Fdd2*), **3-V** crystallized in the monoclinic $P2_1/n$ space group with an asymmetric unit that contains two molecules of **3-V** and one toluene molecule. Bond metrics for **3-Nb** are nearly identical to those for **3-Ta**. Contraction of C–O and C–N bond lengths within the (ONO) ligands of **3-Nb** and **3-Ta** relative to **1-Nb** and **1-Ta**, respectively, are indicative of ligand oxidation up to the semiquinonate oxidation state. Notably these C–O and C–N bond distances in **3-Nb** and **3-Ta** are very similar to the C–O and C–N bond lengths within the (ONO) ligand of $(ONO)VCl_2(THF)$ (**1-V**). The structural data for **3-V** shows further contractions in the C–N and C–O bond lengths suggesting an increased oxidation level in the (ONO) ligand of vanadium complex **3-V**. Congruently, the C–C bond distances within the (ONO) ligand of **3-V** show the familiar cyclohexadiene bond-length pattern, with short C–C distances of 1.36 Å and long C–C distances of 1.42 Å, that are characteristic of a quinone-like ligand.

Complexes **3-M** are all $S = 1/2$ spin systems and EPR spectra indicate delocalization of the unpaired electron over the entire molecule. Fig. 5 shows the X-band EPR spectra of **3-V** and **3-Nb** collected at 298 K in toluene. The room-temperature EPR spectrum of **3-Ta** was reported previously and was characterized as an eight-line, isotropic signal at $g = 1.979$ ($a_{Ta} = 20$ G).[11] Similarly, the EPR spectrum of **3-Nb** shows an isotropic signal at

Table 2 Selected bond lengths (Å) for (ONO)VCl_3·$\frac{1}{2}C_6H_5Me$ (**3-V**·$\frac{1}{2}C_6H_5Me$), (ONO)$NbCl_3$ (**3-Nb**), and (ONO)$TaCl_3$ (**3-Ta**). Computed bond-lengths (PBE0/TZVP) are indicated in brackets

	3-V		3-Nb		3-Ta[a]	
M–Cl(1)	2.3268(15)	[2.2992]	2.3810(4)	[2.3654]	2.3686(14)	[2.3658]
M–Cl(2)	2.3212(15)	[2.2990]	—		—	
M–Cl(3)	2.2158(13)	[2.1943]	2.3247(8)	[2.3237]	2.312(5)	[2.3254]
M–O(1)	1.844(3)	[1.8881]	1.9051(12)	[1.9209]	1.915(4)	[1.9359]
M–O(2)	1.849(3)	[1.8544]	—		—	
M–N(1)	2.133(3)	[2.1738]	2.213(2)	[2.2435]	2.222(13)	[2.2279]
O(1)–C(2)	1.300(4)	[1.2701]	1.340(2)	[1.3246]	1.342(7)	[1.3303]
O(2)–C(16)	1.307(5)	[1.2846]	—		—	
N(1)–C(1)	1.348(5)	[1.3279]	1.3690(18)	[1.3632]	1.362(7)	[1.3643]
N(1)–C(15)	1.352(5)	[1.3415]	—		—	
C(1)–C(2)	1.441(6)	[1.4394]	1.422(2)	[1.4295]	1.429(7)	[1.4236]
C(2)–C(3)	1.412(6)	[1.4190]	1.404(2)	[1.4081]	1.408(7)	[1.4013]
C(3)–C(4)	1.370(5)	[1.3746]	1.386(2)	[1.3924]	1.385(7)	[1.3843]
C(4)–C(5)	1.431(6)	[1.4205]	1.415(2)	[1.4162]	1.418(7)	[1.4095]
C(5)–C(6)	1.357(6)	[1.3690]	1.378(2)	[1.3848]	1.382(7)	[1.3751]
C(6)–C(1)	1.419(5)	[1.4100]	1.411(2)	[1.4119]	1.414(7)	[1.4060]

[a] Taken from ref. 11.

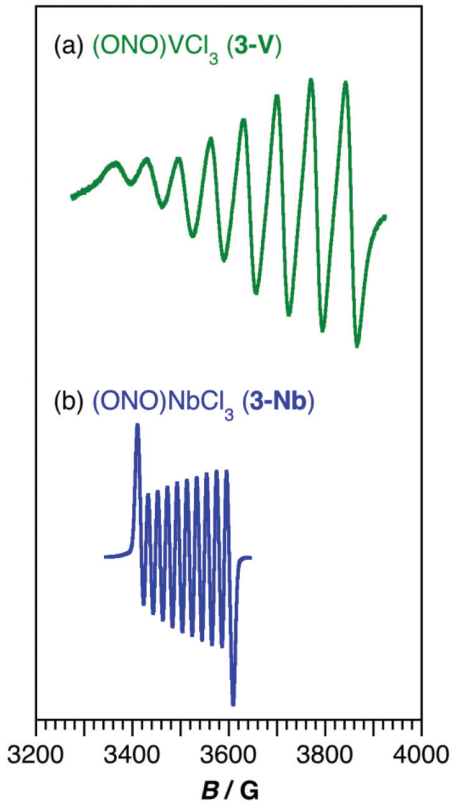

Fig. 5 X-band EPR spectra of (a) (ONO)VCl_3 (**3-V**) and (b) (ONO)$NbCl_3$ (**3-Nb**) collected in toluene at 298 K.

g = 1.990. The ten-line pattern is consistent with hyperfine coupling of the unpaired electron to the I = 9/2 niobium nucleus (a_{Nb} = 20 G).[14,15] In the cases of both **3-Ta** and **3-Nb**, the hyperfine coupling constants are less than 20% of the value normally associated with a classical metal-localized unpaired electron (*i.e.*, M^{IV} oxidation state), suggesting that the upaired electron is localized primarily on the (ONO) ligand. In contrast to **3-Ta** and **3-Nb**, the EPR signal for **3-V** is shifted to g = 1.931 and displays an eight-line pattern due to a 70 G hyperfine coupling to the I = 7/2 vanadium center. Both the g value of the unpaired electron and the large hyperfine coupling constant suggest significant vanadium(IV) character in **3-V**, which is normally characterized by g values between 1.946–2.055 and coupling constants of 90–113 G.[16]

The electronic absorption spectra for **3-M** show evidence for oxidized (ONO) ligands in these three complexes. The spectra for **3-Ta** and **3-Nb** are highly congruous, displaying intense, high-energy bands near 320 nm accompanied by lower-intensity features at 600 and 900 nm. The low-energy band observed in the spectra for **3-Ta** and **3-Nb** are characteristic of metal complexes containing the (ONO) ligand in the semiquinonate oxidation state. Again the spectroscopic data for **3-V** differ from those for **3-Ta** and **3-Nb**. The electronic absorption data for **3-V** are all blue-shifted, with four distinct and moderate-intensity absorption bands visible between 400 nm to 800 nm.

DFT computations on (ONO)MCl_2L and (ONO)MCl_3 (M = V, Nb, Ta)

Density functional theory (DFT) computations were used to model complexes **1-M** and **3-M** to model their electronic structures. Of primary interest was to determine if the modeled distribution of valence electrons between the redox-active ligand and the metal could be correlated to differences in structural and spectroscopic properties of the complexes. Gas-phase DFT calculations were carried out at the PBE0/def2-TZVP level of theory.[17,18] For complexes **1-Nb**, **1-Ta**, and **3-M**, structural data from the aforementioned X-ray diffraction experiments were used as a starting point for initial geometry optimizations. In the case of **1-V**, coordinates for (ONO)VCl_2(THF) were used as a starting point to construct the homologue (ONO)$VCl_2(OEt_2)$ for more direct structural comparisons to **1-Nb** and **1-Ta**.

Complexes of **1-Nb** and **1-Ta** were described well by a singlet closed-shell Kohn–Sham DFT (KS-DFT) solution. Geometry optimization calculations on **1-Nb** and **1-Ta** converged to a closed-shell, $S = 0$ electronic structure, and attempts to locate a low-energy, broken-symmetry singlet state resulted in spontaneous collapse to the closed-shell singlet solution. Computed bond distances for **1-Nb** and **1-Ta** appear in Table 1 alongside the data derived from single-crystal diffraction experiments. The computational data are fully consistent with an electronic structure that puts the (ONO) ligand in the fully-reduced, catecholate oxidation state and the metal in the terminal oxidation state: $(ONO^{cat})M^{V}Cl_2(Et_2O)$ (M = Nb, Ta). These closed-shell singlet solutions for **1-Nb** and **1-Ta** were used as the starting point for time-dependent density functional theory (TD-DFT) calculations, which afforded computed spectra that agree qualitatively with the experimental spectra of Fig. 3. Table 3 summarizes the calculated energies and oscillator strengths of the electronic transitions for **1-Nb** and **1-Ta** along with orbital parentage of each transition. Notably, the spectra of both **1-Nb** and **1-Ta** are dominated by ligand-centered and ligand-to-metal charge-transfer (LMCT) transitions, again consistent with the formal oxidation state assignment of $(ONO^{cat})M^{V}Cl_2(Et_2O)$ for niobium and tantalum metals.

In contrast to the calculated results for **1-Nb** and **1-Ta**, DFT calculations for **1-V** converged to an open-shell singlet diradical ground state. Attempts to model **1-V** as a closed-shell singlet electronic state converged normally to a stable minimum; however, this solution exhibited an electronic instability suggesting the presence of a lower-energy, broken-symmetry solution.[19] Furthermore, the closed-shell solution gave bond lengths inconsistent with the experimental data shown in Table 1.

The broken-symmetry DFT treatment of **1-V** afforded an open-shell singlet solution that lies 0.4 eV lower in energy than the aforementioned singlet closed-shell solution. This broken-symmetry, diradical ground state for **1-V** places one unpaired electron on the vanadium center and one unpaired electron on the (ONO) ligand (see Fig. 7). Thus, the electron distribution is best represented as a one-electron-oxidized (ONO) ligand and a one-electron-reduced vanadium center: $(ONO^{sq})V^{IV}Cl_2(OEt_2)$. Anti-ferromagnetic coupling between the metal- and ligand-localized radicals results in a singlet spin state. Such an open-shell singlet state is approximately represented by a symmetry-broken singlet KS determinant with an S^2 value between 0 (the value for a pure singlet state) and 2 (the value for a pure triplet state).[19,20] The broken symmetry $S = 1$ solution for **1-V** provided bond distances and angles in agreement with the experimental structural data presented in Table 1, and TD-DFT calculations using the broken-symmetry solution for **1-V** reproduced the observed electronic spectral features presented in Fig. 3. Most prominently, the TD-DFT calculations predicted two metal-to-ligand charge-transfer transitions (MLCT) in the UV-vis portion of the spectrum (Table 3), consistent with a vanadium(IV) metal center coordinated to an oxidized (ONO) ligand.

In the cases of **3-M**, all three metal complexes are $S = 1/2$ spin systems, requiring the use of a spin-unrestricted DFT computational scheme. Geometry optimizations were carried out on **3-V**, **3-Nb**, and **3-Ta**, starting from the geometry defined by single-crystal X-ray diffraction data. Optimized bond distances for all three complexes are presented along side the experimental data in Table 2 and in all cases the calculated distances are in reasonably good agreement with the experi-

Table 3 Calculated electronic absorption energies ΔE, wavelengths λ and oscillator strengths f (length representation) of the four most intense electronic transitions along with transition assignments for $(ONO)VCl_2(OEt_2)$ (**1-V**-Et_2O), $(ONO)NbCl_2(OEt_2)$ (**1-Nb**), and $(ONO)TaCl_2(OEt_2)$ (**1-Ta**)

	Excitation	ΔE/eV	λ/nm	f	Assignment
1-V-Et_2O	31	3.44	361	0.066	n(Cl) → π*
	23	3.11	399	0.020	π, n(Cl) → π*
	13	2.74	452	0.065	π → π*
	4	1.80	687	0.050	π,n(Cl) → π*
1-Nb	14	4.60	270	0.276	π → π*,Nb(d)
	7	3.69	335	0.105	π → Nb(d)
	4	3.24	382	0.027	π → Nb(d),n(Cl)
	3	2.72	455	0.036	π → Nb(d),n(O)
1-Ta	12	4.66	266	0.236	π → π*,Ta(d)
	6	3.95	314	0.062	π → Ta(d)
	4	3.72	334	0.019	π → Ta(d),n(Cl)
	3	3.15	393	0.047	π → Ta(d),n(O)

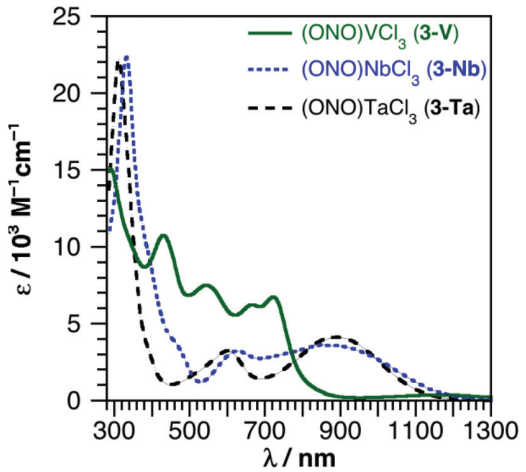

Fig. 6 Electronic absorption spectra of $(ONO)VCl_3$ (**3-V**), $(ONO)NbCl_3$ (**3-Nb**), and $(ONO)TaCl_3$ (**3-Ta**) in benzene.

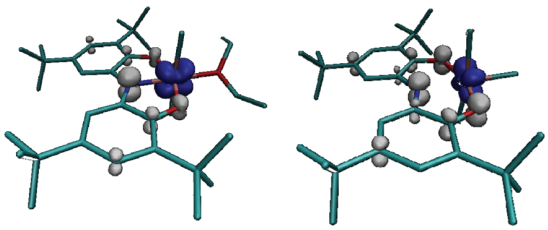

Fig. 7 Plots of the calculated spin density for $(ONO)VCl_2(Et_2O)$ (**1-V**-Et_2O, *left*) and $(ONO)VCl_3$ (**3-V**, *right*). Hydrogen atoms are omitted for clarity.

Table 4 Calculated electronic absorption energies ΔE, wavelengths λ and oscillator strengths f (length representation) of the four most intense electronic transitions along with transition assignments for (ONO)VCl_3 (**3-V**), (ONO)$NbCl_3$ (**3-Nb**), and (ONO)$TaCl_3$ (**3-Ta**)

	Excitation	ΔE/eV	λ/nm	f	Assignment
3-V	35	3.24	383	0.190	$\pi \rightarrow$ V(d),n(Cl)
	24	2.80	442	0.046	π,n(Cl) $\rightarrow \pi^*$
	16	2.40	517	0.015	π,n(Cl) $\rightarrow \pi^*$
	6	1.79	694	0.099	π,n(Cl) $\rightarrow \pi^*$
3-Nb	15	3.44	360	0.019	$\pi \rightarrow$ Nb(d),n(Cl)
	6	2.77	448	0.012	π,n(Cl) $\rightarrow$ Nb(d),n(Cl)
	5	2.32	535	0.050	$\pi \rightarrow \pi^*$
	1	1.56	794	0.067	π,n(Cl) $\rightarrow \pi^*$
3-Ta	24	4.12	301	0.108	$\pi \rightarrow$ Ta(d),n(Cl)
	13	3.52	351	0.022	π,n(Cl) $\rightarrow \pi^*$
	3	2.29	541	0.070	$\pi \rightarrow \pi^*$
	1	1.53	808	0.074	π,n(Cl) $\rightarrow \pi^*$

mental distances. For the heavier congeners **3-Nb** and **3-Ta**, contracted C–O and C–N bond distances are reproduced by the DFT calculation, as are the small differences in C–C bond lengths in the six-member aromatic rings. Both of these structural features implicate an $(ONO^{sq})M^{V}Cl_3$ oxidation state assignment for the Nb and Ta derivatives.

In the case of vanadium complex **3-V**, the computation reproduces the general features of the **3-V** structural data, with a slight over-emphasis on ligand-based oxidation. Given a diradical $(ONO^{sq})V^{IV}Cl_2(OEt_2)$ electronic structure for **1-V**, addition of a chlorine atom to afford **3-V** could plausibly result in a $(ONO^{sq})V^{V}Cl_3$ species (metal-based oxidation) or a (ONO^{q})-$V^{IV}Cl_3$ species (ligand-based oxidation) if localization of the free electron is preserved. The metrical parameters obtained from the DFT calculation show C–O and C–N bond distances that are slightly shorter than the experimental values; however, the calculation faithfully reproduces the C–C bond distances within the ligand backbone. These results suggest the latter, $(ONO^{q})V^{IV}Cl_3$, electronic structure for **3-V**. This assignment is supported by a natural population analysis of the spin density, which shows significant vanadium d-orbital character. TD-DFT calculations for **3-V** reproduces the absorption features of Fig. 6. Calculated energies and intensities, along with orbital parentages for each transition are provided in Table 4.

Conclusion

Isostructural vanadium, niobium, and tantalum complexes of the (ONO) ligand platform have been prepared and characterized to elucidate the impact that metal ion has on the redox activity of the ligand platform. In the cases of complexes of the heavier metals niobium and tantalum, experimental and theoretical treatments indicate that the terminal +5 oxidation state is favored for the metal ion. In contrast, the vanadium species all favor the +4 oxidation state for the metal. Thus, for the reported isostructural complexes of vanadium and niobium/tantalum, the (ONO) ligand is always one oxidation state higher in the vanadium complex than in the niobium/tantalum complex. Despite this shift in electron distribution between the metal and ligand upon descending a column of the Periodic Table, all three 1 M complexes behave analogously upon reaction with chlorine atom sources: the (ONO) ligand is oxidized by one electron and the chloride anion coordinates to the metal center, which does not change oxidation state.

Another curious consequence of the electron distribution in **1-V** is the ground state electronic structure as computed by DFT. While **1-Nb** and **1-Ta** are best described by closed-shell electronic structures, the $(ONO^{sq})V^{IV}Cl_2L$ electronic structure of **1-V** is best described by a broken symmetry solution that places one unpaired electron on the vanadium and a second on the (ONO) ligand: an $S = 0$ diradical state. While these electrons occupy orbitals of the same symmetry, the contracted nature of the vanadium d orbital does not allow for significant π overlap, which would result in a closed-shell ground-state configuration. Efforts are currently underway to determine what if any reactivity differences may result from analogous complexes with diradical *versus* closed-shell ground-state electronic structures.

Experimental

General considerations

Due to the moisture- and oxygen-sensitivity of the compounds mentioned below, all manipulations were carried out in a nitrogen atmosphere using standard glovebox techniques. Solvents initially were degassed by sparging with argon and further purified by sequential passage through activated Q5 and alumina columns to remove oxygen and water, respectively. The solvents were tested for oxygen and water removal using a purple solution of sodium benzophenone ketyl radical in THF. Reagents were purchased from commercial sources and used as received except $[ONO^{cat}]H_3$,[11] $PhICl_2$,[21] $[ONO^{q}]K$,[22] **1-Ta**, $[BnNEt_3][$**2-Ta**$]$, and **3-Ta**,[11] which were synthesized according to published literature procedures.

Physical measurements

NMR spectra were collected on Bruker DRX 400 or 500 MHz spectrometers in dry, degassed benzene-d_6, acetonitrile-d_3 or chloroform-d_1. ^{1}H NMR spectra were referenced to TMS using the residual proteo species of the solvent; $^{13}C\{^1H\}$ NMR spectra were referenced to TMS using the natural abundance ^{13}C present in the solvent. All chemical shifts are reported in the standard notation using parts per million; positive chemical shifts are to a higher frequency from TMS. Electronic absorption spectra were recorded with a Perkin-Elmer Lambda 800 UV-vis spectrophotometer or Perkin-Elmer Lambda 900 UV-vis-NIR spectrophotometer. Perpendicular-mode X-band EPR spectra were collected using a Bruker EMX spectrometer equipped with an ER041XG microwave bridge. The EPR spectra were fit using the EasySpin software add-on for MatLab.[23]

Electrochemistry

Electrochemical data were collected with a Gamry Reference 600 Series Potentiostat/Galvanostat/ZRA (Gamry Instruments,

Warminster, PA, U.S.A.) using a 3.0 mm glassy carbon working electrode, a platinum wire auxiliary electrode, and a silver wire reference electrode. Electrochemical experiments were performed at room temperature in a glovebox under an atmosphere of nitrogen. Samples were typically acetonitrile solutions containing 1.0 mM of the desired analyte and 0.10 M (n-Bu_4N)PF_6 as the supporting electrolyte. All potentials are referenced to an internal $[Cp_2Fe]^{+/0}$ standard.[24] The typical solvent system window with our configuration was +1.5 V for the oxidation limit and 0 V for the reduction limit (*vs.* $[Cp_2Fe]^{+/0}$). Ferrocene (Acros) was purified by sublimation under reduced pressure and tetra-*n*-butylammonium hexafluorophosphate (Acros) was recrystallized from ethanol three times and dried under vacuum. To verify that electrode processes were diffusion-controlled, forward peak currents were plotted with respect to the square root of scan rates in the range of 50 to 1600 mV s^{-1} and found to be linear.

X-ray crystallography

Crystals were mounted on a glass fiber and transferred to a Bruker SMART APEX II diffractometer. APEX2[25] was used to determine the unit-cell parameters and for data collection. The raw frame data was processed using SAINT[26] and SADABS[27] to yield the reflection data file. Subsequent calculations were carried out using SHELXTL.[28] Structures were solved by direct methods and refined on F^2 by full-matrix least-squares techniques. Analytical scattering factors for neutral atoms were used throughout the analysis.[29] Hydrogen atoms were included using a riding model. ORTEP diagrams were generated using ORTEP-3 for Windows.[30] Diffraction data for **1-V**, **1-Nb**, **3-V**, and **3-Nb** can be found in Table 5.

Computational methods

Calculations were performed employing the non-empirical hybrid-GGA functional PBE0.[17] For computational efficiency, initial geometry optimizations were performed using moderate split-valence plus polarization basis sets (def2-SVP).[31] Structures were refined using basis sets of triple zeta valence plus polarization (def2-TZVP) quality.[18] Small-core pseudopotentials for niobium and tantalum were used throughout.[32] When available, crystal structures obtained from X-ray diffraction experiments were used as starting points for the geometry optimization; no molecular symmetry was imposed. In the case of **1-V**, the model complex **1-V**-Et_2O was constructed for better comparisons to **1-Nb** and **1-Ta**. Energies and minimum energy structures were evaluated self-consistently to tight convergence criteria (energy converged to 0.1 μHartree, maximum norm of the Cartesian gradient $\leq 10^{-4}$ a.u.). The vanadium broken symmetry solution was found by geometry optimization of the lowest triplet excited state using spin-unrestricted KS theory and subsequent reoptimization of the spin-unrestricted singlet solution. Minima on the ground-state potential energy surface were verified by analytical second derivatives of the energy with respect to nuclear coordinates at the PBE0/SVP level.[32] Linear-response time-dependent DFT was used to simulate electronic absorption spectra of the two series.[33] All calculations were performed using the quantum chemistry program package TURBOMOLE.[34,35]

Synthesis of (ONO)VCl_2(THF) (1-V)

In a 100 mL round-bottom flask, $[ONO^q]K$ (1.364 g, 2.96 mmol) was dissolved in 75 mL of THF and frozen in a liquid nitrogen cold well. In a 250 mL round-bottom flask, $VCl_3(THF)_3$ was dissolved in 25 mL THF and frozen as well. Once the $[ONO^q]K$ solution was thawed, it was added dropwise to the recently thawed $VCl_3(THF)_3$ solution. The pink solution turned into a dark purple. The solution was allowed to stir for 1 day. The volatiles were removed under vacuum. The purple solid was triturated 3 times with diethyl ether, removing the solvent under vacuum between each trituration. The product was extracted with diethyl ether and filtered until the filtrate was almost colorless. The product was isolated by removing

Table 5 Diffraction data for (ONO)VCl_2(THF) (**1-V**), (ONO)$NbCl_2(OEt_2)$ (**1-Nb**), (ONO)VCl_3 (**3-V**), and (ONO)$NbCl_3$ (**3-Nb**)

	(ONO)VCl_2(THF)·THF **1-V**·THF	(ONO)$NbCl_2(OEt_2)$·C_5H_{12} **1-Nb**·C_5H_{12}	(ONO)VCl_3·$\frac{1}{2}C_7H_8$ **3-V**·$\frac{1}{2}C_7H_8$	(ONO)$NbCl_3$ **3-Nb**
Empirical formula	$C_{36}H_{56}Cl_2NO_4V$	$C_{37}H_{62}NO_3Cl_2Nb$	$C_{31.5}H_{44}Cl_3NO_2V$	$C_{28}H_{40}NO_2NbCl_3$
Formula weight	688.66	732.69	625.96	621.87
Crystal system	Monoclinic	Orthorhombic	Monoclinic	Orthorhombic
Space group	$P2_1/n$	$P2_12_12_1$	$P2_1/n$	$Fdd2$
a/Å	16.6922(12)	14.5710(10)	9.5015(8)	18.7255(12)
b/Å	10.7697(8)	15.9423(11)	22.5812(19)	27.2787(17)
c/Å	20.4145(15)	17.0831(12)	31.221(3)	11.9550(7)
α/°	90	90	90	90
β/°	93.0439(10)	90	91.0821(14)	90
γ/°	90	90	90	90
V/Å^3	3664.7(5)	3968.3(5)	6697.3(10)	6106.7(7)
Z	4	4	8	8
Refl. collected	7481	45 745	18 750	13 033
Indep. Refl.	7481	9374 (R_{int} = 0.0220)	18 750	3580 (R_{int} = 0.0213)
R_1[a] ($I > 2\sigma_I$)	0.0410	0.0229	0.0590	0.0198
wR_2[b] (all data)	0.0994	0.0587	0.1287	0.0473

[a] $R_1 = \sum||F_o| - |F_c||/\sum|F_o|$. [b] $wR_2 = [\sum[w(F_o^2 - F_c^2)^2]/\sum[w(F_o^2)^2]]^{1/2}$.

the volatiles under vacuum, yielding a dark purple powder. Yield: 1.759 g (96%). Anal. Calc. (Found) for $C_{32}H_{48}Cl_2NO_3V$: C 62.33 (62.47), H 7.85 (8.01), N 2.27 (1.99). ^{1}H NMR (500 MHz, C_6D_6) δ/ppm: 1.11 (s, 18H, ^{t}Bu), 1.17 (s, 18H, ^{t}Bu), 1.40 (s, b, 4H, THF–CH_2), 4.38 (s, b, 4H, THF–O–CH_2), 6.40 (s, 2H, aryl-H), 6.54 (s, 2H, aryl-H). $^{13}C\{^1H\}$ NMR (125.6 MHz, $CDCl_3$) δ/ppm: 15.09 (THF–CH_2), 29.75 ($C(CH_3)_3$), 31.17 ($C(CH_3)_3$), 34.49 ($C(CH_3)_3$), 34.90 ($C(CH_3)_3$), 66.23 (THF–O–CH_2), 111.76 (aryl-C), 126.30 (aryl-C), 127.12 (aryl-C), 128.15 (aryl-C), 128.96 (aryl-C), 153.60 (aryl-C). UV-vis (Et_2O) λ_{max}/nm (ε/M^{-1} cm^{-1}): 298 (21 600), 496 (10 000), 542 (9800).

Synthesis of (ONO)$NbCl_2(Et_2O)$ (1-Nb)

In a 100 mL round-bottom flask, $[ONO^{cat}]H_3$ (1.568 g, 3.68 mmol) was dissolved in 50 mL of toluene and 1 mL of diethyl ether. The solution was then frozen in a cold well. Upon thawing, 3 equivalents of *n*-BuLi (4.15 mL, 11.05 mmol, 2.66 M in hexanes) were added dropwise to the solution. The yellow solution was allowed to stir for 3 hours. The yellow $[ONO^{cat}]Li_3$ solution was then added dropwise to a slurry of $NbCl_5$ (1.065 g, 3.94 mmol) in *ca.* 10 mL of toluene. The reaction was stirred for one day. The volatiles were removed under vacuum, then extracted and filtered with diethyl ether until the filtrate was colorless. The volatiles were removed under vacuum, yielding a dark purple powder. Yield: 2.413 g (99%). Anal. Calc. (Found) for $C_{32}H_{50}Cl_2NO_3Nb$: C 58.18 (58.34), H 7.63 (7.58), N 2.12 (2.09). ^{1}H NMR (400 MHz, C_6D_6) δ/ppm: 1.07 (t, J = 8 Hz, 6H, Et_2O–CH_3), 1.26 (s, 18H, ^{t}Bu), 1.37 (s, 18H, ^{t}Bu), 3.54 (q, J = 8 Hz, 4H, Et_2O–CH_2), 6.92 (s, 2H, aryl-H), 7.10 (s, 2H, aryl-H). $^{13}C\{^1H\}$ NMR (100.6 MHz, C_6D_6) δ/ppm: 15.08 (Et_2O–CH_3), 30.11 ($C(CH_3)_3$), 32.01 ($C(CH_3)_3$), 34.94 ($C(CH_3)_3$), 35.32 ($C(CH_3)_3$), 68.34 (Et_2O–CH_2), 111.66 (aryl-C), 121.03 (aryl-C), 133.65 (aryl-C), 145.13 (aryl-C), 147.74 (aryl-C), 160.44 (aryl-C). UV-vis (Et_2O) λ_{max}/nm (ε/M^{-1} cm^{-1}): 290 (21 800), 370 (9400), 540 (3600).

Synthesis of [$BnNEt_3$][(ONO)VCl_3] ([$BnNEt_3$][2-V])

To a stirring solution of **1-V** (0.194 g, 0.315 mmol) in 10 mL THF, $BnNEt_3Cl$ (0.072 g, 0.316 mmol) was added and the solution was allowed to stir overnight. The purple solution was then concentrated under vacuum to *ca.* 5 mL and 10 mL of pentane was added, causing the product to precipitate out. The solution was allowed to sit at room temp for 5 hours, and then the product was filtered and washed with Et_2O. The product was dried under vacuum and isolated as a dark purple powder. Yield: 0.186 g (76%). ^{1}H NMR (500 MHz, CD_3CN) δ/ppm: 1.12 (s, 18H, ^{t}Bu), 1.44 (s, 18H, ^{t}Bu), 1.47 (b, 9H, Et-CH_3), 3.29 (s, br, 6H, Et-CH_2), 4.47 (s, 2H, benzyl-CH_2), 6.59 (s, 2H, aryl-H), 6.65 (s, 2H, aryl-H), 7.63 (s, 4H, Benzyl-aryl-H), 7.66 (s, 1H, benzyl-aryl-H). $^{13}C\{^1H\}$ NMR (125.6 MHz, CD_3CN) δ/ppm: 9.00 (Et-CH_3), 28.89 ($C(CH_3)_3$), 31.34 ($C(CH_3)_3$), 34.72 ($C(CH_3)_3$), 35.52 ($C(CH_3)_3$), 54.42 (Et-CH_2), 62.59 (benzyl-CH_2), 113.38 (aryl-C), 127.41 (aryl-C), 128.26 (aryl-C), 130.32 (aryl-C), 131.62 (aryl-C), 133.83 (aryl-C), 153.11 (aryl-C), 172.22 (aryl-C).

Synthesis of [$BnNEt_3$][(ONO)$NbCl_3$] ([$BnNEt_3$][2-Nb])

To a stirring solution of **1-Nb** (0.202 g, 0.306 mmol) in 10 mL of THF, $BnNEt_3Cl$ (0.071 g, 0.312 mmol) was added and the solution was allowed to stir overnight. The purple solution was then concentrated under vacuum and pentane was added, causing the product to precipitate out. The solution was allowed to sit at room temp for a 5 hours, and then the product was filtered and washed with Et_2O. The product was dried under vacuum and isolated as dark purple crystals. Yield: 0.248 g (91%). ^{1}H NMR (500 MHz, C_6D_6) δ/ppm: 0.95 (t, J = 7 Hz, 9H, Et-CH_3), 1.27 (s, 18H, ^{t}Bu), 1.45 (s, 18H, ^{t}Bu), 2.74 (q, J = 7 Hz, 6H, Et-CH_2), 4.00 (s, 2H, benzyl-CH_2), 6.88 (d, J = 2 Hz, 2H, aryl-H), 7.12 (m, 5H, benzyl-aryl-H), 7.19 (m, 2H, aryl-H). $^{13}C\{^1H\}$ NMR (125.6 MHz, C_6D_6) δ/ppm: 8.65 (Et-CH_3), 30.36 ($C(CH_3)_3$), 32.17 ($C(CH_3)_3$), 35.10 ($C(CH_3)_3$), 35.24 ($C(CH_3)_3$), 53.38 (Et-CH_2), 61.40 (benzyl-CH_2), 111.45 (aryl-C), 119.63 (aryl-C), 127.71 (aryl-C), 129.87 (aryl-C), 130.89 (aryl-C), 133.00 (aryl-C), 133.16 (aryl-C), 144.40 (aryl-C), 146.38 (aryl-C), 161.51 (aryl-C).

Synthesis of (ONO)VCl_3 (3-V)

Complex **1-V** (0.308 g, 0.500 mmol) was dissolved in 8 mL toluene and frozen in a cold well. $PhICl_2$ (0.069 g, 0.251 mmol) was dissolved in 5 mL of toluene and placed in a −35 °C freezer for 15 minutes. Once the solution of **1-V** thawed, the $PhICl_2$ solution was added dropwise and the solution was mixed until the solution turned to a dark green. The solution was then placed in the freezer overnight. The product was isolated as a microcrystalline, dark green solid. Yield: 0.205 g (71%). Anal. Calc. (Found) for $C_{28}H_{40}Cl_3NO_2V$: C 57.99 (58.16), H 6.95 (6.87), N 2.42 (2.32). UV-vis (benzene) λ_{max}/nm (ε/M^{-1} cm^{-1}): 434 (11 700), 557 (7200), 665 (6800), 723 (7400).

Synthesis of (ONO)$NbCl_3$ (3-Nb)

Complex **1-Nb** (0.203 g, 0.307 mmol) was dissolved in 8 mL of Diethyl ether and frozen in the nitrogen cold well. $PhICl_2$ (0.042 g, 0.5 equiv.) was dissolved in 5 mL of toluene and cooled at −35 °C for 15 min. Then, $PhICl_2$ solution was added dropwise to the recently thawed solution of **1-Nb** and the mixture was shaken to mix. Upon observing the color change from purple to green, the mixture was cooled at −35 °C overnight. The green microcrystalline solid was collected the next day and washed with pentane and dried under vacuum. Yield: 0.114 g (60%). Anal. Calc. (Found) for $C_{28}H_{40}Cl_3NO_2Nb$: C 53.90 (53.83), H 6.79 (6.45), N 2.25 (2.19). UV-vis (benzene) λ_{max}/nm (ε/M^{-1} cm^{-1}): 334 (23 200), 465 (4000), 628 (3200), 883 (3700).

Acknowledgements

This work was supported by the National Science Foundation (CHE-1152543 to AFH) and by the Department of Energy (DE-SC0008694 to FF). AFH is a Camille Dreyfus Teacher-Scholar.

Notes and references

1 P. J. Chirik and K. Wieghardt, *Science*, 2010, **327**, 794–795.
2 A. F. Heyduk, R. A. Zarkesh and A. I. Nguyen, *Inorg. Chem.*, 2011, **50**, 9849–9863.
3 V. K. K. Praneeth, M. R. Ringenberg and T. R. Ward, *Angew. Chem., Int. Ed.*, 2012, **51**, 10228–10234.
4 D. D. Wright and S. N. Brown, *Inorg. Chem.*, 2013, **52**, 7831–7833.
5 A. B. P. Lever, *Coord. Chem. Rev.*, 2010, **254**, 1397–1405.
6 H. Masui, A. B. P. Lever and P. R. Auburn, *Inorg. Chem.*, 1991, **30**, 2402–2410.
7 P. Chaudhuri, C. N. Verani, E. Bill, E. Bothe, T. Weyhermüller and K. Wieghardt, *J. Am. Chem. Soc.*, 2001, **123**, 2213–2223.
8 D. Herebian, E. Bothe, E. Bill, T. Weyhermüller and K. Wieghardt, *J. Am. Chem. Soc.*, 2001, **123**, 10012–10023.
9 D. Herebian, E. Bothe, F. Neese, T. Weyhermüller and K. Wieghardt, *J. Am. Chem. Soc.*, 2003, **125**, 9116–9128.
10 S. Kokatam, T. Weyhermüller, E. Bothe, P. Chaudhuri and K. Wieghardt, *Inorg. Chem.*, 2005, **44**, 3709–3717.
11 R. A. Zarkesh, J. W. Ziller and A. F. Heyduk, *Angew. Chem., Int. Ed.*, 2008, **47**, 4715–4718.
12 S. Bruni, A. Caneschi, F. Cariati, C. Delfs, A. Dei and D. Gatteschi, *J. Am. Chem. Soc.*, 1994, **116**, 1388–1394.
13 T. Ren, *Inorg. Chim. Acta*, 1995, **229**, 195–202.
14 D. P. Johnson and R. D. Bereman, *J. Inorg. Nucl. Chem.*, 1972, **34**, 2957–2959.
15 M. D. Fryzuk, C. M. Kozak, M. R. Bowdridge, B. O. Patrick and S. J. Rettig, *J. Am. Chem. Soc.*, 2002, **124**, 8389–8397.
16 J. Zah-Letho, E. Samuel and J. Livage, *Inorg. Chem.*, 1988, **27**, 2233–2237.
17 J. P. Perdew, M. Ernzerhof and K. Burke, *J. Chem. Phys.*, 1996, **105**, 9982–9985.
18 A. Schäfer, C. Huber and R. Ahlrichs, *J. Chem. Phys.*, 1994, **100**, 5829–5835.
19 R. Bauernschmitt and R. Ahlrichs, *J. Chem. Phys.*, 1996, **104**, 9047–9052.
20 J. Gräfenstein, E. Kraka, M. Filatov and D. Cremer, *Int. J. Mol. Sci.*, 2002, **3**, 360–394.
21 H. J. Lucas and E. R. Kennedy, *Org. Synth.*, 1942, **22**, 69.
22 G. Szigethy, D. W. Shaffer and A. F. Heyduk, *Inorg. Chem.*, 2012, **51**, 12606–12618.
23 S. Stoll and A. Schweiger, *J. Magn. Reson.*, 2006, **178**, 42–55.
24 N. G. Connelly and W. E. Geiger, *Chem. Rev.*, 1996, **96**, 877–910.
25 *APEX2 V2.2-0*, Bruker AXS, Inc., Madison, WI, 2007.
26 *SAINT V7.58a*, Bruker AXS, Inc., Madison, WI, 2007.
27 G. M. Sheldrick, *SADABS V2007/4*, Bruker AXS, Inc., Madison, WI, 2007.
28 G. M. Sheldrick, *SHELXTL, V6.12*, Bruker AXS, Inc., Madison, WI, 2001.
29 *International Tables for X-ray Crystallography*, ed. A. J. C. Wilson, Kluwer Academic, Dordrecht, Netherlands, 1992, Vol. C.
30 L. J. Farrugia, *J. Appl. Crystallogr.*, 1997, **30**, 565–565.
31 A. Schäfer, H. Horn and R. Ahlrichs, *J. Chem. Phys.*, 1992, **97**, 2571–2577.
32 D. Andrae, U. Häußermann, M. Dolg, H. Stoll and H. Preuß, *Theor. Chim. Acta*, 1990, **77**, 123–141.
33 P. Elliott, F. Furche and K. Burke, in *Reviews in Computational Chemistry*, ed. K. B. Lipkowitz and T. R. Cundari, Wiley & Sons, Hoboken, NJ, 2009, pp. 91–165.
34 *TURBOMOLE V6.3*, Turbomole GmbH, Karlsruhe, 2011. http://www.turbomole.com.
35 F. Furche, R. Alrichs, C. Hättig, W. Klopper, M. Sierka and F. Weigend, *WIREs Comp. Mol. Chem.*, 2014, **4**, 91–100.

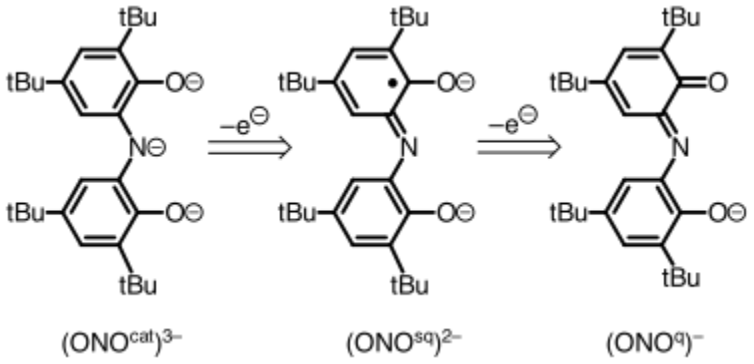

Figure 7.1: Oxidation states of the redox active ligand ONO

Appendices

A Integral of a Gaussian charge density with an Erf-attenuated Coulomb interaction

The evaluation of the the integral over the short-ranged interaction by an error function begins in the same manner as in the Gaussian-attenuated case: rewrite each of the four Gaussian basis functions in terms of relative and center-of-mass coordinates and combine them all using Gaussian product theorem

$$I^{erf} = K \int d^3 r e^{-\gamma(\mathbf{r}-\frac{1}{\gamma}\mathbf{R})^2} \mathrm{Erf}[zr]/r. \tag{1}$$

First, write out Erf in terms of its integral representation

$$I^{erf} = K \int d^3 r e^{-\gamma(\mathbf{r}-\frac{1}{\gamma}\mathbf{R})^2} \left[\frac{2}{\sqrt{\pi}} \int_0^{zr} dt e^{-t^2}\right] /r. \tag{2}$$

Next, substitute $t^2 = z^2 r^2 y^2$;$dt = zrdy$, and rearrange the order of integration

$$I^{erf} = K \int_0^1 dy \int d^3 r \frac{2z}{\sqrt{\pi}} e^{-\gamma(\mathbf{r}-\frac{1}{\gamma}\mathbf{R})^2} e^{-z^2 y^2 r^2}. \tag{3}$$

Using the Gaussian product theorem, we combine the two Gaussians in r

$$I^{erf} = \frac{2z}{\sqrt{\pi}} K \int_0^1 dy \int d^3r e^{-\frac{\gamma z^2 y^2}{\gamma + z^2 y^2}(\frac{1}{\gamma}\mathbf{R})^2} * e^{-(\gamma + z^2 y^2)(\mathbf{r} - \frac{\mathbf{R}}{\gamma + z^2 y^2})} \tag{4}$$

yielding a single Gaussian in r that can be integrated analytically by separating r into its components r_x, r_y, r_z. This results in

$$I^{erf} = \frac{2z}{\sqrt{\pi}} K \int_0^1 dy \left(\frac{\pi}{\gamma + z^2 y^2}\right)^{3/2} e^{-\frac{\gamma z^2 y^2}{\gamma + z^2 y^2}(\frac{1}{\gamma}\mathbf{R})^2}. \tag{5}$$

A change of variables $v = \frac{zy}{\gamma(\gamma + z^2 y^2)^{1/2}}$; $dv = \frac{z}{(\gamma + z^2 y^2)^{3/2}} dy$ yields a simple integral over a Gaussian

$$I^{erf} = 2\pi K \int_0^{\frac{z}{\gamma(\gamma + z^2)^{1/2}}} dv e^{-\gamma v^2 R^2}. \tag{6}$$

Making one more substition for the integration limits, $w = v\left(\frac{\gamma(\gamma + z^2)^{1/2}}{z}\right)$

$$I^{erf} = 2\pi \left(\frac{z}{\gamma(\gamma + z^2)^{1/2}}\right) K \int_0^1 dw e^{-\frac{z^2 R^2}{\gamma(\gamma + z^2)} w^2}. \tag{7}$$

This can be rewritten as the Boys function

$$I^{erf} = 2\pi \left(\frac{z}{\gamma(\gamma + z^2)^{1/2}}\right) K F_0 \left[\frac{z^2}{\gamma(\gamma + z^2)} R^2\right] \tag{8}$$

In order to make this expression compatible with the implementation we make the following definitions:

$$\zeta = \left(\frac{z^2}{\gamma(\gamma + z^2)}\right)^{-1} \tag{9}$$

The following expression is now readily computed by the integral machinery found in the module `nlint`, module procedure `nlasra`. Only modification of the ζ and boysfnarg variables are necessary.

$$I^{erf} = KG_0^{erf} \tag{10}$$

$$G_0^{erf} = 2\pi\sqrt{\frac{\gamma}{\zeta}}F_0\left[\frac{1}{\zeta}R^2\right] \tag{11}$$

B Explicit expressions for G_m^n

For the Gaussian range-separating function, the s-function integral is

$$I = \int d^3u\, Exp[-\zeta(\mathbf{u} - \frac{1}{\zeta}\mathbf{U})^2]\, g(u) \tag{12}$$

where, $g(u) = \frac{1}{u}(c_0 + c_1u + c_2u^2 + \ldots)$ and the remaining variables are defined in Section 2.3.1. Here, we seek to write the auxiliary indices expressions for each different power of u in our interaction. $G_m^{(n)}$ corresponds to the n^{th} power of u corresponding to the coefficienct c_n in the definition of g, while m is the auxiliary index. When generating the auxiliary indices m, we apply the differential operator

$$\hat{d}_m = \left(-\frac{\zeta}{2U}\frac{\partial}{\partial U}\right)^m. \tag{13}$$

First, $G_0^{(n)}$ is evaluted by hand, then a pattern is determined by successive applications of $\hat{d}_m$ generating the relation for the auxiliary index.

$$G_n^{(0)}(\zeta, T) = \frac{2\pi}{\zeta} F_n[T] \tag{14}$$

$$G_0^{(1)}(\zeta, T) = \left(\frac{\pi}{\zeta}\right)^{3/2}; \; G_{n>0}^{(1)} = 0 \tag{15}$$

$$G_n^{(2)}(\zeta, T) = \frac{2\pi}{\zeta^2} \left[(n+1)F_n - nF_{n-1} + T(F_n - F_{n+1})\right] \tag{16}$$

$$G_0^{(3)}(\zeta, T) = \sqrt{\frac{\pi^3}{\zeta^5}}(T + \frac{3}{2}); \; G_1^{(3)}(\zeta, T) = -\sqrt{\frac{\pi^3}{\zeta^5}}; \; G_{n>1}^{(3)}(\zeta, T) = 0 \tag{17}$$

When the integrand is even in u, there is no Boys function dependence. The integration limits can be split in half and evaluted to a closed-form expression dependent only on ζ and T. In principle, generalization over the auxiliary index n and over the order of u is possible but is tedious to be done by hand. Use of a code generator may be beneficial in this case.

C Evaluation of the short-ranged PBE exchange-hole

The short-ranged PBE exchange energy density is constructed by adapting the GGA exchange-hole model constructed by Ernzerhof and Perdew[99] Beginning from the definition of the GGA exchange energy per particle (Eqs. 22 and 23 of Ref. 99), we make a short-ranged modification to the exchange energy per particle:

$$\varepsilon_x^{sr-GGA}(\mathbf{r}) = 2\pi\rho(\mathbf{r}) \int_0^\infty du u J^{GGA}(s, k_F u) e^{-\alpha u^2} \tag{18}$$

where $k_F = (3\pi\rho)^{1/3}$ is the Fermi wavevector and $s = |\nabla\rho|/(2k_F\rho)$ is the reduced gradient. Making the substition to reduced units $y = k_F u$,

$$\varepsilon_x^{sr-GGA}(\mathbf{r}) = 2\pi\rho(\mathbf{r}) \int_0^\infty (k_F^{-1} dy)(k_F^{-1} y) J^{GGA}(s, y) e^{-\alpha(k_F^{-1} y)^2} \tag{19}$$

where J^{GGA} is a quantity related to the GGA exchange hole

$$J^{GGA}(s,y) = G(s,y) * Exp[-s^2\mathcal{H}(s)y^2], \tag{20}$$

and $G(s,y)$ is the term in large square brackets in Eq. 24 of the reference article and remains unchanged. Simplifying the expression for ε_x^{sr-GGA} we get

$$\varepsilon_x^{sr-GGA}(\mathbf{r}) = \frac{2\pi\rho(\mathbf{r})}{k_F^2}\int_0^\infty dyyG(s,y) * Exp[-s^2\mathcal{H}(s)y^2]Exp[-\frac{\alpha}{k_F^2}y^2]. \tag{21}$$

Combining the two Gaussians in y yields

$$J^{sr-GGA}(s,y) = G(s,y) * Exp[-s^2\tilde{\mathcal{H}}(s)y^2] \tag{22}$$

where, $\tilde{\mathcal{H}}(s) = \mathcal{H} + \frac{\alpha}{s^2k_F^2}$.

Bibliography

[1] A. Mukherji, R. Marschall, A. Tanksale, C. Sun, S. C. Smith, G. Q. Lu, and L. Wang, Adv. Funct. Mater. **21**, 126 (2010).

[2] K. Maeda and K. Domen, J. Phys. Chem. C **111**, 7851 (2007).

[3] J. Sato, N. Saito, Y. Yamada, K. Maeda, T. Takata, J. N. Kondo, M. Hara, H. Kobayashi, K. Domen, and Y. Inoue, J. Am. Chem. Soc. **127**, 4150 (2005).

[4] M. K. Nazeeruddin, F. De Angelis, S. Fantacci, A. Selloni, G. Viscardi, P. Liska, S. Ito, B. Takeru, and M. Grätzel, J. Am. Chem. Soc. **127**, 16835 (2005).

[5] C. Di Valentin, G. Pacchioni, A. Selloni, S. Livraghi, and E. Giamello, J. Phys. Chem. B **109**, 11414 (2005).

[6] A. J. Cohen, P. Mori-Sánchez, and W. Yang, Science **321**, 792 (2008).

[7] K. Burke, J. Werschnik, and E. K. U. Gross, J. Chem. Phys. **123**, 062206 (2005).

[8] O. Gunnarsson and B. Lundqvist, Phys. Rev. B **13**, 4274 (1976).

[9] O. Gunnarsson, M. Jonson, and B. I. Lundqvist, Phys. Rev. B **20**, 3136 (1979).

[10] R. Ahlrichs, Theor. Chim. Acta **33**, 157 (1974).

[11] O. Vahtras, J. Almlöf, and M. W. Feyereisen, Chem. Phys. Lett. **213**, 514 (1993).

[12] C. F. Bender, J. Comput. Phys. **9**, 547 (1972).

[13] S. Obara and A. Saika, J. Chem. Phys. **84**, 3963 (1986).

[14] M. Head-Gordon and J. Pople, J. Chem. Phys. **89**, 5777 (1988).

[15] M. Dupuis, J. Rys, and H. King, J. Chem. Phys. **65**, 111 (1976).

[16] H. King and M. Dupuis, J. Comput. Phys. **21**, 144 (1976).

[17] S. Boys, P. Roy. Soc. Lond. A Mat. **200**, 542 (1950).

[18] L. E. McMurchie and E. R. Davidson, J. Comput. Phys. **26**, 218 (1978).

[19] H. B. Schlegel, J. S. Binkley, and J. A. Pople, J. Chem. Phys. **80**, 1976 (1984).

[20] J. A. Pople and W. J. Hehre, J. Comput. Phys. **27**, 161 (1978).

[21] H. Taketa, S. Huzinaga, and K. O-ohata, J. Phys. Soc. Jpn. **21** (1966).

[22] J. Almlöf, K. Faegri, and K. Korsell, J. Comp. Chem. **3**, 385 (1982).

[23] S. A. Losilla, M. M. Mehine, and D. Sundholm, Mol. Phys. **110**, 2569 (2012).

[24] M. Häser and R. Ahlrichs, J. Comp. Chem. **10**, 104 (1989).

[25] C. Roothaan, Rev. Mod. Phys. **23**, 69 (1951).

[26] K. E. Schmidt and M. A. Lee, J. Stat. Phys. **63**, 1223 (1991).

[27] K. N. Kudin and G. E. Scuseria, Chem. Phys. Lett. **289**, 611 (1998).

[28] R. Dovesi, C. Pisani, C. Roetti, and V. R. Saunders, Phys. Rev. B **28**, 5781 (1983).

[29] P. M. W. Gill, Chem. Phys. Lett. **270**, 193 (1997).

[30] M. Sierka, A. Hogekamp, and R. Ahlrichs, J. Chem. Phys. **118**, 9136 (2003).

[31] K. Eichkorn, O. Treutler, H. Oehm, M. Haeser, and R. Ahlrichs, Chem. Phys. Lett. **240**, 283 (1995).

[32] F. Aquilante, T. B. Pedersen, and R. Lindh, J. Chem. Phys. **126**, 194106 (2007).

[33] F. R. Manby, J. Chem. Phys. **119**, 4607 (2003).

[34] Á. Rák and G. Cserey, Chem. Phys. Lett. **622**, 92 (2015).

[35] N. Luehr, I. S. Ufimtsev, and T. J. Martinez, J. Chem. Theory Comput. **7**, 949 (2011).

[36] A. V. Titov, I. S. Ufimtsev, N. Luehr, and T. J. Martinez, J. Chem. Theory Comput. **9**, 213 (2013).

[37] K. Esler, J. Kim, D. Ceperley, and L. Shulenburger, Comput. Sci. Eng. **14**, 40 (2012).

[38] P. Čársky and R. Čurík, Theor. Chem. Acc. **133**, 1466 (2014).

[39] O. A. Vydrov and T. Van Voorhis, Phys. Rev. Lett. **103**, 063004 (2009).

[40] O. A. Vydrov and T. Van Voorhis, J. Chem. Phys. **133**, 244103 (2010).

[41] T. Shiozaki, J. Chem. Phys. **138**, 111101 (2013).

[42] R. Haunschild, T. M. Henderson, C. A. Jiménez-Hoyos, and G. E. Scuseria, J. Chem. Phys. **133**, 134116 (2010).

[43] J. Gräfenstein and D. Cremer, Theor. Chem. Acc. **123**, 171 (2009).

[44] U. R. Fogueri, S. Kozuch, A. Karton, and J. M. L. Martin, Theor. Chem. Acc. **132**, 1291 (2012).

[45] M. Hellgren, F. Caruso, D. R. Rohr, X. Ren, A. Rubio, M. Scheffler, and P. Rinke, Phys. Rev. B **91**, 165110 (2015).

[46] J. W. Hollett and P. M. W. Gill, J. Chem. Phys. **134**, 114111 (2011).

[47] R. Ahlrichs, Phys. Chem. Chem. Phys. **8**, 3072 (2006).

[48] M. Abramowitz and I. A. Stegan, *Handbook of Mathematical Functions* (Dover Publications, NY, 1965).

[49] I. Shavitt, *The Gaussian Function in Calculations of Statistical Mechanics and Quantum Mechanics*, methods in computational physics ed., Vol. 2 (1963).

[50] T. Helgaker, P. Jørgensen, and J. Olsen, *Molecular electronic-structure theory* (John Wiley & Sons, 2014).

[51] F. Furche, R. Ahlrichs, C. Hättig, W. Klopper, M. Sierka, and F. Weigend, WIREs Comput. Mol. Sci. **4**, 91 (2014).

[52] A. D. Becke, J. Chem. Phys. **88**, 2547 (1988).

[53] O. Treutler and R. Ahlrichs, J. Chem. Phys. **102**, 346 (1995).

[54] R. Lindh, U. Ryu, and B. Liu, J. Chem. Phys. **95**, 5889 (1991).

[55] S. Maheshwary, N. Patel, N. Sathyamurthy, A. D. Kulkarni, and S. R. Gadre, J. Phys. Chem. A **105**, 10525 (2001).

[56] A. Becke, J. Chem. Phys. **98**, 5648 (1993).

[57] J. P. Perdew, M. Ernzerhof, and K. Burke, J. Chem. Phys. **105**, 9982 (1996).

[58] J. P. Perdew and A. Zunger, Phys. Rev. B **23**, 5048 (1981).

[59] P. Mori-Sanchez, A. J. Cohen, and W. Yang, J. Chem. Phys. **125**, 201102 (2006).

[60] A. Ruzsinszky, J. P. Perdew, G. I. Csonka, O. A. Vydrov, and G. E. Scuseria, J. Chem. Phys. **126**, 104102 (2007).

[61] M. Fuchs, Y.-M. Niquet, X. Gonze, and K. Burke, J. Chem. Phys. **122**, 094116 (2005).

[62] T. M. Henderson and G. E. Scuseria, Mol. Phys. **108**, 2511 (2010).

[63] M. Dierksen and S. Grimme, J. Phys. Chem. A **108**, 10225 (2004).

[64] M. Reiher, O. Salomon, and B. Artur Hess, Theor. Chem. Acc. **107**, 48 (2001).

[65] J. Jaramillo, G. E. Scuseria, and M. Ernzerhof, J. Chem. Phys. **118**, 1068 (2003).

[66] E. R. Johnson, J. Chem. Phys. **141**, 124120 (2014).

[67] B. G. Janesko and G. E. Scuseria, J. Chem. Phys. **127**, 164117 (2007).

[68] B. G. Janesko and G. E. Scuseria, J. Chem. Phys. **128**, 084111 (2008).

[69] M. Kaupp, H. Bahmann, and A. V. Arbuznikov, J. Chem. Phys. **127**, 194102 (2007).

[70] A. V. Arbuznikov and M. Kaupp, Chem. Phys. Lett. **440**, 160 (2007).

[71] J. Perdew, V. Staroverov, J. Tao, and G. Scuseria, Phys. Rev. A **78** (2008).

[72] H. Bahmann and M. Kaupp, J. Chem. Theory Comput. **11**, 1540 (2015).

[73] K. Burke, F. G. Cruz, and K.-C. Lam, J. Chem. Phys. **109**, 8161 (1998).

[74] F. G. Cruz, K.-C. Lam, and K. Burke, J. Phys. Chem. A **102**, 4911 (1998).

[75] J. Tao, V. Staroverov, G. Scuseria, and J. Perdew, Phys. Rev. A **77** (2008).

[76] T. M. Henderson, A. F. Izmaylov, G. E. Scuseria, and A. Savin, J. Chem. Phys. **127**, 221103 (2007).

[77] J. Heyd, G. E. Scuseria, and M. Ernzerhof, J. Chem. Phys. **118**, 8207 (2003).

[78] J. Heyd, G. E. Scuseria, and M. Ernzerhof, J. Chem. Phys. **124**, 219906 (2006).

[79] T. Stein, H. Eisenberg, L. Kronik, and R. Baer, Phys. Rev. Lett. **105** (2010).

[80] E. Livshits and R. Baer, Phys. Chem. Chem. Phys. **9**, 2932 (2007).

[81] O. A. Vydrov and G. E. Scuseria, J. Chem. Phys. **125**, 234109 (2006).

[82] W. Kohn, Y. Meir, and D. Makarov, Phys. Rev. Lett. **80**, 4153 (1998).

[83] J. Toulouse, F. Colonna, and A. Savin, Phys. Rev. A **70**, 062505 (2004).

[84] E. Goll, H.-J. Werner, and H. Stoll, Phys. Chem. Chem. Phys. **7**, 3917 (2005).

[85] K. Burke, J. P. Perdew, and D. C. Langreth, Phys. Rev. Lett. **73**, 1283 (1994).

[86] D. Langreth and J. Perdew, Phys. Rev. B **15**, 2884 (1977).

[87] N. Mardirossian and M. Head-Gordon, J. Chem. Phys. **140**, 18a527 (2014).

[88] J. D. Gledhill, M. J. G. Peach, and D. J. Tozer, J. Chem. Theory Comput. **9**, 4414 (2013).

[89] T. Stein, L. Kronik, and R. Baer, J. Am. Chem. Soc. **131**, 2818 (2009).

[90] S. Refaely-Abramson, S. Sharifzadeh, N. Govind, J. Autschbach, J. B. Neaton, R. Baer, and L. Kronik, Phys. Rev. Lett. **109** (2012).

[91] A. V. Krukau, G. E. Scuseria, J. P. Perdew, and A. Savin, J. Chem. Phys. **129**, 124103 (2008).

[92] A. D. Becke, Phys. Rev. A **38**, 3098 (1988).

[93] J. Tao, J. P. Perdew, V. N. Staroverov, and G. E. Scuseria, Phys. Rev. Lett. **91**, 146401 (2003).

[94] J. P. Perdew and W. Yue, Phys. Rev. B **33**, 8800 (1986).

[95] C. Adamo and V. Barone, J. Chem. Phys. **108**, 664 (1998).

[96] J. Harris, Phys. Rev. A **29**, 1648 (1984).

[97] J. P. Perdew, A. Ruzsinszky, J. Tao, V. N. Staroverov, G. E. Scuseria, and G. I. Csonka, J. Chem. Phys. **123**, 62201 (2005).

[98] J. P. Perdew, K. Burke, and M. Ernzerhof, Phys. Rev. Lett. **77**, 3865 (1996).

[99] M. Ernzerhof and J. P. Perdew, J. Chem. Phys. **109**, 3313 (1998).

[100] J. P. Perdew, J. A. Chevary, S. H. Vosko, K. A. Jackson, M. R. Pederson, D. J. Singh, and C. Fiolhais, Phys. Rev. B **46**, 6671 (1992).

[101] V. N. Staroverov, G. E. Scuseria, J. Tao, and J. P. Perdew, J. Chem. Phys. **119**, 12129 (2003).

[102] J. P. Perdew, V. N. Staroverov, J. Tao, and G. E. Scuseria, Phys. Rev. A **78**, 052513 (2008).

[103] A. Görling, Phys. Rev. Lett. **83**, 5459 (1999).

[104] R. van Leeuwen and E. J. Baerends, Phys. Rev. A **49**, 2421 (1994).

[105] M. Levy and J. P. Perdew, Phys. Rev. B **48**, 11638 (1993).

[106] N. C. Handy and A. J. Cohen, Mol. Phys. **99**, 403 (2001).

[107] W. Kohn and L. J. Sham, Phys. Rev. **140**, A1133 (1965).

[108] J. Sun, B. Xiao, Y. Fang, R. Haunschild, P. Hao, A. Ruzsinszky, G. I. Csonka, G. E. Scuseria, and J. P. Perdew, Phys. Rev. Lett. **111** (2013).

[109] A. D. Becke and K. E. Edgecombe, J. Chem. Phys. **92**, 5397 (1990).

[110] J. P. Perdew and J. Tao, J. Mol. Struct. (Theochem) **943**, 19 (2010).

[111] L. Goerigk and S. Grimme, J. Chem. Theory Comput. **7**, 291 (2011).

[112] A. Tajti, P. G. Szalay, A. G. Csaszar, M. Kallay, J. Gauss, E. F. Valeev, B. A. Flowers, J. Vazquez, and J. F. Stanton, J. Chem. Phys. **121**, 11599 (2004).

[113] R. Peverati and D. G. Truhlar, Phil. Trans. R. Soc. A **372**, 20120476 (2014).

[114] A. Schafer, C. Huber, and R. Ahlrichs, J. Chem. Phys. **100**, 5829 (1994).

[115] J. VandeVondele, U. Borštnik, and J. Hutter, J. Chem. Theory Comput. **8**, 3565 (2012).

[116] K. Burke, J. Chem. Phys. **136**, 150901 (2012).

[117] J. F. Dobson and J. Wang, Phys. Rev. Lett. **82**, 2123 (1999).

[118] H. Eshuis, J. E. Bates, and F. Furche, Theor. Chem. Acc. **131**, 1084 (2012).

[119] H. Eshuis and F. Furche, J. Phys. Chem. Lett. **2**, 983 (2011).

[120] F. Furche, J. Chem. Phys. **129**, 114105 (2008).

[121] X. Ren, P. Rinke, C. Joas, and M. Scheffler, J. Mater. Sci. **47**, 7447 (2012).

[122] H. Eshuis, J. Yarkony, and F. Furche, J. Chem. Phys. **132**, 234114 (2010).

[123] M. Kaltak, J. Klimeš, and G. Kresse, Phys. Rev. B **90**, 054115 (2014).

[124] G. E. Scuseria, T. M. Henderson, and D. C. Sorensen, J. Chem. Phys. **129**, 231101 (2008).

[125] H. van Aggelen, Y. Yang, and W. Yang, J. Chem. Phys. **140**, 18A511 (2014).

[126] F. Furche, Phys. Rev. B **64**, 195120 (2001).

[127] Z. Yan, J. P. Perdew, and S. Kurth, Phys. Rev. B **61**, 16430 (2000).

[128] D. Bohm and D. Pines, Phys. Rev. **82**, 625 (1951).

[129] D. Bohm and D. Pines, Phys. Rev. **92**, 609 (1953).

[130] D. Pines and D. Bohm, Phys. Rev. **85**, 338 (1952).

[131] F. Furche, Phys. Rev. B **64**, 195120 (2001).

[132] Y. Yang, H. van Aggelen, and W. Yang, J. Chem. Phys. **139**, 224105 (2013).

[133] F. Furche and T. Van Voorhis, J. Chem. Phys. **122**, 164106 (2005).

[134] D. C. Langreth and J. P. Perdew, Solid State Commun. **17**, 1425 (1975).

[135] M. Fuchs and X. Gonze, Phys. Rev. B **65**, 235109 (2002).

[136] J. E. Bates and F. Furche, J. Chem. Phys. **139**, 171103 (2013).

[137] M. Petersilka, U. J. Gossmann, and E. K. U. Gross, Phys. Rev. Lett. **76**, 1212 (1996).

[138] F. Haase and R. Ahlrichs, J. Comput. Chem. **14**, 907 (1993).

[139] D. C. McCutcheon, M. A. Paley, and R. C. Steinhardt, J. Am. Chem. Soc. **134**, 7604 (2012).

[140] N. R. Conley, A. Dragulescu Andrasi, J. Rao, and W. E. Moerner, Angew. Chem., Int. Ed. **124**, 3406 (2012).

[141] M. S. Evans, J. P. Chaurette, S. T. Adams Jr, and G. R. Reddy, Nature Meth. **11**, 393 (2014).

[142] R. Kojima, H. Takakura, T. Ozawa, and Y. Tada, Angew. Chem., Int. Ed. (2013).

[143] D. M. Mofford, G. R. Reddy, and S. C. Miller, J. Am. Chem. Soc. **136**, 13277 (2014).

[144] H. Fraga, Photochem. Photobiol. **7**, 146 (2008).

[145] M. A. Paley and J. A. Prescher, Med. Chem. Comm. **5**, 255 (2014).

[146] W. C. Rhodes and W. D. McElroy, J. Bio. Chem. **233**, 1528 (1958).

[147] S. M. Marques and J. C. G. Esteves da Silva, IUBMB Life **61**, 6 (2009).

[148] S. Inouye, Cell. Mol. Life Sci. **67**, 387 (2010).

[149] D. M. Mofford, G. R. Reddy, and S. C. Miller, Proc. Natl. Acad. Sci. U.S.A. **111**, 4443 (2014).

[150] B. R. Branchini, C. E. Behney, and T. L. Southworth, J. Am. Chem. Soc. **137**, 7592 (2015).

[151] H. Wörther, G. F. Field, and W. D. McElroy, J. Org. Chem. **30**, 2344 (1965).

[152] E. H. White and D. F. Roswell, Photochem. Photobiol. **53**, 131 (1991).

[153] B. R. Branchini, M. M. Hayward, S. Bamford, P. Brennan, and E. J. Lajiness, Photochem. Photobiol. **49**, 689 (1989).

[154] C. C. Woodroofe, P. L. Meisenheimer, and D. H. Klaubert, Biochemistry **51**, 9807 (2012).

[155] G. R. Reddy and W. C. Thompson, J. Am. Chem. Soc. **132**, 13586 (2010).

[156] R. Bauernschmitt and R. Ahlrichs, Chem. Phys. Lett. **256**, 454 (1996).

[157] G. Orlova, J. D. Goddard, and L. Y. Brovko, J. Am. Chem. Soc. **125**, 6962 (2003).

[158] A. M. Ren and J. D. Goddard, J. Photoch. Photobio. B **81**, 163 (2005).

[159] A. M. Ren, J. F. Guo, J. K. Feng, and L. Y. Zou, Chinese J. Chem. (2008).

[160] K. Støchkel, B. F. Milne, and S. B. Nielsen, J. Phys. Chem. A **115**, 2155 (2011).

[161] M. Hiyama, H. Akiyama, and T. Mochizuki, Photoch. Photobiol. (2014).

[162] Z. S. Li, C. G. Min, A. M. Ren, L. Y. Zou, and Z. Xu, J. Photoch. Photobiol. A **243**, 7 (2012).

[163] D. Rappoport and F. Furche, J. Chem. Phys. **133**, 134105 (2010).

[164] P. Deglmann, K. May, F. Furche, and R. Ahlrichs, Chem. Phys. Lett. **384**, 103 (2004).

[165] F. Furche and R. Ahlrichs, J. Chem. Phys. **117**, 7433 (2002).

[166] A. Dreuw, J. L. Weisman, and M. Head-Gordon, J. Chem. Phys. **119**, 2943 (2003).

[167] I. Navizet, N. Ferré, W. H. Fang, and R. Lindh, J. Chem. Theory Comput. **7**, 798 (2011).

[168] E. H. White, E. Rapaport, H. H. Seliger, and T. A. Hopkins, Bioorg. Chem. **1**, 92 (1971).

[169] J. Leitão and J. da Silva, J. Photoch. Photobiol. B **101**, 1 (2010).

[170] L. P. da Silva and J. C. G. E. Da Silva, Photochem. Photobiol. Sci. **10**, 1039 (2011).

[171] J. R. Lakowicz, "Principles of fluorescence spectroscopy" (2013).

[172] E. Lippert, W. Luder, and H. Boos, "Advances in molecular spectroscopy" (1962).

[173] Z. R. Grabowski, K. Rotkiewicz, and A. Siemiarczuk, J. Lumin. **18**, 420 (1979).

[174] Z. R. Grabowski and J. Dobkowski, Pure Appl. Chem. **55**, 245 (1983).

[175] Z. R. Grabowski, J. Dobkowski, and W. Kühnle, J. Mol. Struct. **114**, 93 (1984).

[176] Z. R. Grabowski, K. Rotkiewicz, and W. Rettig, Chem. Rev. **103**, 3899 (2003).

[177] J. B. Grimm, B. P. English, J. Chen, J. P. Slaughter, and Z. Zhang, Nature Meth. **12**, 244 (2015).

[178] M. Vogel, W. Rettig, R. Sens, and K. H. Drexhage, Chem. Phys. Lett. **147**, 452 (1988).

[179] T. G. Waddell, J. Chem. Ed. **80**, 883 (2003).

[180] S. Johansson, C. C. C, M. O. Kitching, T. J. Colacot, and V. Snieckus, Angew. Chem., Int. Ed. **51**, 5062 (2012).

[181] J. A. Sundlov, D. M. Fontaine, and T. L. Southworth, Biochemistry **51**, 6493 (2012).

[182] R. A. Morton, T. A. Hopkins, and H. H. Seliger, Biochemistry **8**, 1598 (1969).

[183] O. Shimomura and T. Goto, Proc. Natl. Acad. Sci. U.S.A. **74**, 2799 (1977).

[184] W. J. Evans, Coord. Chem. Rev. **206**, 263 (2000).

[185] H. M. Crosswhite, H. Crosswhite, W. T. Carnall, and A. P. Paszek, J. Chem. Phys. **72**, 5103 (1980).

[186] M. R. MacDonald, J. W. Ziller, and W. J. Evans, J. Am. Chem. Soc. **133**, 15914 (2011).

[187] W. J. Evans, N. T. Allen, and J. W. Ziller, J. Am. Chem. Soc. **122**, 11749 (2000).

[188] M. R. MacDonald, J. E. Bates, J. W. Ziller, F. Furche, and W. J. Evans, J. Am. Chem. Soc. **135**, 9857 (2013).

[189] M. Szostak and D. J. Procter, Angew. Chem., Int. Ed. **51**, 9238 (2012).

[190] W. J. Evans, N. T. Allen, and J. W. Ziller, J. Am. Chem. Soc. **122**, 11749 (2000).

[191] P. Girard, J. L. Namy, and H. B. Kagan, J. Am. Chem. Soc. **102**, 2693 (1980).

[192] M. Chinol, S. Vallabhajosula, and S. J. Goldsmith, J. Nucl. Med. (1993).

[193] W. J. Evans, M. Fang, G. Zucchi, F. Furche, J. W. Ziller, R. M. Hoekstra, and J. I. Zink, J. Am. Chem. Soc. **131**, 11195 (2009).

[194] V. Smil, *Enriching the earth: Fritz Haber, Carl Bosch, and the transformation of world food production* (MIT press, 2004).

[195] P. J. Chirik and K. Wieghardt, Science **327**, 794 (2010).

[196] D. C. Leitch, P. R. Payne, C. R. Dunbar, and L. L. Schafer, J. Am. Chem. Soc. **131**, 18246 (2009).

[197] K. E. Meyer, P. J. Walsh, and R. G. Bergman, J. Am. Chem. Soc. **116**, 2669 (1994).

[198] C. K. Jørgensen, Coord. Chem. Rev. **1**, 164 (1966).

[199] M. D. Ward and J. A. McCleverty, Dalton Trans. , 275 (2002).

[200] E. Billig, R. Williams, I. Bernal, J. H. Waters, and H. B. Gray, Inorganic Chemistry **3**, 663 (1964).

[201] H. B. Gray, R. Williams, I. Bernal, and E. Billig, J. Am. Chem. Soc. **84**, 3596 (1962).

[202] R. A. Zarkesh, J. W. Ziller, and A. F. Heyduk, Angew. Chem., Int. Ed. **47**, 4715 (2008).

[203] D. Herebian, K. E. Wieghardt, and F. Neese, J. Am. Chem. Soc. **125**, 10997 (2003).

[204] P. Chaudhuri, C. N. Verani, E. Bill, and E. Bothe, J. Am. Chem. Soc. **123**, 2213 (2001).

[205] J. L. Wong, R. F. Higgins, I. Bhowmick, D. X. Cao, G. Szigethy, J. W. Ziller, M. P. Shores, and A. F. Heyduk, Chem. Sci. (2016).